Processes Regulating Iron Supply at the Mesoscale (PRISM)
NBP12-01 Cruise Report
Draft February 12, 2012

Contents

Introduction

The Ross Sea continental shelf is the single most productive area in the Southern Ocean, and may comprise a significant but unaccounted for oceanic CO_2 sink, largely driven by phytoplankton production. However, the processes that control the magnitude of primary production in this region are not well understood. During summer, an observed abundance of macronutrients and scarcity of dissolved iron are consistent with iron limitation of phytoplankton growth in the Ross Sea polynya, as is further suggested by shipboard bioassay experiments. Field observations and model simulations indicate four potential sources of dissolved iron to surface waters of the Ross Sea: (H_1) circumpolar deep water intruding from the shelf edge; (H_2) sediments on shallow banks and nearshore areas; (H_3) melting sea ice around the perimeter of the polynya; and (H_4) glacial meltwater from the Ross Ice Shelf. These potential iron sources are isolated, either laterally or vertically, from the surface waters of the Ross Sea for much of the growing season. We hypothesize that hydrodynamic transport via mesoscale currents, fronts, and eddies facilitate the supply of dissolved iron from these four sources to the surface waters of the Ross Sea polynya. Our cruise plan was designed to accomplish two distinct objectives: (A) regional-scale, high-resolution transects to characterize the hypothesized source regions of iron, and (B) mini-process studies to examine selected mesoscale features in detail.

Sampling overview

Voyage #12-01 of the RVIB Nathaniel B. Palmer was a 49 day journey from Punta Arenas Chile to McMurdo Station, Antarctica. Shortly after departure on 24 December 2011, we

took the opportunity to test two of our towed instrument platforms, the Moving Vessel Profiler (MVP) and the Video Plankton Recorder (VPR). These systems were then stowed away for the transit to the Ross Sea. During a particularly good stretch of weather on January 1-2, the VPR was deployed for a 25-hour tow, described in section 3 below. Later in transit, we began to address PRISM objectives with an opportunistic process study in and around a band of sea ice in the Antarctic Circumpolar Current (H_3). We entered the eastern Ross Sea on January 9, and with the aid of a recently acquired MODIS image sampled two eddies. Shortly after beginning a detailed survey of Eddy 2, we broke off from science operations to respond to a distress call from F/V *Jung Woo 2*. The rescue mission was completed on January 11 with the evacuation of seven injured fishermen to McMurdo Station. Science operations were recommenced in the Western Ross Sea, starting with a zonal transect at 76° 40' followed by detailed studies of a cyclonic eddy (including a SeaHorse deployment) and the frontal region between high- and low-biomass areas of the zonal transect (H_3). We then proceeded to Ross Bank for surveys and deployment of the SeaHorse in a moored configuration (H_2). Next on our agenda was the Ross Ice Shelf, where we sampled Ice Shelf Water and a cyclonic eddy moving northward from the ice edge (H_4). From there we transited back to Ross Bank for recovery of the SeaHorse and then proceeded to Joides Trough to sample Modified Circumpolar Deep Water coming up onto the shelf (H_1). The last phase of the cruise, we revisited the Western Ross Sea with re-occupation of the 76° 40' line, study of an eddy near the ice edge, sampling of a suspected hydrothermal vent site near Franklin Island, a north-south transect along 169°E, detailed survey of a frontal region between 169°E and 170°E, and an extension of the 76° 40' line (actually at 76° 45') into the far western Ross Sea previously covered with ice (H_2, H_3). Detailed station maps are presented in Figures 1-6.

NBP1201 Ross Sea Area
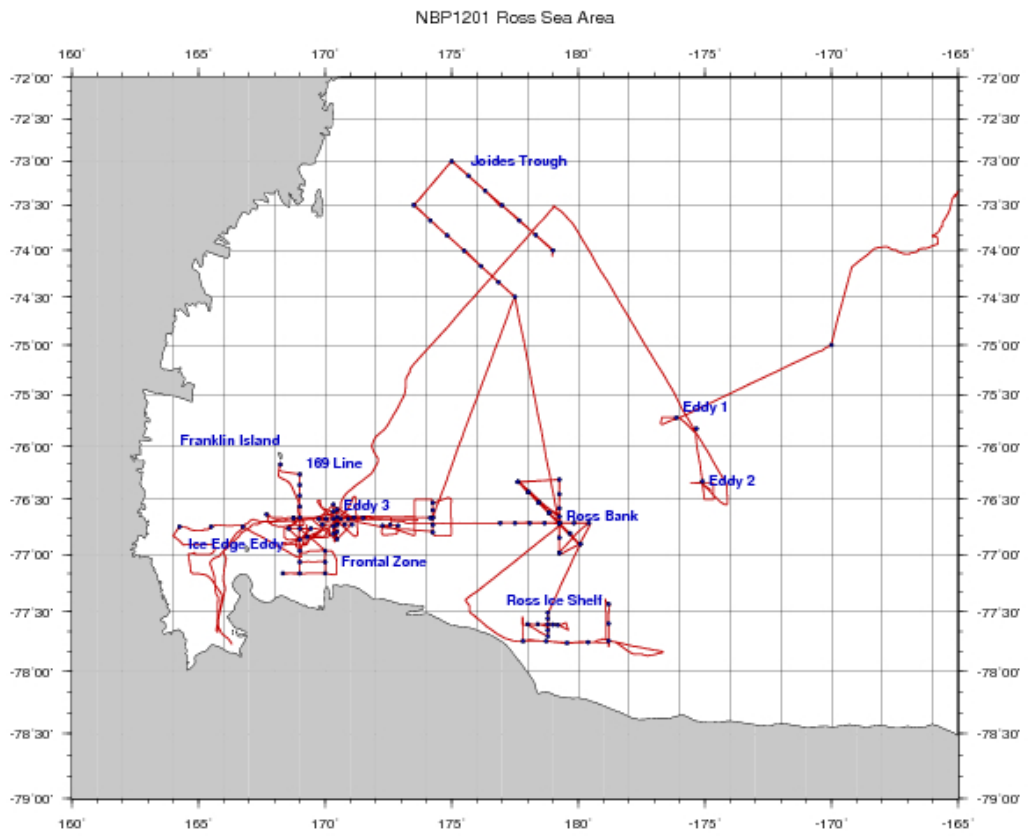
Science activities in transit

In transit to the Ross Sea, we deployed the VPR on New Year's Day 2012. The 25-hour tow spanned longitudes 110-121°W of our west-southwestward trackline (Figure Transit.1). Initially low fluorescence rapidly increased to high values between 111-113°W (247-249°E), roughly corresponding to an upwelling of relatively warm and salty water in the 50-100m depth interval. This area of enhanced fluorescence corresponds to the interior of a counter-clockwise eddy-like feature (Figure Transit.1d). A second area of enhanced fluorescence was centered on 114°W (246°E), the location of another eddy-like feature with distinctly different properties—most notably a positive salinity anomaly in the upper ocean. Nearly contiguous with that feature was another band of high fluorescence spanning ca. 115-116°W (244-245°E), perhaps related to a front. Fluorescence decreased dramatically south and west of that front, and remained low for the duration of the transect. The low-fluorescence region is characterized by a relatively warm and fresh surface layer overlying a lens of very cold water near the freezing point.

The areas of high fluorescence where characterized by a large number of amorphous image targets (Figure Transit.2). Microscopic examination of a sample taken from the ship's underway seawater system by Hai suggest these may be comprised of a mucus matrix with diatoms in their interior—however, that analysis is based on only one sample.

Regional/Process Studies

ACC sea ice process study

Ice conditions dictated an entrance point into the Ross Sea of ca. 72° 30' S, 162°W, with exit at ca. 74° S, 168°W. We took the opportunity to occupy three stations in the vicinity: one offshore of the sea ice, one in the midst of it, and one inshore (Figure ACC.1). This set of stations provides contrasting samples for H_3 (sea ice), as well as three replicates for H_1 (CDW). One appealing aspect of the sea ice assessment is that, in contrast to the western Ross Sea, surface waters in this area are not subject to other proximal sources such as continental or sedimentary inputs. Initial analysis of the iron data suggest enhanced concentrations in near surface waters at Station 2 relative to surrounding Stations 1 and 3 (Figures ACC.2). Although chlorophyll was lower at Station 2, Fv/Fm values were higher, suggesting better physiological condition of the phytoplankton within the ice pack (Figure ACC.3).

Eastern Ross Sea Eddies

Upon entering the Ross Sea polynya, we were fortunate to receive a clear MODIS image in our operational area. This facilitated sampling of two distinct eddy features, "Eddy 1" and "Eddy 2". Eddy 1 was nicknamed "Geordie" in honor of Chris Marsay's birthday on January 9. Based on recent imagery, both features appear to be translating to the northeast at ca. 5 km d^{-1} (Figure ERS.1). An underway MVP/XBT/ADCP survey (Figure ERS.2,3,4,5) was successful in locating Geordie's center slightly northeast of its position in the satellite image, confirming enhanced fluorescence in its interior (Station 4). Station 5 was occupied in comparatively low chlorophyll water southeast of Geordie, providing contrast between inside- and outside-the-eddy conditions. Variable fluorescence Fv/Fm increased with depth both inside and outside the eddy (Figure ERS.6). Chl biomass, as indicated by Fm was substantially higher inside versus outside the eddy.

Subsequent to departure from Geordie, we proceeded to Eddy 2 and a similar technique was used to locate eddy center from the underway MVP/XBT/ADCP data (Figure ERS.7). The interiors of both eddies are characterized by a doming of the halocline and relatively warm temperatures in the upper ocean (Figure ERS.2).

After occupying station 6 the center of eddy 2, we deployed the VPR and surveyed from eddy center to its southeastern flank and slightly north thereof (Figure ERS.8), at which point the NBP responded to a distress call. Similar to the MVP data, the VPR observations show upward doming of the halocline and a positive temperature anomaly in the upper layer. The VPR fluorometer was set to a maximum of 5 µg Chl l^{-1}, so it saturated in the upper ocean during most of the transect. Although it is not possible to quantify the detailed structure of the fluorescence field with these data, the thickness of the saturated layer is clearly larger at eddy center than it is at the periphery. Initial analysis of the VPR plankton imagery (Figure ERS.9) suggests the high fluorescence coincided with enhanced abundance of *Phaeocystis* colonies. The colonies appeared to be aggregated into large clumps near the surface, with individual colonies more common at depth. Also at depth there were many kidney-shaped objects that looked like either deflated or half-eaten *Phaeocystis* colonies. *Phaeocystis* distributions derived from an at-sea classifier suggests covariance of individuals and aggregated colonies, with the population centers of mass deeper inside the eddy than at the periphery (Figure ERS.10). In addition, both "kidney beans" and marine snow are most abundant at depth in the eddy core.

Stations 4-6 were all characterized by surprisingly elevated dissolved Fe levels (ca. 0.3-0.4 nM) in the photic zone - possibly derived from the sea ice to the north (Figure ACC.2). However, surface towfish samples also revealed some low dissolved Fe (ca. 0.1) surface 'patches' in this area.

Interestingly, the highest values of fluorescence observed in the MVP survey data occurred in the area northeast of Geordie, an apparently eddy-like feature that was obscured by clouds (Figure ERS.1). The MVP data also provide a means to assess the presence of MCDW (Figure ERS.3), and it is clear that we have not encountered it yet in the depth interval sampled by the MVP. The underway XBT data reveal the warm signature of CDW in the deep waters seaward of the continental shelf, but there is no trace of MCDW on the shelf itself (Figure ERS.4).

This phase of the project was cut short so the NBP could participate in the rescue of injured men from the F/V *Jung Woo 2*.

Western Ross Sea Process Study

After completing the rescue of the injured men from the F/V *Jung Woo 2*, we occupied a west-to-east transect of three stations from the ice edge (station 8) to high and low biomass areas (stations 9 and 10, respectively) identified in the most recent satellite image (Figure WRS.1). Underway MVP data (Figure WRS.2) reveal a dramatic drop in fluorescence between stations 9 and 10, consistent with the MODIS image. The transect also showed enhanced fluorescence associated with an upward doming of the halocline at ca. 170° 30'E, around which ADCP velocities suggested a strong cyclonic flow. CTD and nutrient sections are presented in Figures WRS.3 and WRS.4.

Dissolved Fe (Figure WRS.5) was somewhat elevated (ca. 0.2 nM) in the photic zone at the ice edge on western side of the polynya (Station 7), and further east in the 'high biomass' region (Station 8), whereas dissolved Fe was low (< 0.1 nM) in the photic zone in low biomass waters further to the east (Station 9). At depth, dissolved iron increased from west to east.

Variable fluorescence along this same line showed some correspondence with upper ocean iron concentrations, such that the fittest phytoplankton were located from the high-biomass area to the western side of the frontal boundary. Variable fluorescence was quite low in the iron-depleted waters of the low-biomass area, although photochemical quenching could be an issue. Bongo net tows in this area reveal that the pteropod *Limacina* is abundant, as are copepods, and substantial numbers of the carnivorous pteropod *Clione* were also observed.

We then occupied a VPR transect back west along the trackline, followed by a detailed survey of Eddy 3 (Figure WRS.6). ADCP velocities from the survey confirm the clockwise circulation of the feature (Figure WRS.7). Even with the VPR fluorometer set to a scale of 0-15 μg Chl l^{-1}, the instrument still saturated in several areas, including the relatively warm and fresh near-surface waters of eddy center. Plankton images from the VPR revealed abundant *Phaeocystis*, which according to Hai's microscopy were in excellent condition (c.f. the aggregated clusters observed in the VPR survey of Eddy 2, Figure ERS.9). The VPR also recorded curious "white out" conditions in near surface waters, which corresponded with high values of fluorescence and turbidity. We speculate this optical effect may have been caused by scattering from very abundant small (ca. 1-2μ by 10-15μ) diatoms identified in Hai's microscopy (Figure WRS.8). In many areas, the VPR data seemed to indicate a layering of phytoplankton community structure, with the suspected diatom bloom overlying deeper populations of *Phaeocystis*. With the VPR survey complete, we occupied a station at eddy center (station 10) and deployed the SeaHorse Buoy in that location. Subsequently, east-west and north-south cross-sections of stations were occupied (Figures WRS.7, WRS.9-12). Upper ocean hydrographic characteristics are roughly consistent with expectation based on the VPR survey: fluorescence is highest in the warm and fresh waters in the eddy interior; the halocline is domed upward at depth. The deeper CTD data show that upward doming of the halocline and associated pycnocline extends at least deep as 700m (bottom depth in this area is ~740 m). These fluctuations are also manifested in the distributions of oxygen and beam attenuation. Mesoscale variations in macronutrients are modest below the euphotic zone, reflecting the relatively homogeneous vertical distribution of nutrients in this high-nutrient low-chlorophyll environment. However, there are clear manifestations of the eddy in upper ocean nutrient distributions: for example, in the areas of highest fluorescence silicate is lower, nitrite is higher, and the ammonacline is shallower. Near-surface iron depletion is enhanced at eddy center; the ferrocline is domed upward at depth, mimicking the structure of the halocline and pycnocline (Figure WRS.13). Variable fluorescence measurements indicate a strong vertical gradient in physiological status below the near-surface chlorophyll maximum where iron is more readily available. However, quenching may play an important role in the upper part of the euphotic zone.

With the SeaHorse deployed in the center of Eddy E3, we sought to contrast the high-biomass conditions in which the eddy resides with the lower-biomass environment to the east (Figure WRS.1). The first component of that was a detailed VPR survey of the frontal region between the two (Figure WRS.14), which revealed a clear water mass transition over very small spatial scales (a few km). Specifically, in surface waters the high-biomass water to the west was warmer and fresher than the low-biomass water to the east. At depth (ca. 100m) the sign of the salinity gradient changes, such that the waters underlying the high-biomass water are slightly saltier than those underlying the low-biomass water. The front appears to be meandering, with the boundary located farther east in the cross-section at 76.75S than it is in the cross-sections to the north and south. Strong southward velocities are present in the vicinity of the front, with

some reverse flow on the eastern periphery of the 76.75S cross-section (Figure WRS.15).   A CTD cross section highlights the dramatic change in water properties across the front (Figures WRS.16). Macronutrients show relatively modest gradients across the front, with the exception of silicate which shows evidence of enhanced removal associated with the diatom bloom present west of the front (Figure WRS.17). Iron depletion in the upper ocean is strongest where the lowest chlorophyll biomass is located on the east side of the front (Figure WRS.18), although at depth dissolved iron increases from west to east. The fact that that lowest surface dissolved iron values (ca. 0.1 nM) to east of the biomass front suggest that iron availability played some role in defining this biomass gradient.

After the frontal survey we sought to characterize a larger area of low-biomass water with a radiator-pattern VPR survey (Figure WRS.19). The northwest corner contained high fluorescence associated with a warm and fresh water mass, suggesting an eastward meander of the high-biomass front into that area. Although the chlorophyll fluorescence is considerably lower in the low-biomass region, there is significant submesoscale variability in this area. ADCP currents suggest generally southward flow (FigureWRS.20). A north-south transect of stations was occupied in the center line of the VPR survey (Figure WRS.21,22), in which the upper ocean hydrographic characteristics were roughly consistent with expectation based on the VPR survey. The deeper data reveal hints of MCDW with local temperature maximum at depths of 200-300m, although the waters comprising these local maxima are cold (<-1°C). Variable fluorescence measurements suggest a strong vertical gradient in phytoplankton physiological status below the subsurface chlorophyll maximum, but again photochemical quenching may be a significant factor in the upper part of the euphotic zone (Figure WRS.23).

With the characterization of the low-biomass area complete, we returned to Eddy 3 for a final VPR survey (Figure WRS.24) followed by repeats of the east-west and north-south sections. The sections were oriented approximately 5km NW or the original location to account for movement of the eddy during the intervening period. The new fix on eddy center was derived from a combination of ADCP data (Figure WRS.25) and the trajectory of the SeaHorse Buoy (Figure WRS.25).   Overall, upper ocean properties during the second survey were similar to the prior occupation (Figures WRS.27-30). However, the upward doming of the halocline and pycnocline below 400m is less evident in the second survey. One notable change in the nutrient distributions is the increase in nitrite in the 50-150m depth interval, which is evident in both east-west and north-south sections. The mesoscale distribution of dissolved iron again shows maximum surface depletion at eddy center and elevated values at depth (Figure WRS.31).   The observed depletion in dissolved iron in surface waters of the eddy core implies importance of primary production in drawing down iron availability within the polynya. MODIS imagery from January 18 illustrate the imprint of Eddy 3 on SST and upper ocean chlorophyll distributions (Figure WRS.32).

In essence, Eddy 3 appears to be a local enhancement of biomass couched within a larger area of high biomass in the western Ross Sea. Highest biomass coincides with a warm fresh layer in the near-surface waters of the eddy core (Figure WRS.32). Although the near-surface waters of the high-biomass region appear to constitute a dramatic departure from the Orsi and Weiderwohl climatology (Figure WRS.33, left), temperatures in this range are within the envelope of prior observations (Figure WRS.33, right). That being said, the high-biomass water occupies an area of T-S space that is not abundantly populated by prior measurements.

Where might this warm and fresh water have come from? A satellite composite from January 13 indicates a band of warm water running roughly north-south just to the east of the ice

edge (Figure WRS.34). These images suggest two possibilities: (1) retreating sea ice leaves a wake of warm, fresh, (previously) high-iron meltwater; and (2) there is an eastward eddy flux of warm, fresh, (previously) high-iron meltwater. Of course these two hypotheses are not mutually exclusive, and both may contribute. Two lines of evidence support the viability of (2). First, the core of Eddy 3 contains a distinct salinity anomaly at depth, which suggests a non-local origin. The large scale salinity gradient points toward a source in the western Ross Sea. Second, the upper ocean heat content of the eddy core is significantly higher than the surrounding water (Figure WRS.35). Regardless of the mechanism(s) responsible for creating this environment, it is clear that these highly stratified (and previously iron replete?) conditions favor high biomass conditions which consist of both diatoms and *Phaeocystis*.

Ross Bank

We be began our study of Ross Bank with a VPR survey, which indicated that waters on the crest were colder, saltier, and less stratified than the surrounding areas (Figure RB.1). Fluorescence was generally lower on the crest and higher on the periphery of the bank; highest values occurred just to the south of the crest (see inset). Hydrography from three cross-bank CTD sections (Figures RB.2-7) was generally consistent with the VPR survey. Dissolved iron concentrations were significantly enhanced on the crest of the bank, particularly near the bottom (Figure RB.8). Near-surface waters along the periphery of the bank were relatively depleted, consistent with the increased biomass in those areas. Near-bottom waters south and east of the bank are also enriched in iron; CTD transmissometry suggests these elevated values are associated with benthic nepheloid layers (Figure RB.4).

In order to examine the idea that tidal mixing on Ross Bank provides a mechanism for iron supply, the SeaHorse profiler was deployed in a moored configuration, just north of the central crest station. According to the Erofeeva et al. (2005) tidal model, deployment coincided with spring tides (Figure RB.9). The time-series extended nearly to the neap tides, with velocities decreasing from ca. 35 cm s^{-1} to ca. 15 cm s^{-1} during the period. Strong tidal fluctuations were present in all quantities measured by SeaHorse, including temperature, salinity, fluorescence and oxygen (Figure RB.10). The overall trend during the time series was cooling, freshening, decreasing fluorescence, and deepening of the mixed layer. Re-occupation of the northwest-southeast CTD section confirmed these trends (Figure RB.11,12). Differences in the temperature-salinity characteristics from the two occupations of the transect suggest the changes were not all locally forced (Figure RB.13). There was a dramatic change in the iron profile on the crest of the bank during this time period (Figure RB.14). Near-surface concentrations decreased only slightly, but there was a major removal of iron in the 70-150m depth interval. The nature of this change is such that the most likely explanation is advective.

Quantification of the advective loss of iron from the bank will be possible based on PRISM observations. The iron observations along the transects will provide estimates of the spatial gradients, and ADCP measurements from the underway system and SeaHorse mooring provide velocity information. Interpretation of the ADCP current velocities is made difficult by the strong tides present in this area (Figure RB.15), but the availability of an accurate tidal model (Erofeeva et al. 2005) facilitates real-time inference of the subtidal flow. To evaluate the effectiveness of this approach, we compared velocities from two occupations of the southeast-to-northwest survey lines, the first of which was executed when the tide was running north, and the other when the tide was running south (middle panel; two tracks indicated by black arrows). Close examination of the predicted subtidal flow (right panel) shows a consistent depiction of the

residual current, which is to the north SE of the crest and to the south NW of the crest. The direction of the around-bank flow is qualitatively consistent with expectation from the Dinniman et al. ROMS model results. Full evaluation of the advective flux of iron awaits shore-based analysis, but given the relatively low concentrations of iron flanking the crest, advective loss is certainly a plausible explanation.

Lastly, we note an interesting feature in the VPR surveys on approach to Ross Bank (Figure RB.16). In several places along the west-to-east track, there were small-scale enhancement of fluorescence that were associated with subsurface boluses of warm and fresh water. The nature of these features is not known.

Ross Ice Shelf

Survey of the Ross Ice Shelf (RIS) afforded the opportunity to investigate iron supply through both glacial meltwater near the surface and Ice Shelf Water (ISW) at depth. ISW has yet to be sampled for iron in any prior measurements that we are aware of, and is potentially high in iron for two reasons illustrated in a schematic (Figure RIS.1) by Smethie and Jacobs (2005). To begin with, one contributor of the source water is High Salinity Shelf Water (HSSW), which has high iron content associated with its own formation region in the western Ross Sea. Secondly, melting of the glacier at the grounding line may release iron bound within the ice.

ISW is visible in the Orsi and Wiederwohl (2009) climatology (Figure RIS.2) as super-cooled water emanating from underneath the RIS near the dateline (180° longitude). "Super-cooled" is defined as water with potential temperature θ below the surface freezing point ($\theta < -1.937$). ISW is clearly visible as a mid-depth temperature minimum in a quasi-synoptic zonal section occupied in February 1984 (Figure RIS.3), although the location of the ISW core can vary interannually (Figure).

Salinity of the ISW tends to be somewhat fresher than the surrounding waters in that same density range (Figure RIS.2), although that signature is less evident in a vertical section view (Figure RIS.3). Oxygen content of the ISW is intermediate at the location of its exit from underneath the RIS, but is clearly influenced by the high-oxygen water of the RIS polynya between 170 and 178°E as this water mass extends equatorward.

Based on both climatological and synoptic views, it appeared that a quasi-zonal section spanning 175°E to 175°W should encompass the core of the ISW emanating from underneath the RIS. In some years, the ISW core is displaced slightly east of the dateline (Figure RIS.4). However, based on these prior observations, 175°W appeared to be far enough east to delimit the core of the ISW. Zonal extent of the core varies between 2-6° in longitude, or ca. 50-150km.

With the 175°E to 175°W longitudinal band of the RIS as our target, we deployed the MVP at Ross Bank and set course for the western edge of the survey area (Figure RIS.5). As we approached the RIS, there was a general decrease in near surface temperature and salinity, accompanied by an increase in fluorescence. This cooling and freshening was clearly visible in the temperature-salinity relationship as we approached the RIS (Figure RIS.6). Underway XBTs revealed the presence of ISW starting just prior to arrival at the RIS (Figure RIS.7). Along the ice edge, the most prominent occurrences of ISW were noted at 178°E to 178.5°W, and the CTD transects were oriented accordingly. A seaward extension of the along-shelf transect was added in an attempt to sample the lower biomass waters identified offshore in the MVP survey; alas this offshore extension found its way into a high-biomass filament. In any case, the RIS CTD survey hit significant amounts of ISW in every single cast (Figure RIS.8,9). The ISW does appear to be enriched in dissolved iron, with values in its core of ca. 0.3-0.5 nM, similar to CDW (Figure

RIS.10). Near-surface values also appear to be relatively high, with concentrations on the order of 0.2 nM, except for a small area of near-surface iron depletion on the western edge of the survey line.

During the RIS CTD survey we were fortunate to receive MODIS SST and chlorophyll images that indicated a pair of eddies moving northward from the ice edge, both of which exhibited relatively cold SSTs and low chlorophyll (Figure RIS.11). The VPR was deployed and we were able to survey a cross-section of the western eddy and part of the eastern eddy before ice conditions necessitated recovery of the instrument (Figure RIS.12). Contrary to expectation based on the MODIS chlorophyll image, the cold and fresh waters of the eddy interior contained high fluorescence that was spread over a large depth interval (ca. 100 m inside the eddy versus ca. 50 m outside the eddy; cf. a euphotic zone depth of ca. 20m). VPR plankton images suggested this high biomass consisted mostly of *Phaeocystis* colonies. ADCP velocities revealed the counter-clockwise flow of this anticyclone and apparent compression of the feature on its eastern flank due to interaction with the adjacent anticyclone to the east (Figure RIS.12, right panel). The frontal region between the two eddies actually contains the highest fluorescence observed during the abbreviated VPR survey. East-west and north-south CTD sections across the eddy confirm the hydrographic characteristics observed with the VPR (Figure RIS.13-16). The deeper CTD data reveal isopycnals below ca. 300 m are relatively flat, suggesting the eddy is a relatively near-surface phenomenon. Dissolved iron measurements made on two stations in the east-to-west section across the eddy show depletion in the upper 100 m relative to the water adjacent to the RIS (ca. 0.1 nM versus 0.2 nM), consistent with uptake by the high biomass within the eddy feature (RIS.17). These data are consistent with an eddy-induced lateral transport of iron from near-surface waters of the RIS.

Joides Trough

The intrusion and upwelling of Modified Circumpolar Deep Water (MCDW) has been proposed as a potential source of iron to surface waters at several locations on the Antarctic margin. Dinniman et al. (2003) have explicitly modeled the intrusion of CDW on to the Ross Sea shelf, and one of the preferred pathways is through the Joides Trough, flanked by Mawson and Pennell Banks. To map out this pathway, we conducted an initial VPR/XBT survey along two transects near the outer reaches of the Joides Trough (Figures JT.1,2). On first approach to the trough from Ross Bank, the subsurface temperature maxima characteristic of MCDW intrusions were evident on both eastern and western flanks of Pennell Bank, as well as on its crest. The highest values of fluorescence observed during the entire VPR survey were in this general vicinity, and plankton imagery suggested *Phaeocystis* was abundant. Proceeding across the trough, MCDW was also evident on the eastern flank of Mawson Bank. The most prominent expression of MCWD occurred while transiting along the crest of Mawson Bank (XBTs 102-103). The second cross-trough section showed a similar pattern, with MCDW present on both the eastern flank of Mawson Bank and the western flank of Pennell Bank. In contrast to the prior crossing of Pennell Bank, MCDW was less evident in the shallower waters of the crest. Outside of the area of high fluorescence on Pennell Bank, VPR data indicated high abundance of small diatom chains and some copepods, particularly in the northwestern-most area of the survey. CTD sections confirm the distribution of MCDW inferred from the XBT data, and illustrate the macronutrient variability in this area (Figures JT.3-6). MVP data collected along the survey track provide additional information between stations as well as the transit back to the Western

Ross Sea (Figure JT.7). XBT data were collected along the latter leg starting at the southern end of Pennell Bank, documenting the thinning of MCDW along that transect (Figure JT.8).

Shipboard dissolved Fe analyses from the JOIDES Trough transects (Figures) indicate higher surface dissolved Fe values (~0.2 nM) on the northern transect, perhaps reflecting the lesser time that these waters have been free of sea ice cover. These data also suggest that benthic Fe sources from shelf depressions (rather than banks) may be at least as important in supplying Fe to surface waters as intrusions of MCDW.

Western Ross Sea, revisited

Near-surface conditions during our first occupation of the Western Ross Sea (WRS) were characterized by slightly elevated iron and high biomass in the west, with low iron and low biomass in the east. Re-occupation of that same area later in the cruise afforded several opportunities: (1) assessment of "post-bloom" conditions, to ascertain whether any further drawdown of iron had occurred, and whether exhaustion of the iron supply would cause a decrease in biomass; (2) opportunistic sampling of a suspected hydrothermal vent near Franklin Island; (3) occupation of a north-south transect at 169E to assess east-west transport issues, and (4) additional detailed studies of the mesoscale environment.

MVP re-survey of the east-west line at 76° 40' showed that the front between high- and low-biomass regions is in approximately the same location as it was in the first occupation (Figure WRS2.1). Although the fluorescence data suggest near-surface chlorophyll biomass decreased, it also appears that the mixed layer deepened, most likely as a result of the cold temperatures and moderate winds during the intervening period. Vertical integrals will need to be computed in order to assess the net change in biomass between the two occupations. A repeat CTD transect along the 76° 40' line confirmed the changes in fluorescence and stratification (Figure WRS2.2,3), and it does appear that near-surface iron concentrations decreased between surveys (Figure WRS2.4).

Survey of an anticyclonic eddy near the ice edge revealed striking mesoscale and submesoscale variations in physical and biological properties (Figure WRS2.5). Underway ADCP measurements during the survey document the counter-clockwise circulation within the feature (Figure WRS2.6). East-west and north-south CTD transects illustrate the downward deflection of isopycnal surfaces, owing to relatively warm and fresh waters of the eddy's interior (Figure WRS2.7-10.   These perturbations are mostly confined to the upper few hundred meters, suggesting the importance of upper ocean forcing in eddy dynamics. Near-surface waters show increased fluorescence inside the eddy. SeaHorse was deployed at eddy center, and its track was consistent with the anticyclonic circulation of the eddy (Figure WRS2.11). During the course of the deployment, periodic bouts of moderate winds from the south and southeast tended to displace the eddy away from eddy center. Resurvey of the eddy just prior to the SeaHorse recovery showed a dramatic change in the core of the eddy, as near-surface waters were significantly colder and saltier than the prior survey (Figure WRS2.12). Eddy center was characterized by a thick layer of relatively low fluorescence; VPR data suggested high abundance of *Phaeocystis*. A station was occupied at eddy center, which included an additional net tow with a hoop net aimed at catching larger predators that might be feeding on *Phaeocystis* colonies (see below). A satellite image acquired shortly after the final survey of the "Ice Edge Eddy" revealed the process responsible for the temporal changes observed at eddy center: advection of colder, saltier, and lower-biomass waters from the south and east (Figure WRS2.13).

While the SeaHorse was deployed in the Ice Edge Eddy, we journeyed to Franklin Island to sample at the site of a suspected hydrothermal vent. The return trip provided an opportunity for a north-south section along 169E which will allow us to assess the east-west geostrophic transports that may play a role in iron supply to the region. Large-scale density gradients are clearly present, as are mesoscale variations (Figure WRS2.14,15). The associated geostrophic velocities are mostly westward, except for the eastward jet on the southern flank of the eddy at ca. 76° 50' S (Figure WRS.16). ADCP velocities in the upper 200m show qualitative agreement with the geostrophic computations. Below 500m, the flow is generally weak and westward. Combining the geostrophic velocity calculations with the ADCP measurements will allow inference of the absolute velocity field which can then be combined with east-west iron gradients to estimate iron transports. North-south variations in dissolved iron are also evident (Figure WRS2.17). Iron is particularly enhanced in the benthic nepheloid layer to the north. Near-surface depletion is evident at eddy center, as is a mid-depth enhancement to the south.

The southern terminus of the 169E section afforded the opportunity to occupy the "Jacobs Gulch" time-series station to the west, followed by a survey of the frontal region to the east (Figure WRS.18). VPR data (Figure WRS.19) show this frontal boundary shares similar characteristics with that measured further to the north: near-surface waters are relatively warm, fresh, and high in fluorescence on the western side; waters on the eastern side are colder, saltier, and relatively low in fluorescence. The lower fluorescence on the eastern side of the front is spread over a larger vertical interval, so quantification of the biomass gradient awaits vertical integration. Strong southward flow is present at the frontal boundary (Figure WRS2.18). Cross-frontal (Figures WRS2.20-25) and an along-frontal (Figure WRS2.26,27) CTD sections are consistent with the results of the VPR survey in the upper ocean, and also illustrate that the zonal salinity gradient extends downward throughout most of the water column.

Extension of the 76° 40' line westward (actually at 76° 40') into the area previously covered in ice permitted sampling of the high salinity shelf waters in the western part of the basin (Figure WRS2.2,3). The highest dissolved iron concentrations measured during the entire cruise were found in this area near the bottom, and elevated iron concentrations were present all the way up to 200m (Figure WRS2.4).

Upon completion of the westernmost leg of the WRS transect, we conducted a VPR survey southward into McMurdo Sound (Figures WRS2.28-29). As suggested in the satellite imagery, substantial mesoscale variability is present in the chlorophyll field. To some degree, these fluctuations correspond to hydrographic variability—at depth there is a gradient between cold and salty waters to the north and warmer and less saline waters to the south; a freshwater lens overlies the saline waters to the north.

Preliminary Conclusions

ACC Sea Ice
> Open ocean sea ice a source of iron that improves physiological condition of phytoplankton

> Iron measurements in CDW end-member consistent with previous studies

Eastern Ross Sea Eddies
> Cyclonic eddies driven by doming of the halocline yield elevated Chl

Phaeocystis present as both individual colonies and aggregated colonies

Covariance in the distribution of individual and aggregated colonies, both deeper in the eddy interior than outside the eddy

High abundance of abandoned colonies and marine snow at depth at eddy center

Near-surface iron concentrations of 0.3-0.4 nM both inside and outside eddies

Western Ross Sea
    Frontal boundary separates warm, fresh, higher iron (0.2 nM) surface waters to the west from cold, salty, lower iron (0.1 nM) surface waters to the east; pattern consistent with a wake of retreating sea ice

    At depth, zonal trends are reversed: salinity decreases and iron increases to the east (HSSW production, bathymetry, respectively)

    Warm, fresh, higher iron near-surface waters high in biomass: diatoms near the surface, Phaeocystis down deep; phytoplankton condition better than in low-biomass waters

    Trends in macronutrient data consistent with a diatom bloom (silicate drawdown)

    Cyclonic eddy further elevates biomass in the high-biomass region; domed halocline and ferrocline consistent with increased iron supply, yet near-surface waters depleted in iron

    Temporal increase (ca. 50%) in nitrite concentration 50-150m

    Eddy heat content distinct from surrounding waters, indicating non-local origin; deep salinity suggests formation to the west

    Eastward eddy flux of warm, fresh, (previously) high-iron meltwater?

    Iron depletion and decrease in chlorophyll from 1st to 2nd occupation

Ross Bank
    Hydrographic characteristics
        Crest colder, saltier, less stratified
        Fluorescence enhanced on the more stratified periphery
        ADCP velocity suggests counter-clockwise around-bank flow
        Strong spring-neap cycle, tidal speeds ranging from 35 to 15 cm s-1

    Dissolved iron enhanced on the crest during spring tides, much less on neap tide

    Rapid removal of iron from the aphotic zone on the crest suggests advective loss; hydrographic time-series also indicative of advection

Impact of iron supply from Ross Bank could be spread into the interior Ross Sea via advection

Iron also enhanced in benthic nepheloid layers on the flanks of Ross Bank

Ross Ice Shelf

First ever iron measurements in Ice Shelf Water; concentrations similar to the MCDW end-member at 0.3-0.5 nM

Near-surface waters adjacent to the RIS were cold, fresh, and relatively enhanced in iron (ca. 0.2 nM) apparently due to glacial meltwater

Upper-ocean anticyclonic eddies can transport (previously) iron-rich waters northward, producing substantial blooms of Phaeocystis

Joides Trough

MCDW present on both eastern and western flanks of Pennell Bank, as well as its crest

Most prominent expression of MCDW on the crest of Mawson Bank; also present on the eastern flank (western flank not sampled).

Except for an area of high Phaeocystis abundance on the southwestern transect across Pennell Bank, VPR observations suggest high abundance of small chain-forming diatoms and copepods, particularly in the northwest part of the survey

Surface dissolved Fe values higher (~0.2 nM) on the northern transect, perhaps reflecting the lesser time that these waters have been free of sea ice cover.

Benthic Fe sources from shelf depressions (rather than banks) may be at least as important in supplying Fe to surface waters as intrusions of MCDW.

Iron sources in the Ross Sea

The PRISM data provide a great deal of information about sources of dissolved iron in the Ross Sea (Figure Conc.1, upper panels). The MCDW and ISW end members contain approximately the same concentration (0.3-0.5 nM), although their relative volumes are quite different. MCDW has an offshore source, and its volume decreases shoreward; in contrast, the volume of ISW is much higher on the shelf (Orsi and Wiederwohl, 2009). Interestingly, the highest dissolved iron concentrations are present closest to the bottom (Figure Conc.1, lower panels), often in association with benthic nepheloid layers. Although the pathway for supply of this deep iron source to the upper ocean is not entirely clear, it is more available in shallow / less stratified areas (e.g. Ross Bank). The most proximal source of iron for the upper ocean phytoplankton community is of course melting ice, and we encountered several circumstances in which it appeared ice melt was playing a role: ACC sea ice, Franklin Island (benthic sources also a factor), the northeastern transect across Joides Trough, the Ross Ice Shelf, and in the western Ross Sea.

Nutrient and phytoplankton dynamics

From the aggregate nutrient, nutrient ratio, chlorophyll, and iron data we can begin to discern some aspects of nutrient and phytoplankton dynamics in the Ross Sea (Figure Conc.2,3). High macronutrient and iron concentrations in deep waters give way to nutrient removal and an associated increase in chlorophyll in near-surface waters. Within these broad trends there are a number of finer-scale variations of considerable interest. For example, the high-nitrite waters inside eddy 3 on the second occupation are clearly evident. Variations in N:P and N:Si reflect changes in phytoplankton species composition, and perhaps fluctuating nutrient stoichiometry resulting from iron limitation. Detailed analysis of these variations in the context of the various hydrographic features we sampled is a high priority for post-cruise research.

Phytoplankton Physiology (contributed by Bibby/Ryan-Keogh)

In order to investigate and potentially to map the relative spatial extent of iron-limitation in the Ross Sea a series of long-term and short-term incubation experiments were conducted.

Long-Term Incubation experiments:

Changes in biomass, physiology and species composition were compared between trace-metal-clean water to which 2nM Fe had been added and control samples (no iron added) over a 7-day on-deck incubation period. During PRISM three incubators were successfully completed located at (1) Eddy 2, (2) The Ross Bank and (3) The Ice Shelf. Preliminary analysis of data suggests that all three locations eventually showed an iron-induced increase in both physiology and biomass (Figure Conc.4). However, The Ross Bank showed a relatively reduced response, potentially suggesting that at the time of sampling this phytoplankton community had sufficient available Fe to continue to grow.

Short Term Incubation experiments:

Iron-addition (2 nM Fe) incubation experiments were compared to control (no-iron added) bottles over a 48-hour on-deck incubation. 48 hours is too short a period to observe changes in biomass and/or species composition such that only physiology (Fv/Fm) is analysed. In total 29 short term incubations were set up providing good spatial resolution of all the features targeted during this study (Figures Conc.5,6). In order to compare results between experiments, the difference in Fv/Fm between control bottles and iron-addition bottles at 48 hours (delta Fv/Fm) was analysed. Preliminary findings suggest the following.

(1) Three experiments at the Ross bank showed a small response compared to the Pennell bank – suggesting the supply of iron to the phytoplankton community in the region of the Ross Bank was sufficient.
(2) The communities offshore of the Ice Shelf showed a greater response that those close to the Ice Shelf – possibly implicating the ice-shelf as a source of iron that is depleted as water is carried away from the shelf.
(3) Of the mesoscale eddies sampled 'Eddy 3' in the high-biomass region of the Western Ross sea had the largest delta Fv/Fm suggesting the supply of iron to this high biomass community is insufficient to maintain maximal growth rates.

Further detailed analysis correlating the physiological responses of in situ phytoplankton communities to nutrient availability, the protein abundance of the phytoplankton communities, and the physical environment will be conducted post-cruise at the University of Southampton, UK.

References

Dinniman, J.M., Klinck, J.M. and W.O. Smith, J., 2003. Cross-shelf exchange in a model of Ross Sea circulation and biogeochemistry. Deep Sea Research II, 50: 3103-3120.

Erofeeva, S.Y. ,Egbert, G.D., Padman, L., 2005. Assimilation of ship-mounted ADCP data for barotropic tides: application to the Ross Sea. Journal of Atmospheric and Oceanic Technology 22(6), 721–734.

Jacobs, S.S. and Giulivi, C.F., 1999. Thermohaline data and ocean circulation on the Ross Sea continental shelf. In: G. Spezie and G.M.R. Manzella (Editors), Oceanography of the Ross Sea Antarctica, pp. 3-16.

Orsi, A. H., and C. L. Wiederwohl, 2009: A recount of Ross Sea waters. Deep-Sea Res. II, 56, 778-795, (doi:10.1016/ j.dsr2.2008.10.033).

Smethie, W.M. and Jacobs, S.S., 2005. Circulation and melting under the Ross Ice Shelf: estimates from evolving CFC, salinity and temperature fields in the Ross Sea. Deep-Sea Research I, 52: 959-978.
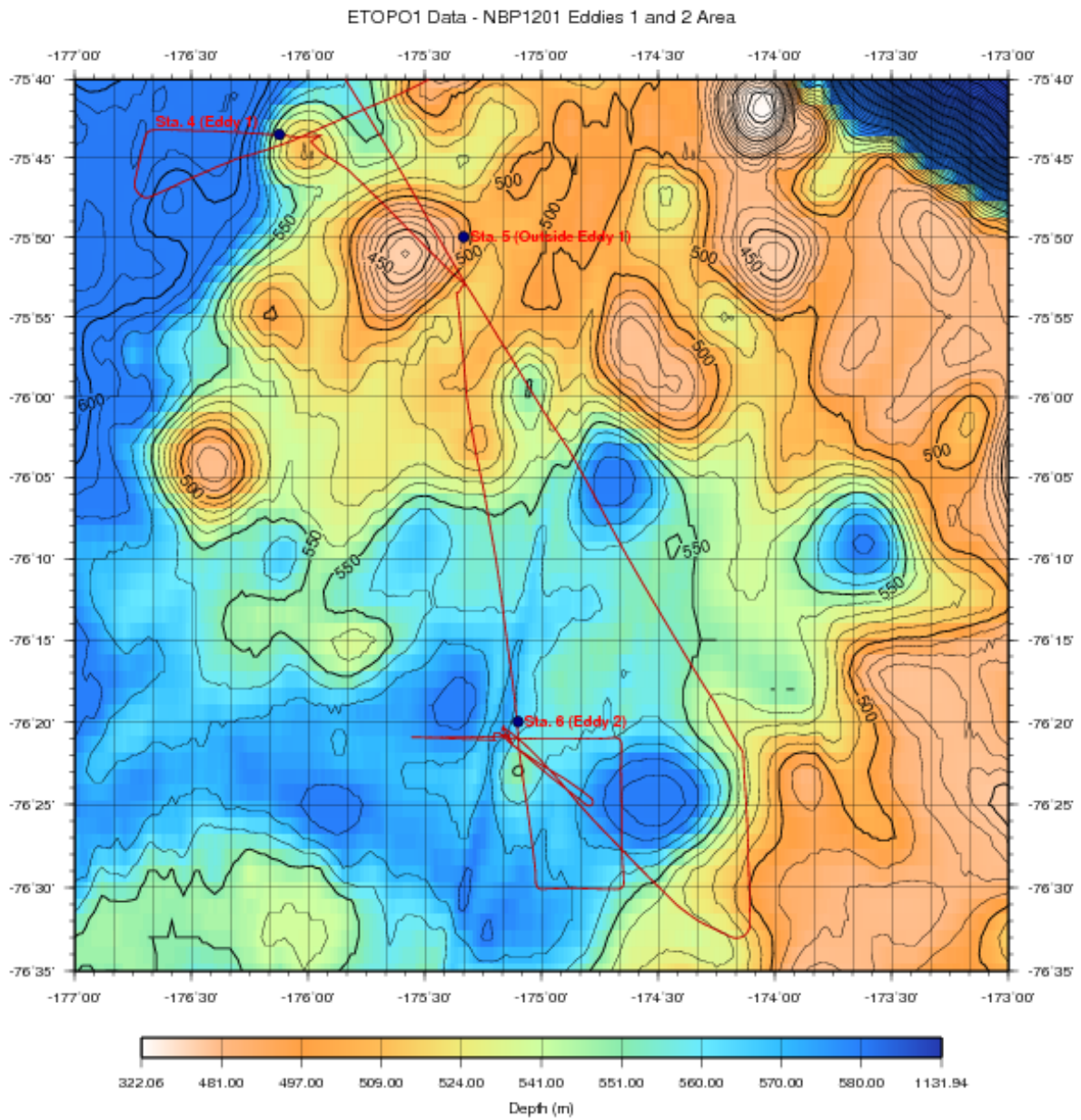
Figure 1. Station map: Eastern Ross Sea Eddies.
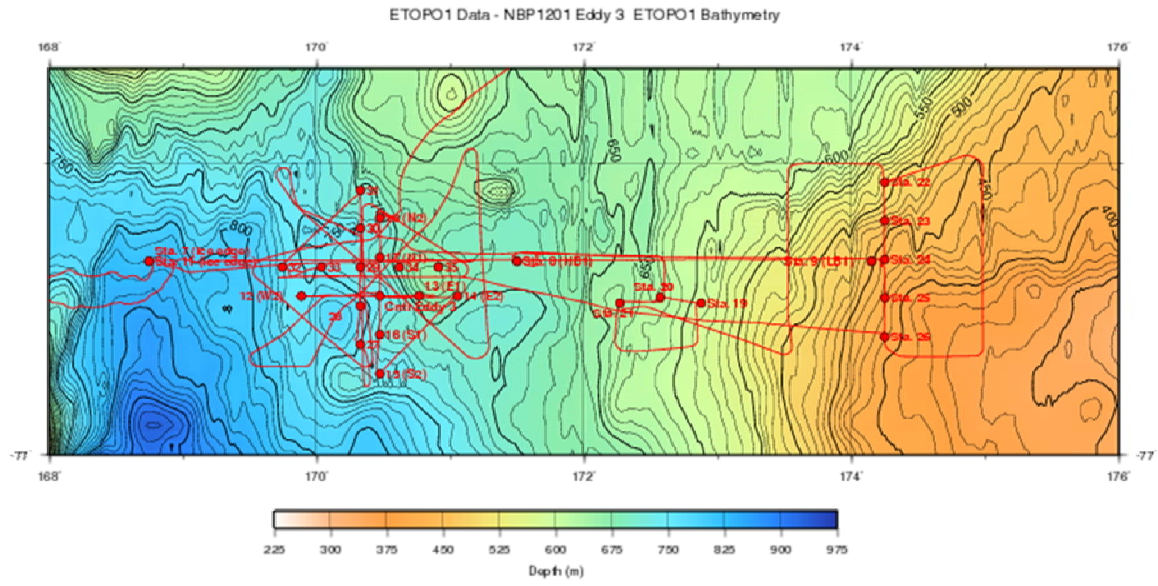
Figure 2. Station map: Western Ross Sea.
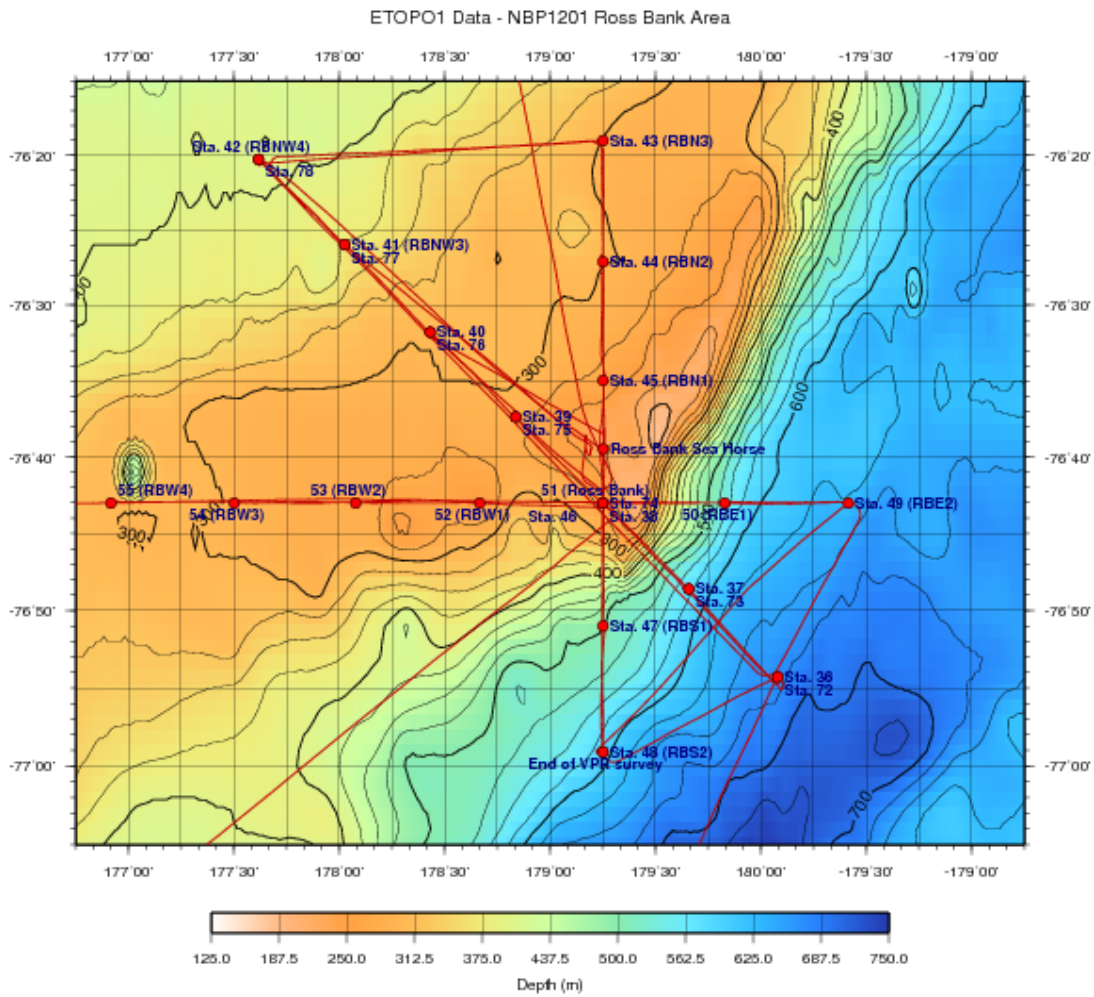
Figure 3. Station map: Ross Bank.
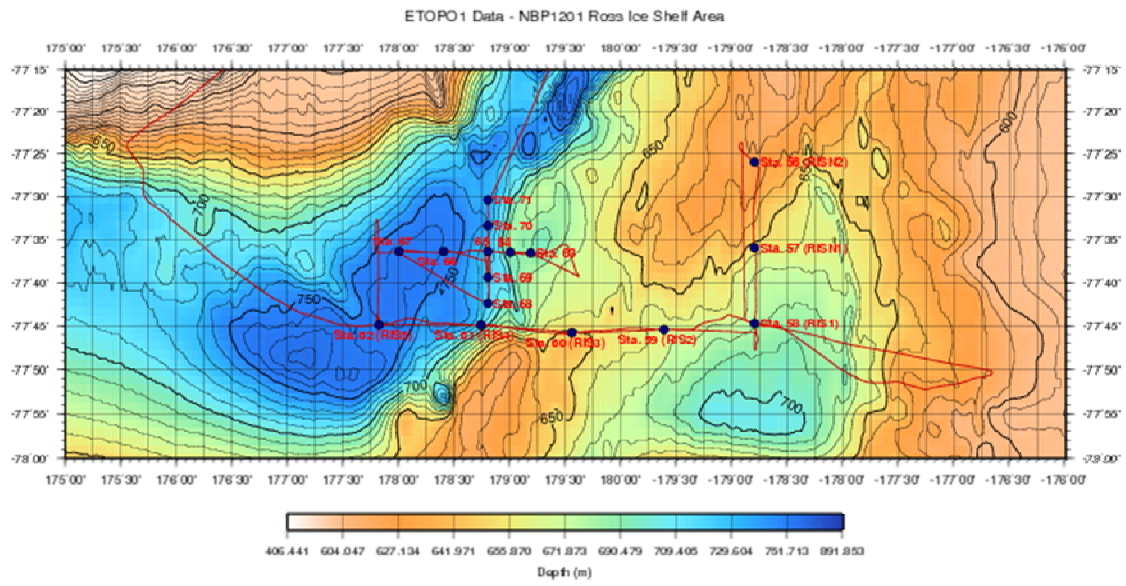
Figure 4. Station map: Ross Ice Shelf.
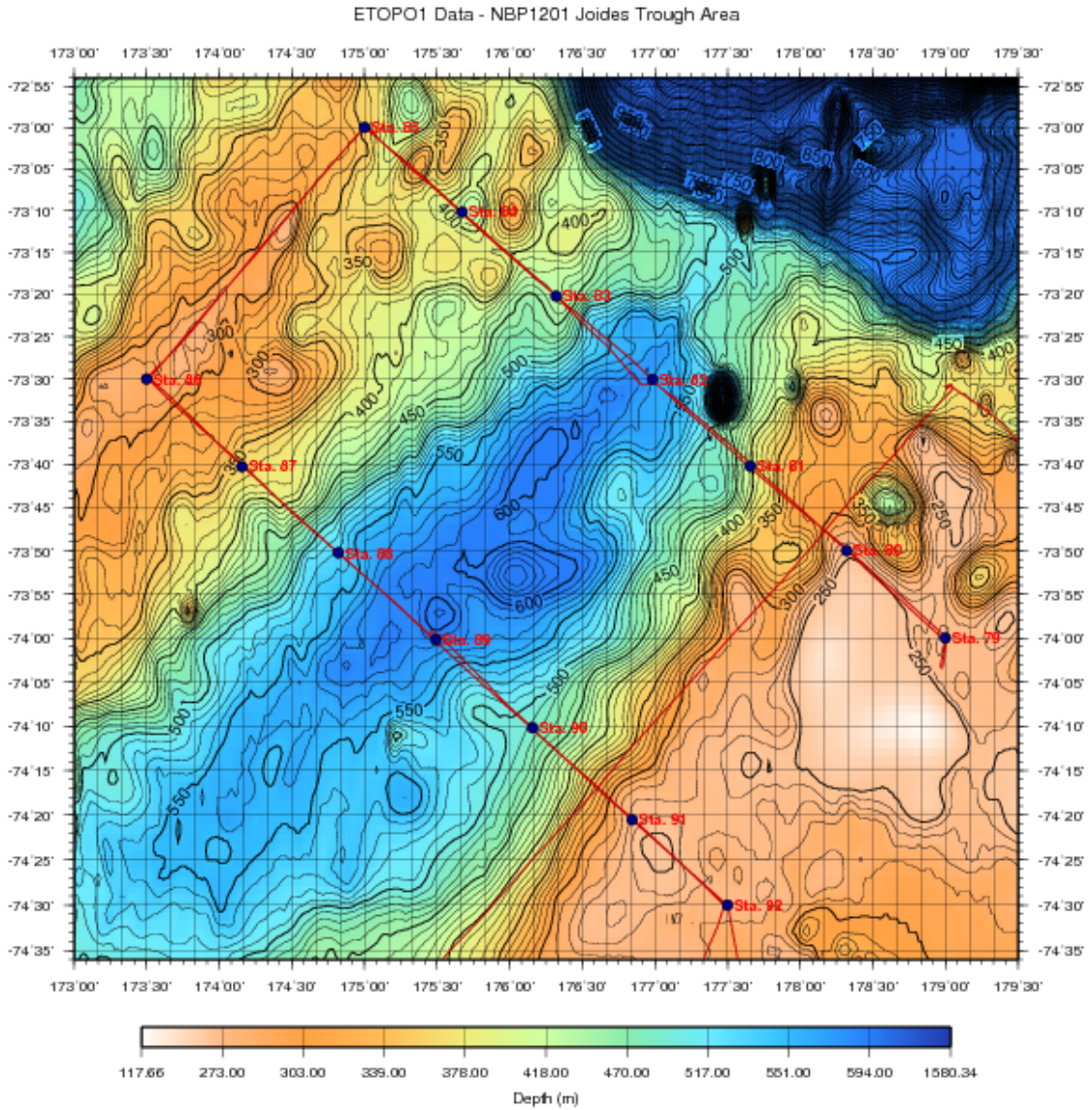
Figure 5. Station map: Joides Trough.
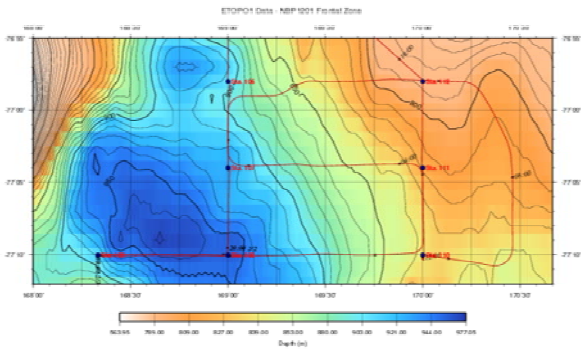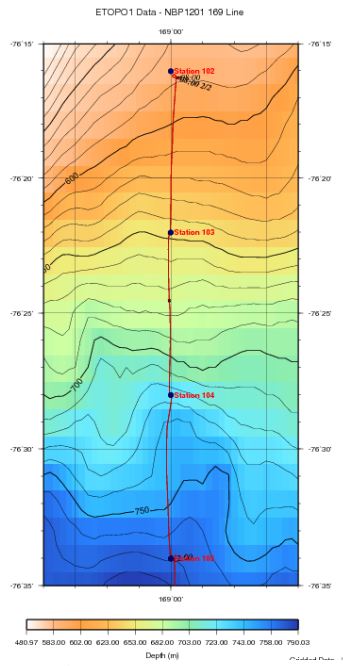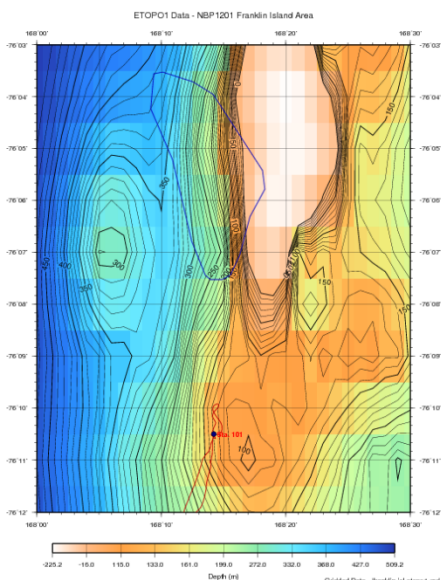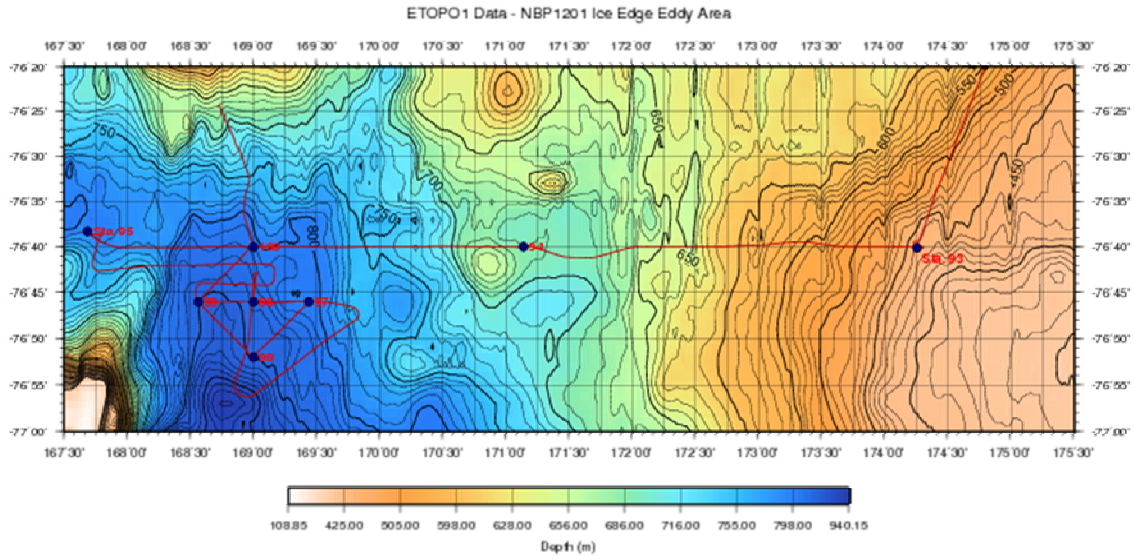
Figure 6. Station maps: Western Ross Sea II.
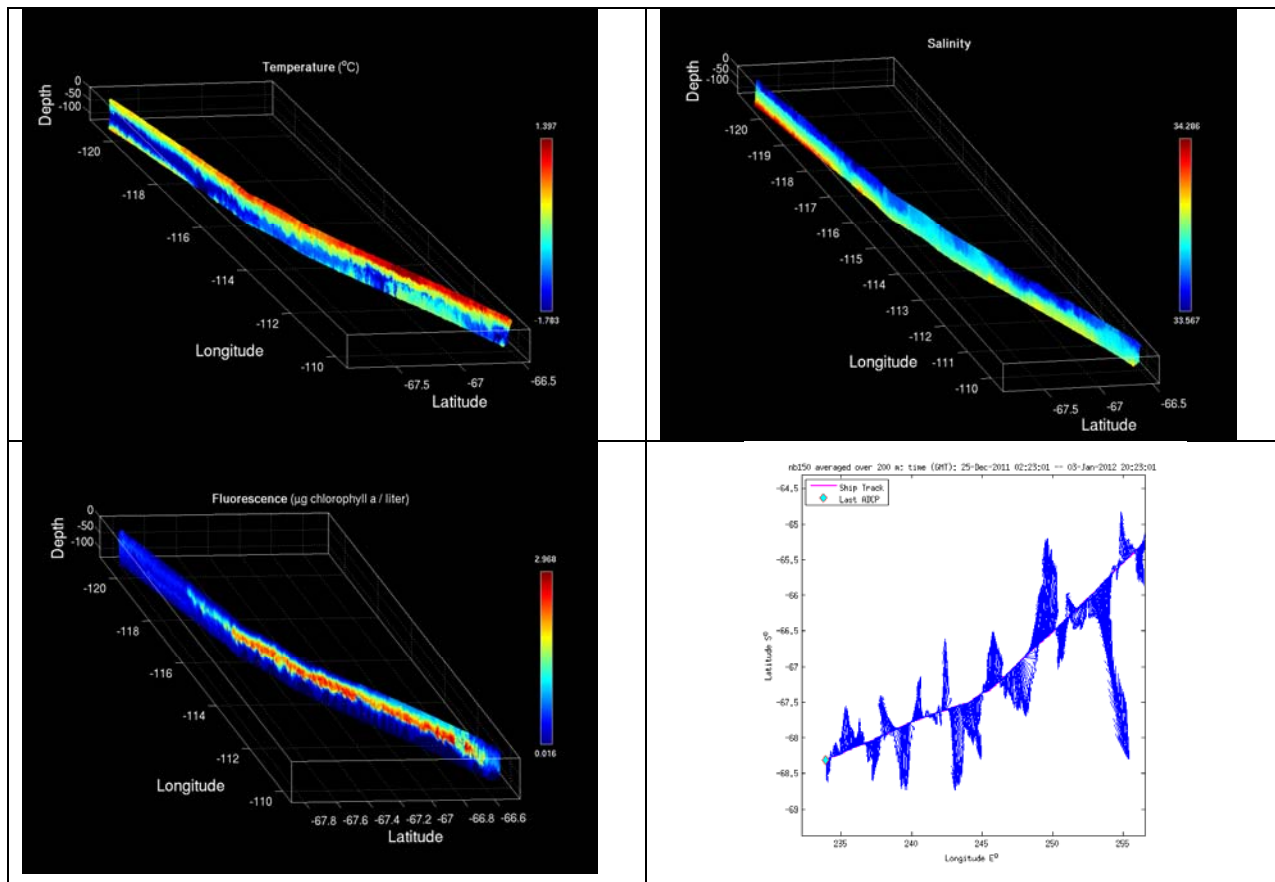
Figure Transit.1. Temperature, salinity, fluorescence, and 0-200m average current velocities for VPR2, Jan 1-3, 2012.
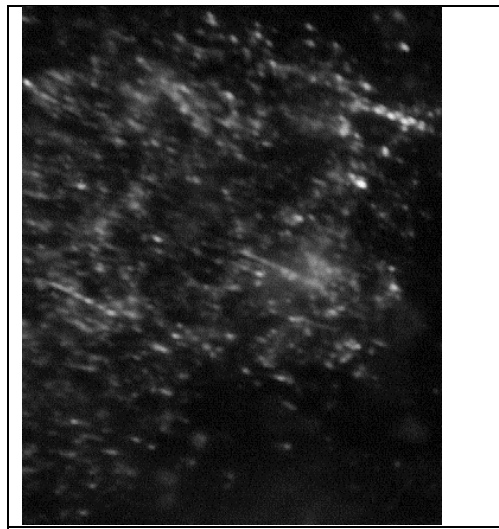
Figure Transit.2. Example VPR image from the high-fluorescence region in the transect depicted in Figure Transit.1.

Figure ACC.1. Position of stations 1-3 overlayed on SSMI/S ice concentrations for January 6, 2012. Image courtesy of PGC.

Figure ACC.2. Dissolved Fe data from stations 1-6.

Station 1 Offshore of ice pack	Station 2 Inside of ice pack	Station 3 Inshore of ice pack
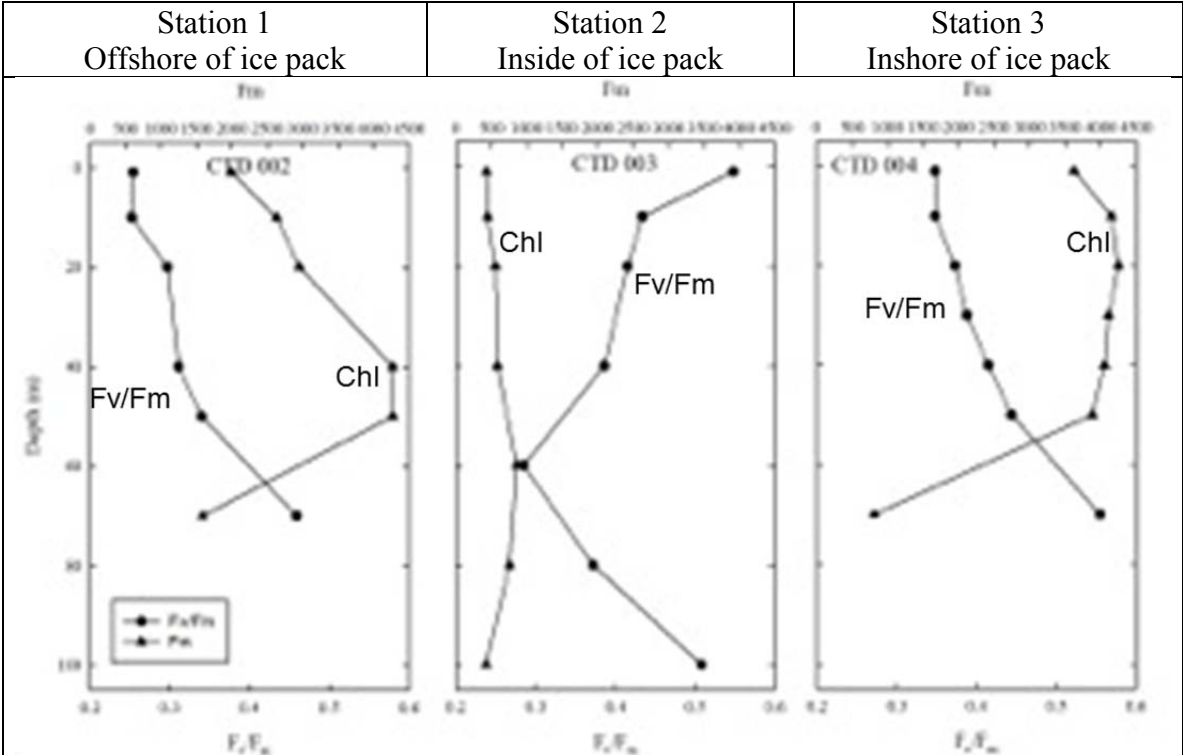
Figure ACC.3. Bibby Fv/Fm data for Stations 1-3.

Figure ERS.1. Tracks of Eddies 1 and 2 overlayed on a MODIS image from Jan 8. Fixes on eddy center determined by local maxima in chlorophyll.
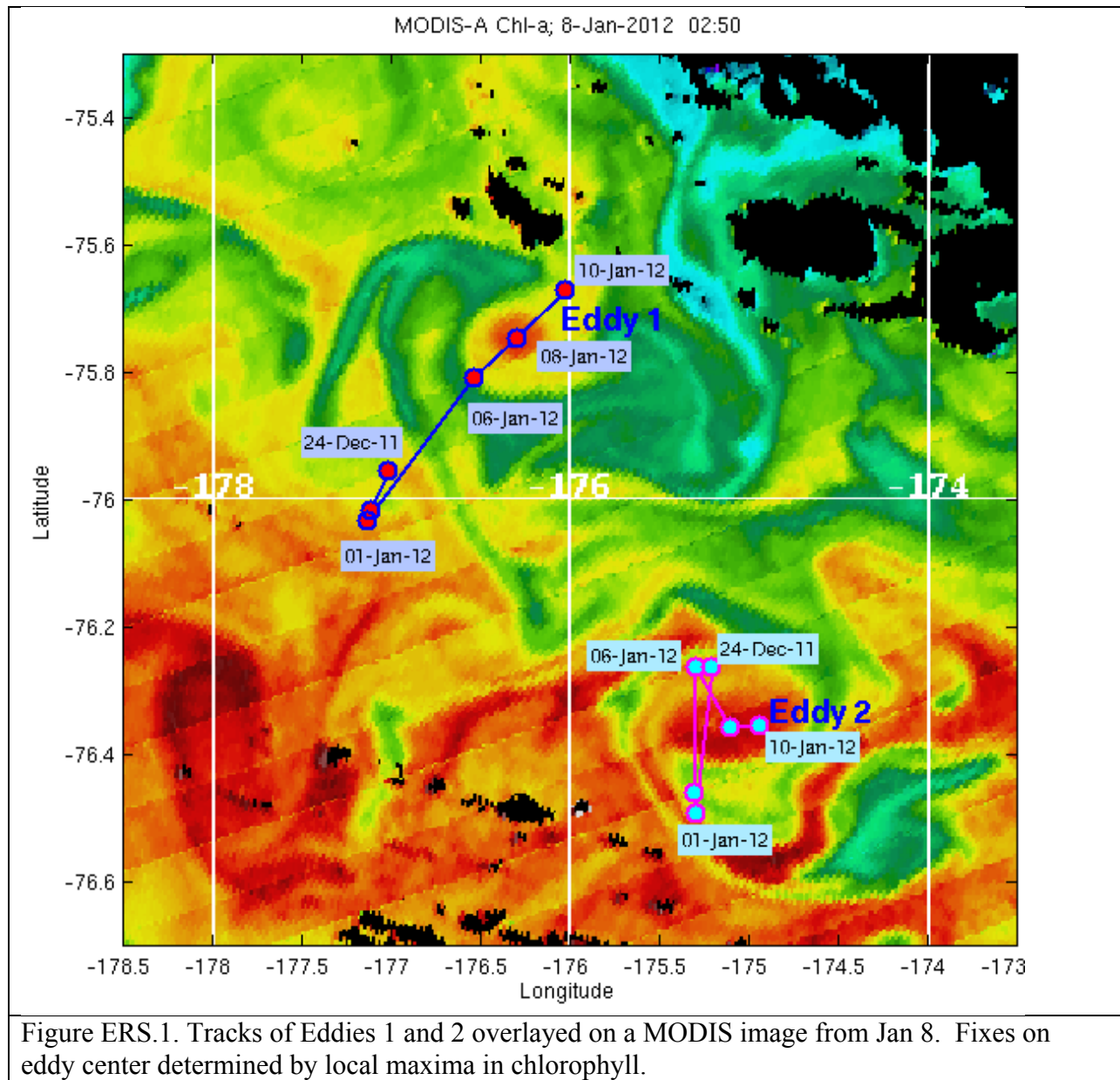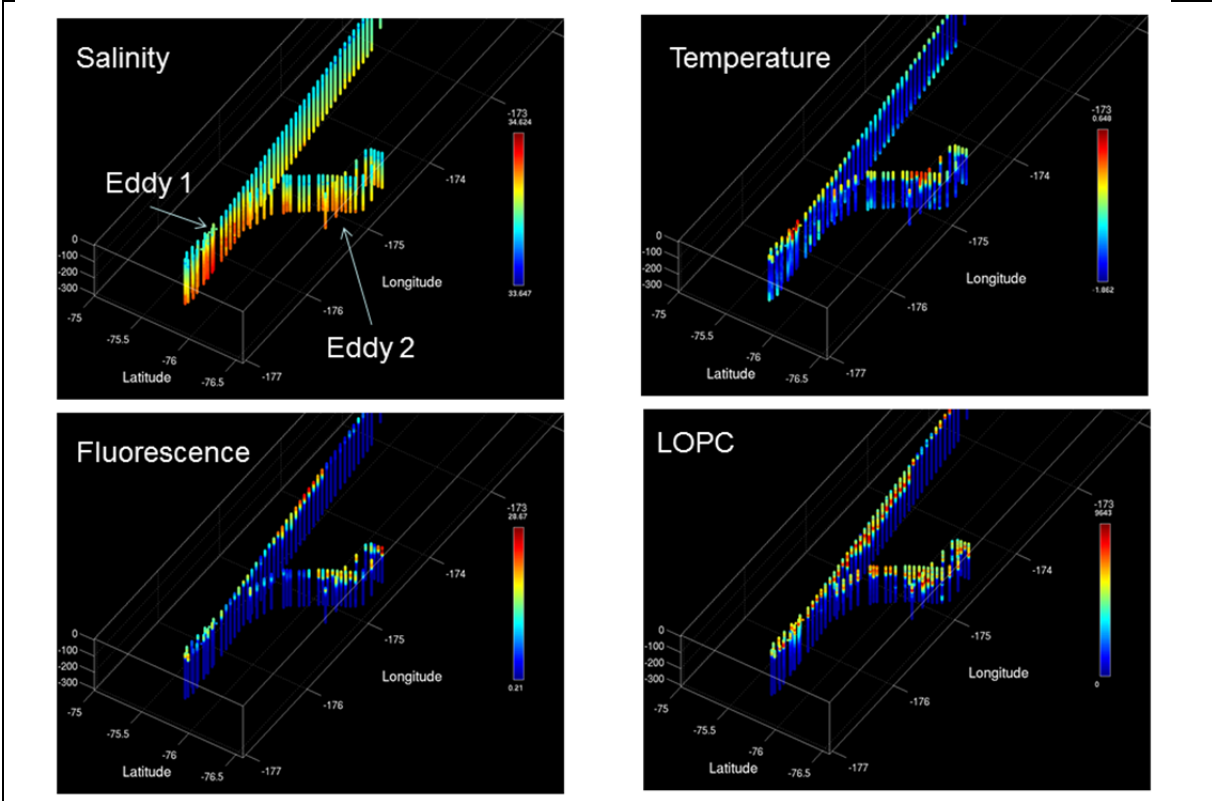
Figure ERS.2. MVP survey of eddies 1 and 2, visualized in 3D looking down from the SW.
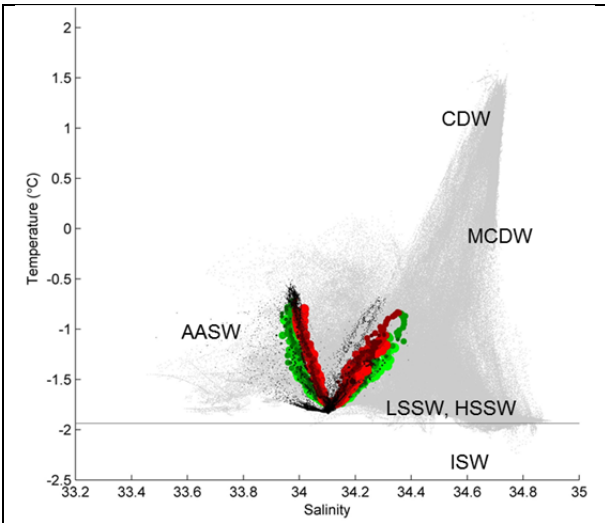
Figure ERS.3. T-S properties (small black dots, colored dots) observed during MVP survey of eddies 1 and 2 (Figure X) overlayed on Orsi climatology (gray dots).
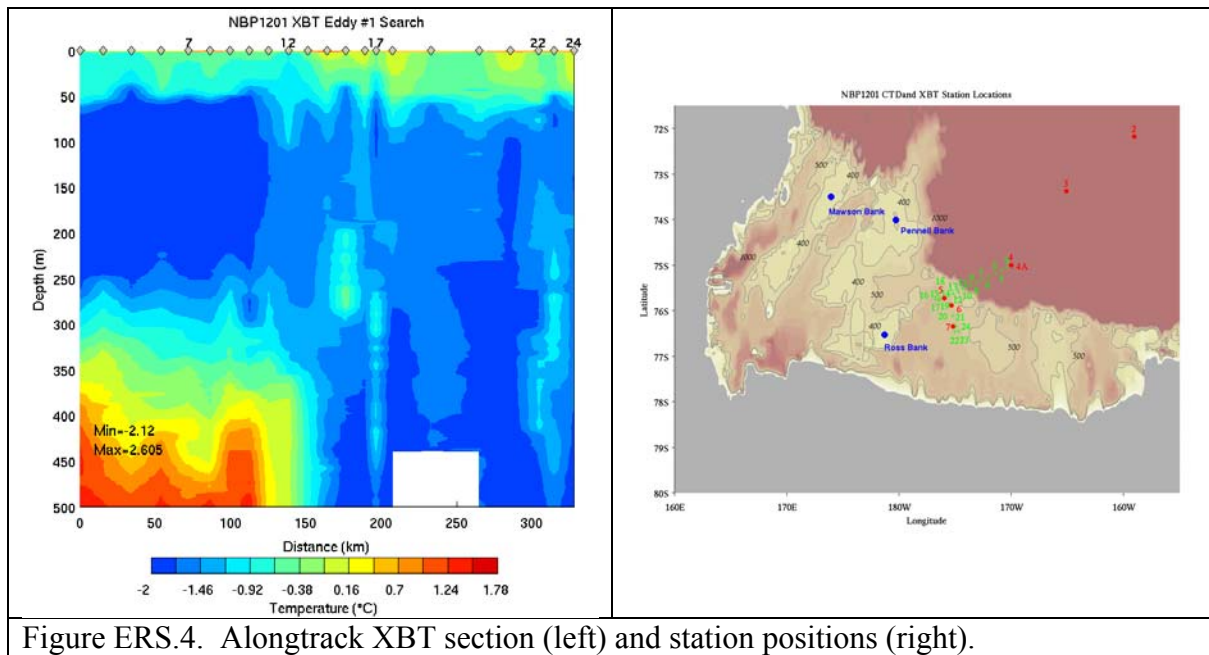
Figure ERS.4. Alongtrack XBT section (left) and station positions (right).
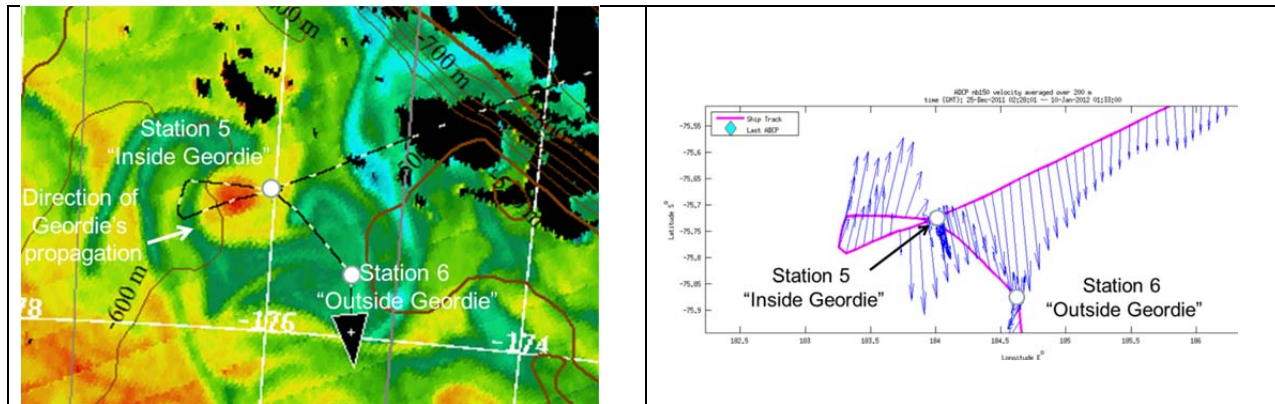
Figure ERS.5. Left: ship track overlayed on January 8 MODIS Chl image. Geordie's direction of propagation is indicated, such that eddy center had moved to the northeast by the time Station 5 was occupied on January 9. Right: zoomed view of 0-200m velocity vectors in the vicinity of Eddy 1 center.
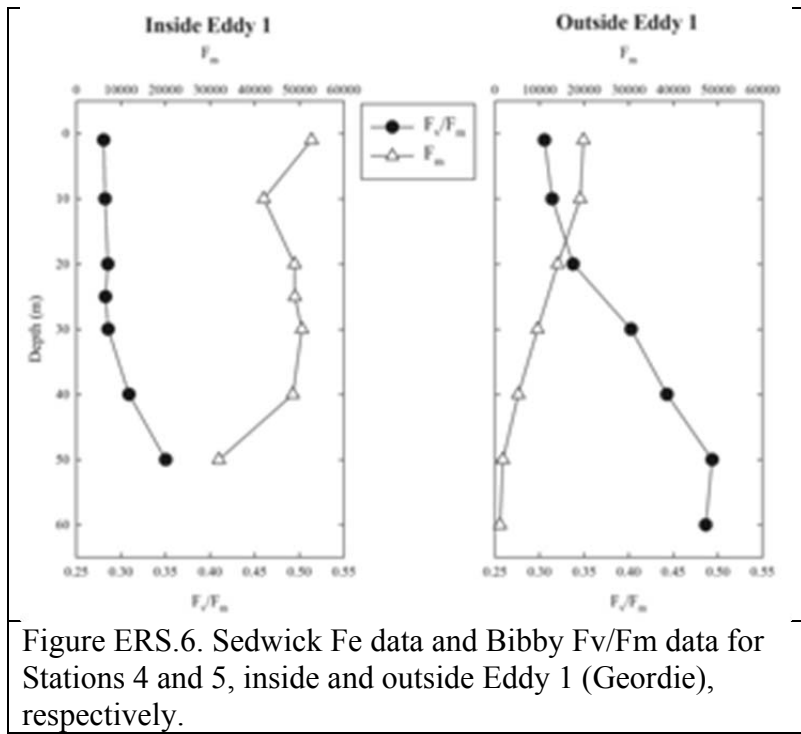
Figure ERS.6. Sedwick Fe data and Bibby Fv/Fm data for Stations 4 and 5, inside and outside Eddy 1 (Geordie), respectively.
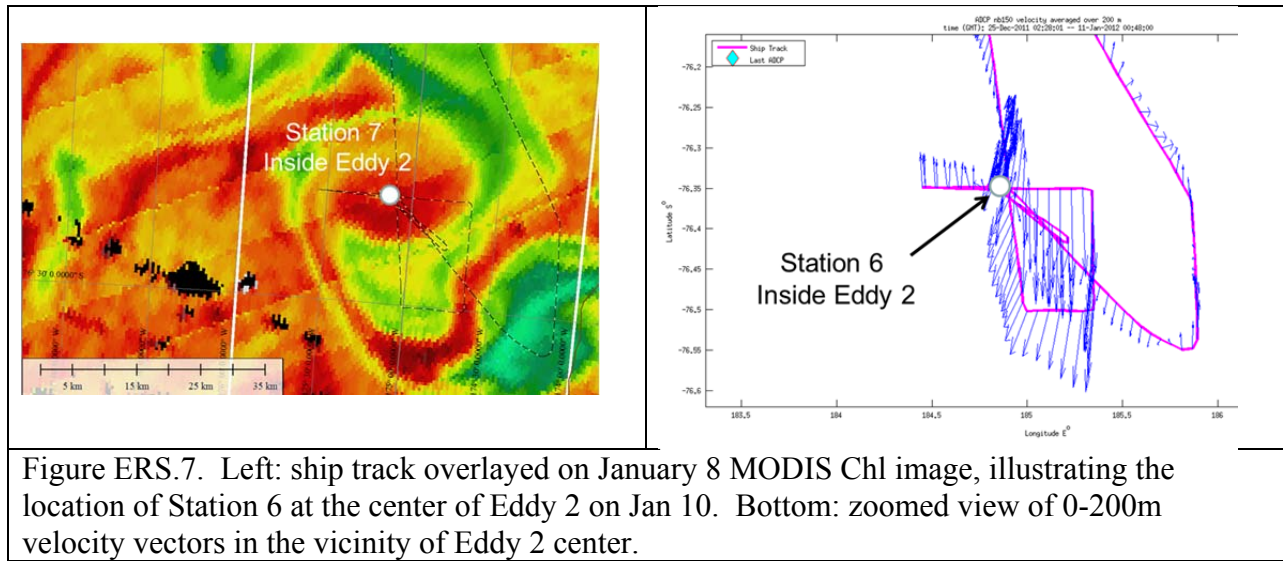
Figure ERS.7. Left: ship track overlayed on January 8 MODIS Chl image, illustrating the location of Station 6 at the center of Eddy 2 on Jan 10. Bottom: zoomed view of 0-200m velocity vectors in the vicinity of Eddy 2 center.
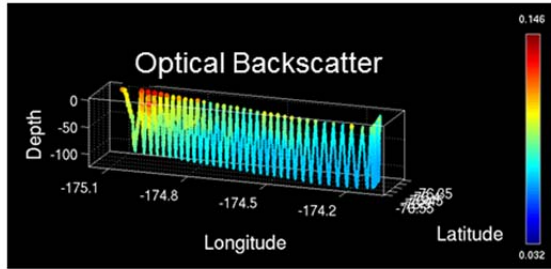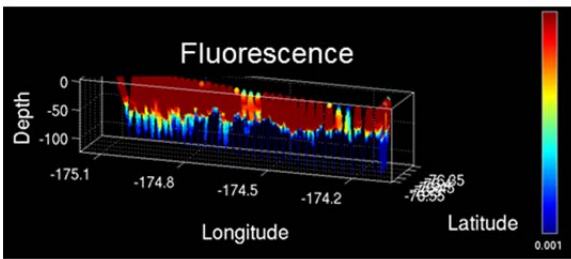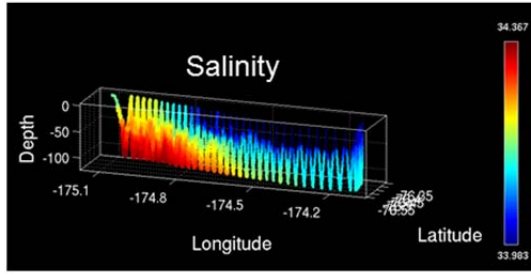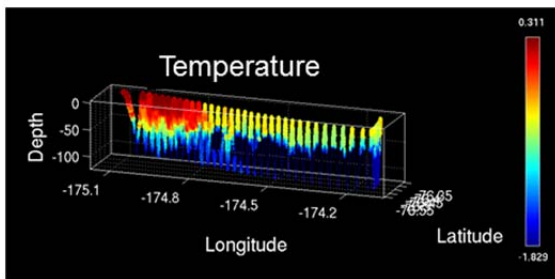
Figure ERS.8. Radial VPR survey of eddy 2, starting at eddy center and proceeding SE and then slightly N.

Figure ERS.9. Sample VPR images from radial survey of eddy 2.
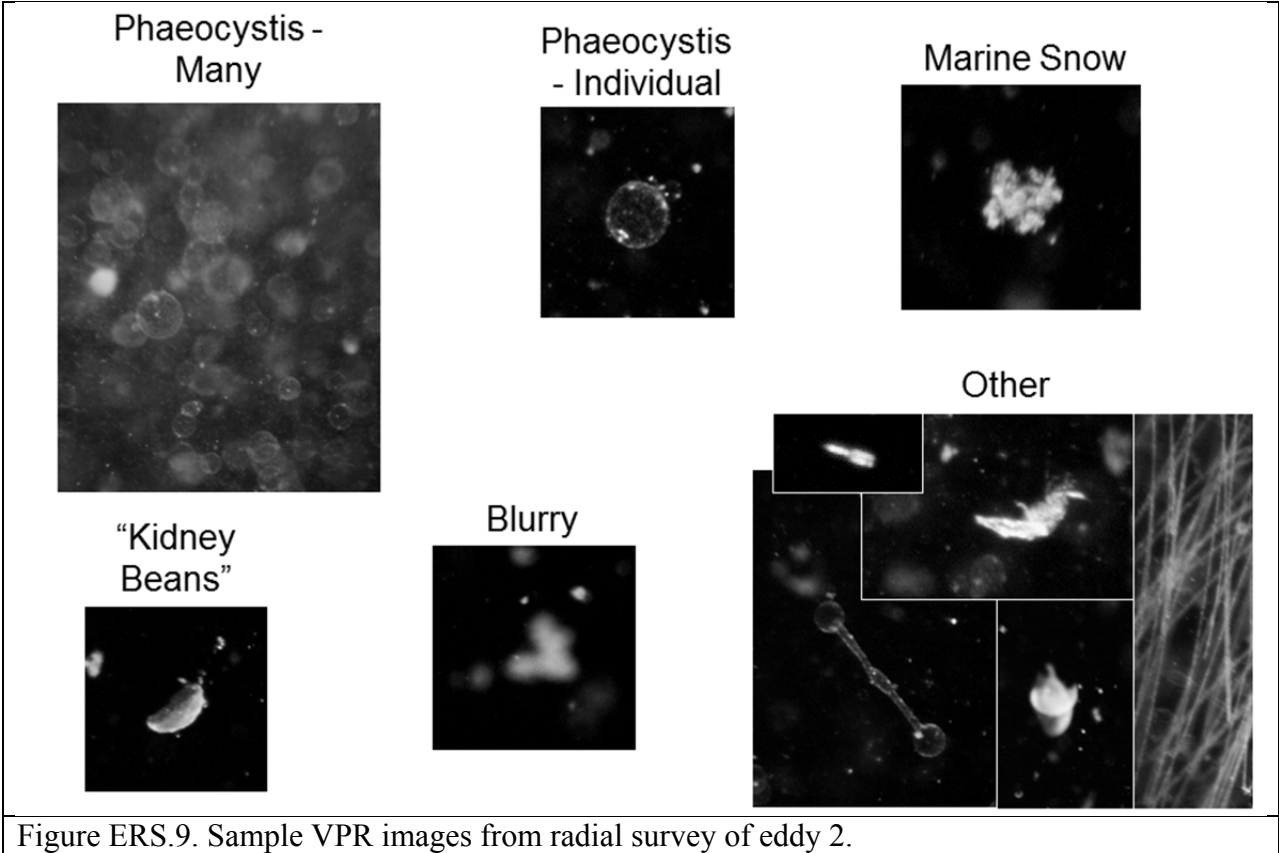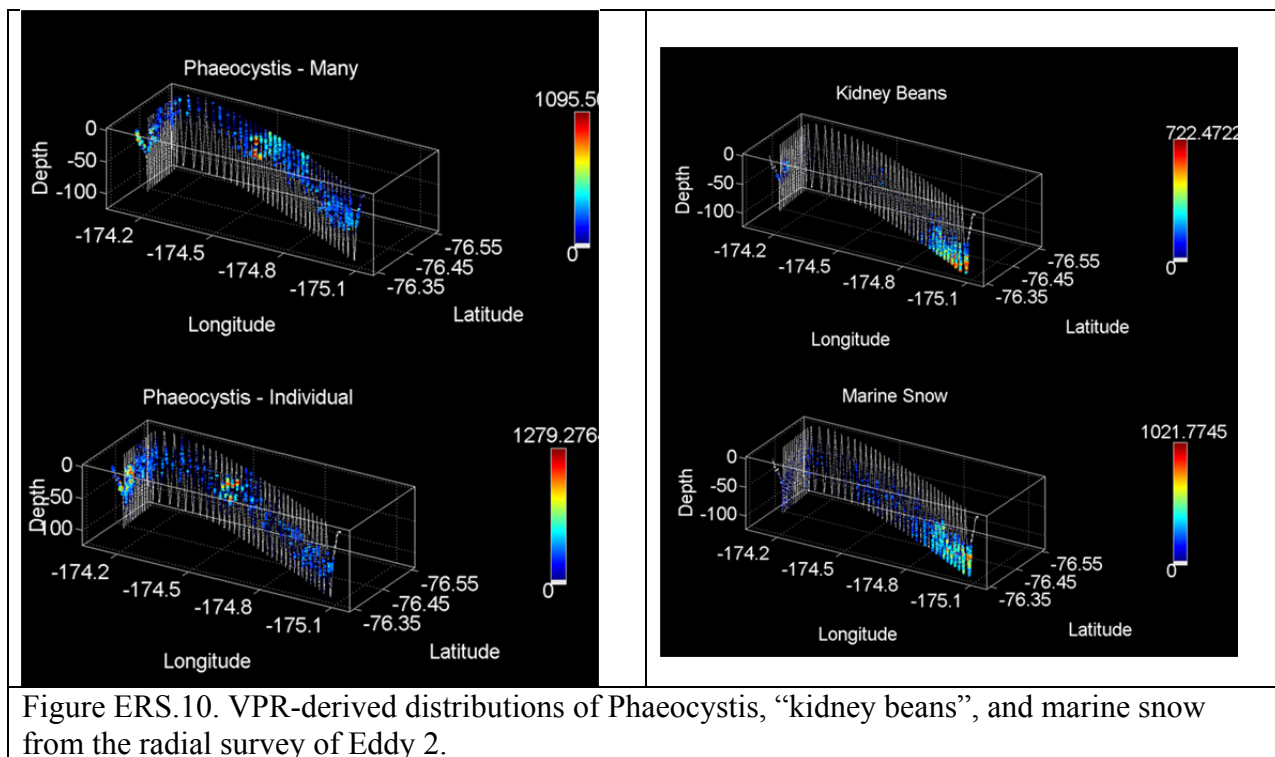
Figure ERS.10. VPR-derived distributions of Phaeocystis, "kidney beans", and marine snow from the radial survey of Eddy 2.
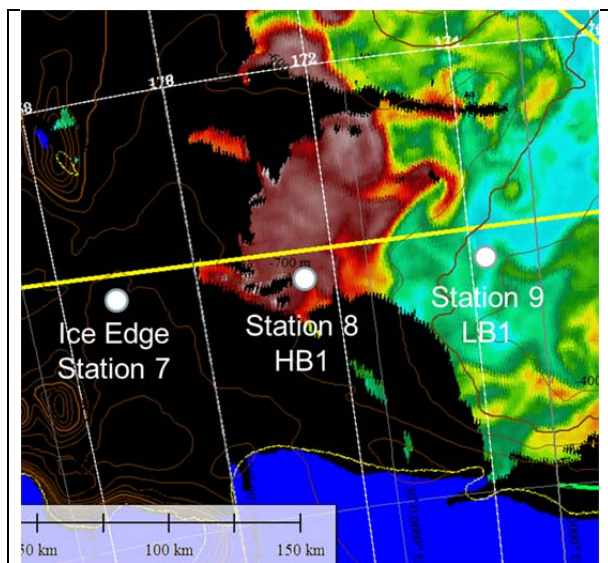
Figure WRS.1. Locations of stations 8-10 overlayed on a MODIS Chl image.
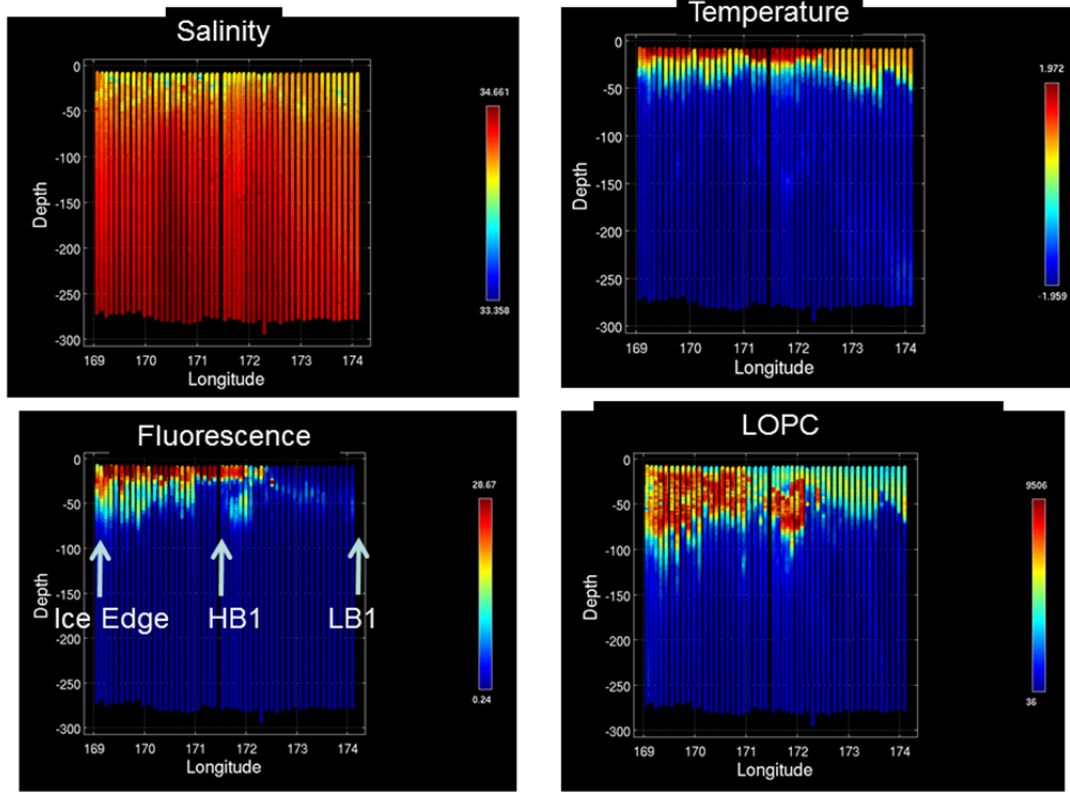
FigureWRS.2. MVP survey along the transect shown in Figure X. Positions of Stations 8, 9, 10 are indicated as "Ice Edge", HB1, and LB1, respectively.
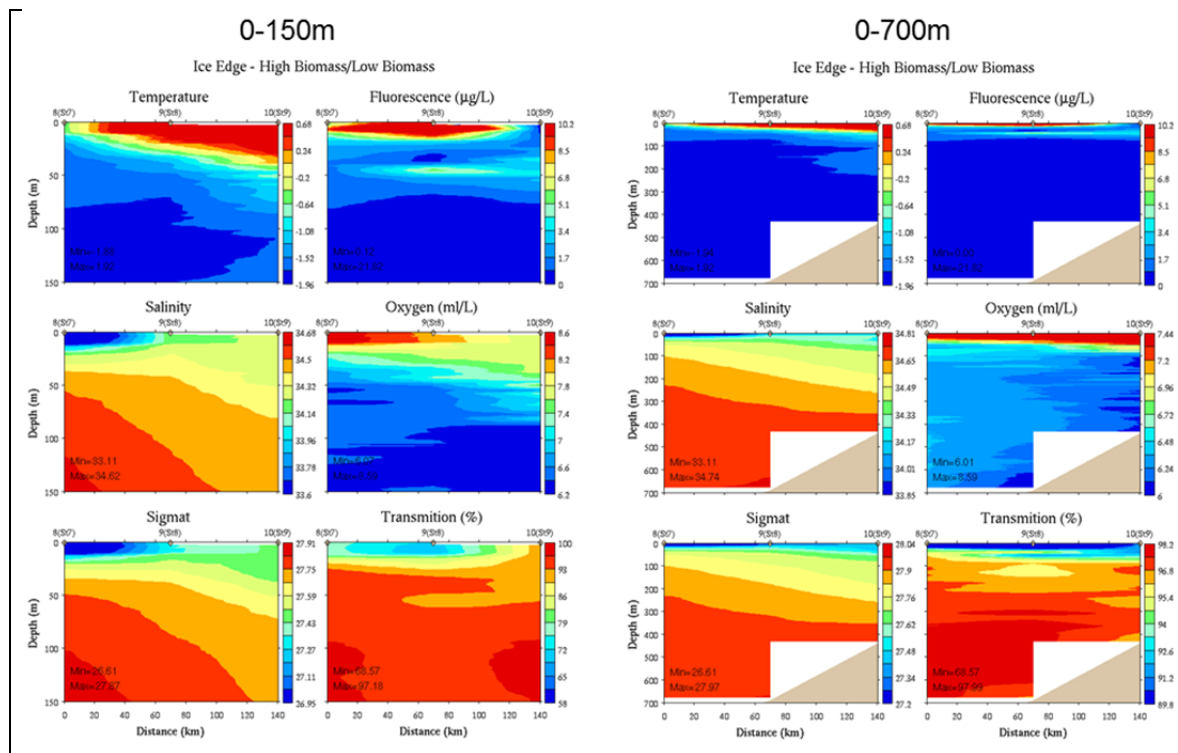
Figure WRS.3. CTD transect from the ice edge to high biomass to low biomass.
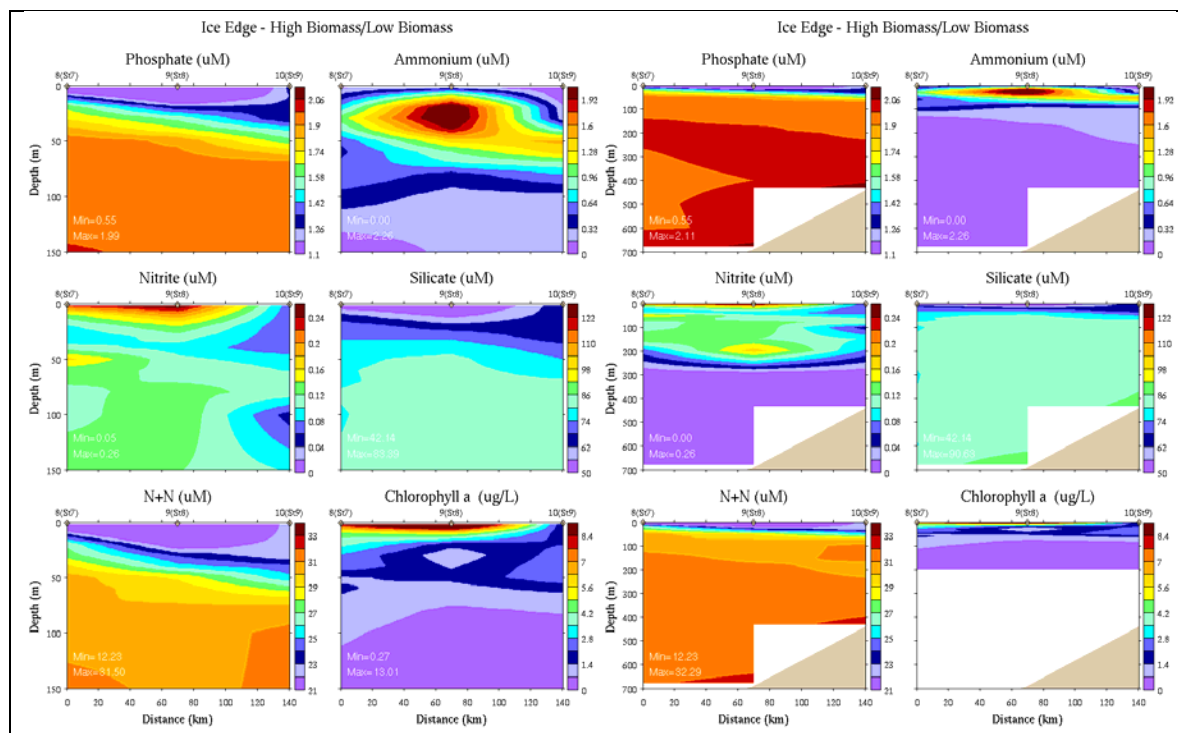
Figure WRS.4. Nutrient sections from the ice edge to high biomass to low biomass.

34
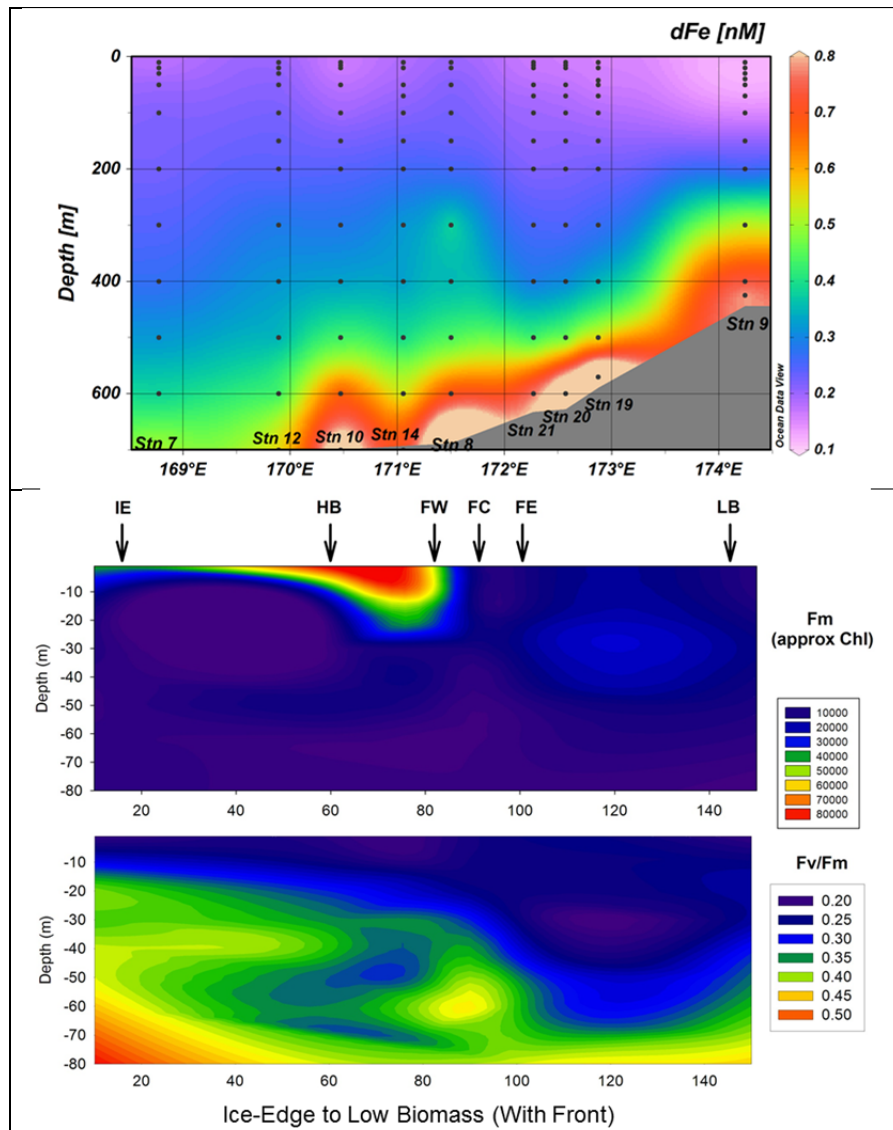
Figure WRS.5. Transects of dissolved iron (top), Fm (middle), and Fv/Fm (bottom) from the ice edge to the low biomass region.
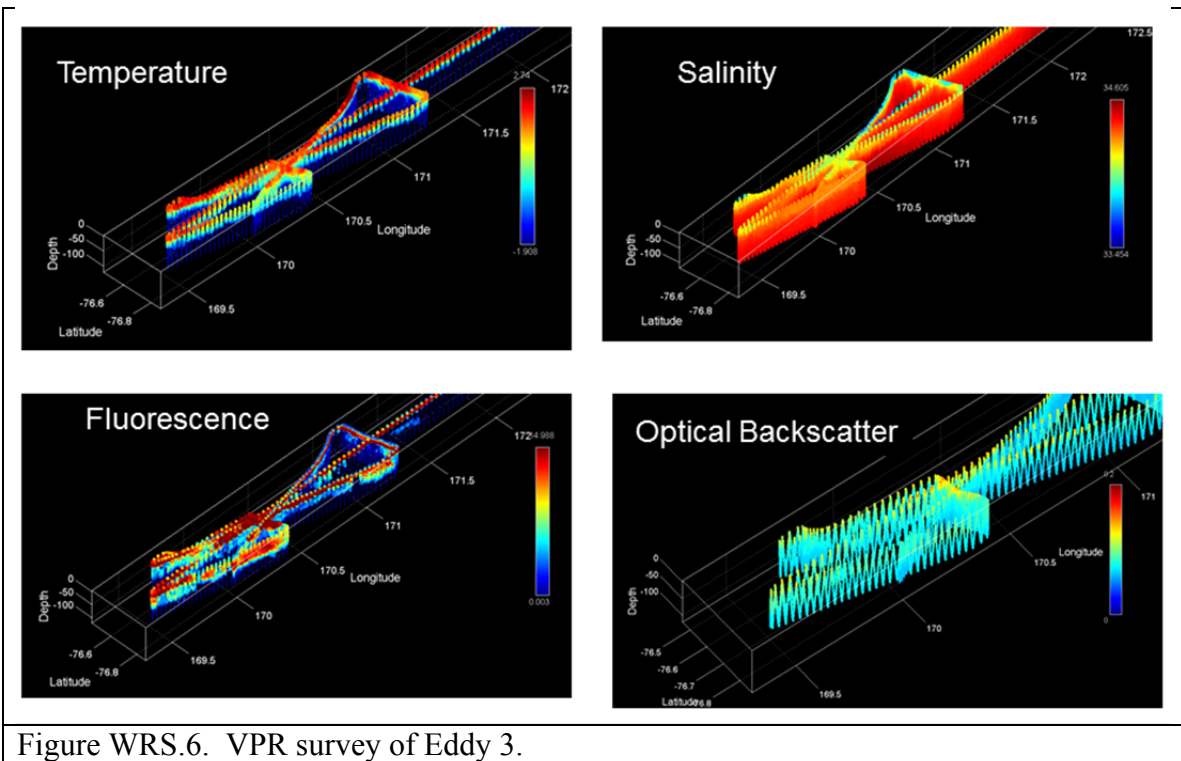
Figure WRS.6. VPR survey of Eddy 3.
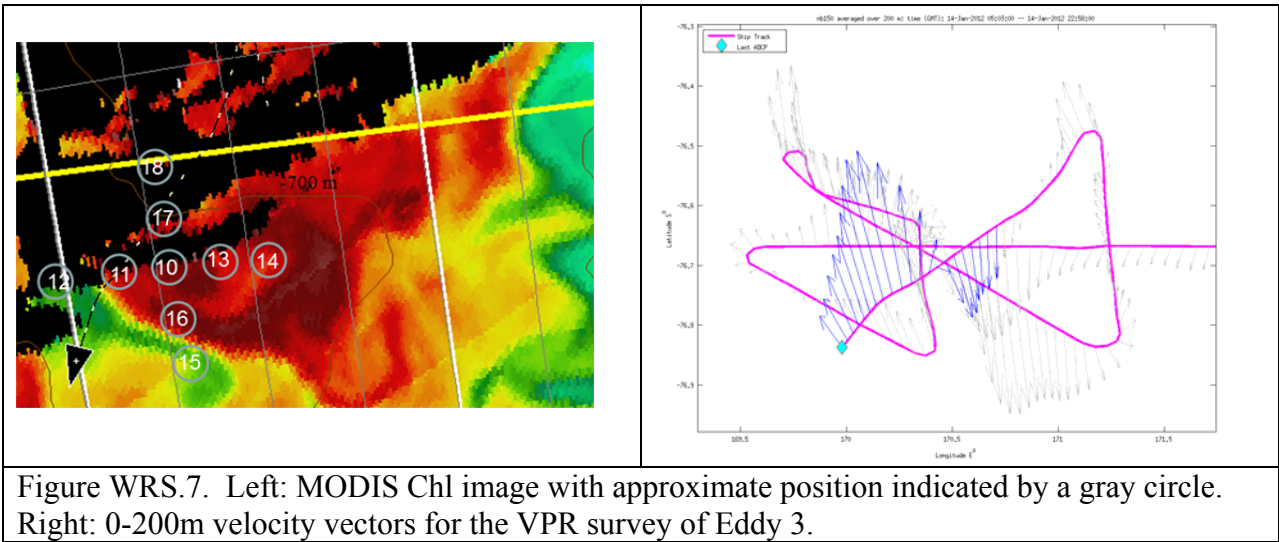
Figure WRS.7. Left: MODIS Chl image with approximate position indicated by a gray circle.
Right: 0-200m velocity vectors for the VPR survey of Eddy 3.
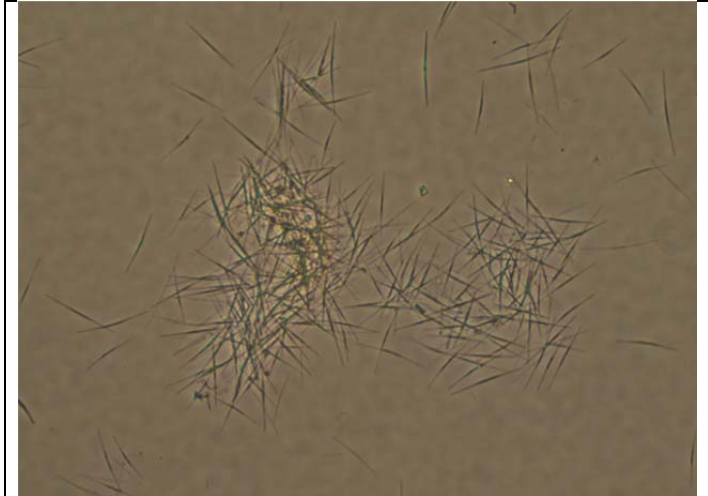
Figure WRS.8. Microscopic images from Hai showing the diatom abundant at stations 8 and 9, perhaps of the genus *Cylindrotheca* or *Nitzchia*.

Figure WRS.9. East-west CTD transect across Eddy 3 for the first occupation, Jan 15-16.

Figure WRS.10. Nutrient and chlorophyll concentrations from the east-west CTD transect across Eddy 3 for the first occupation, Jan 15-16.
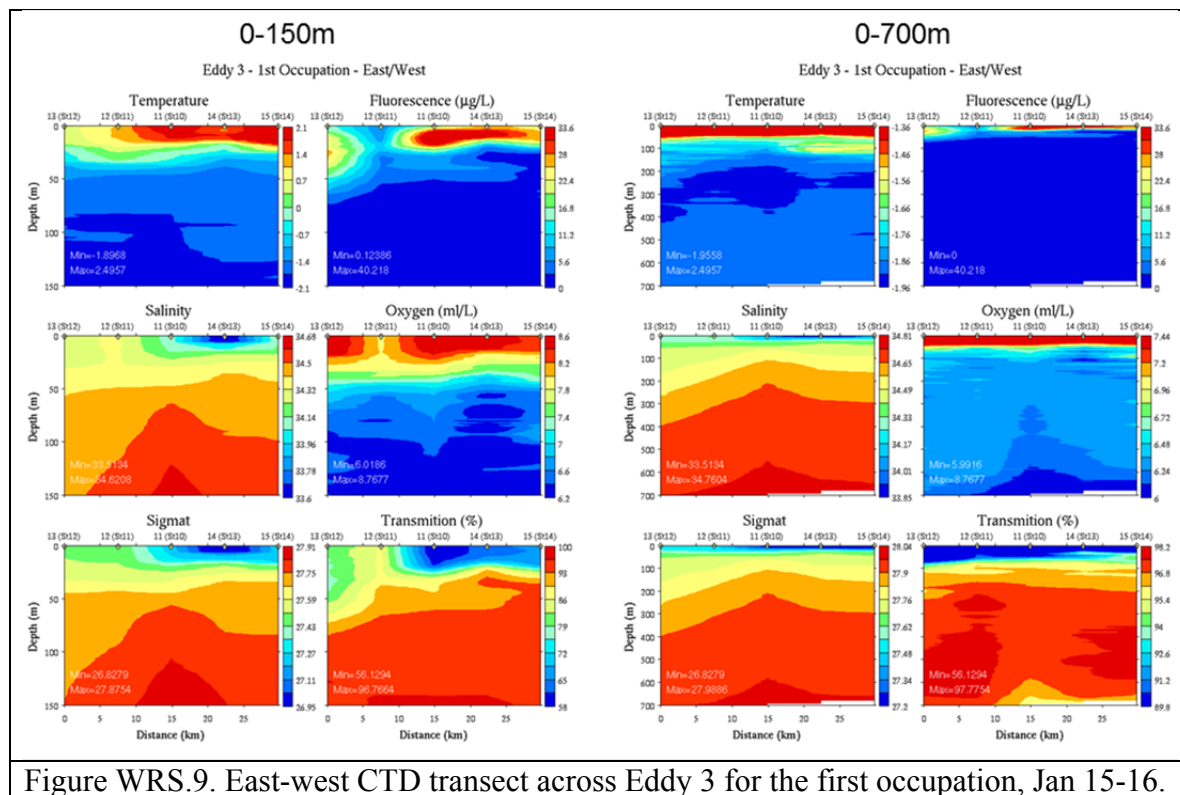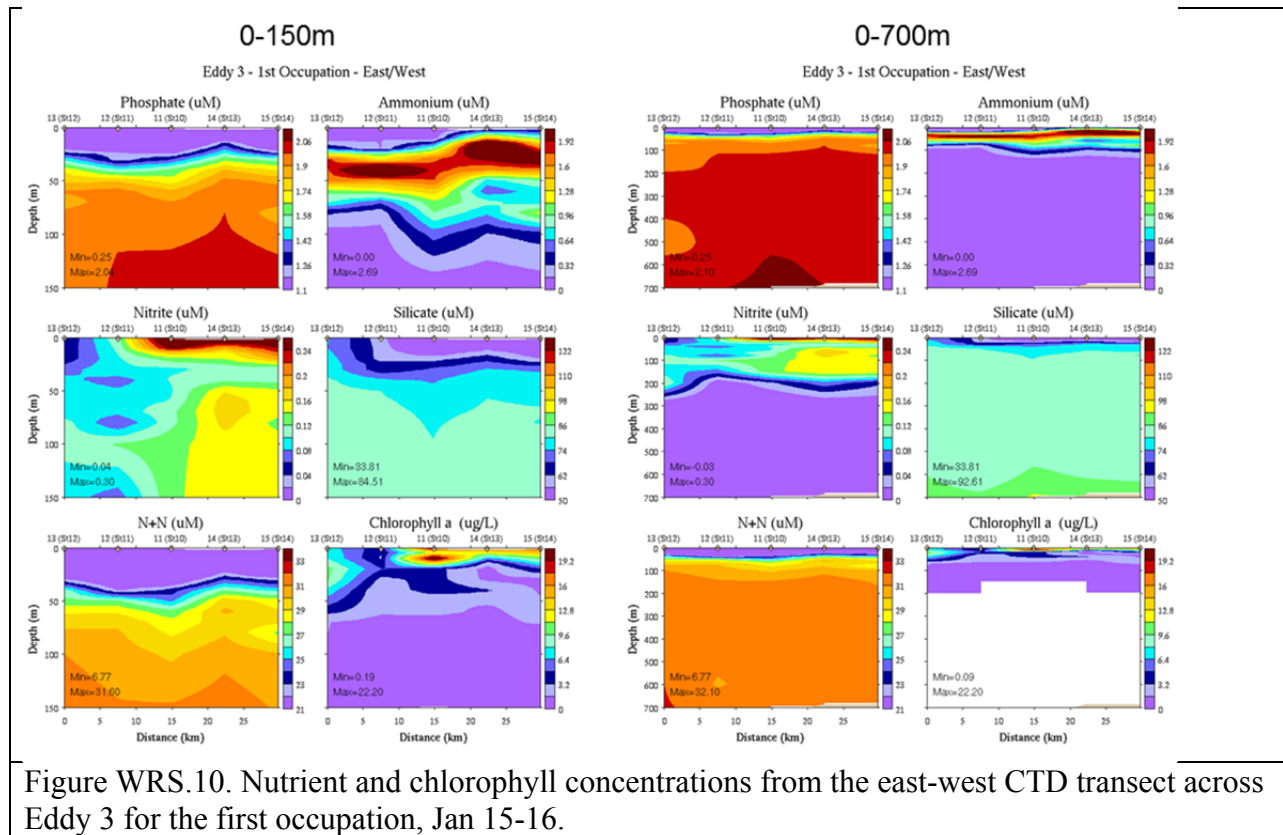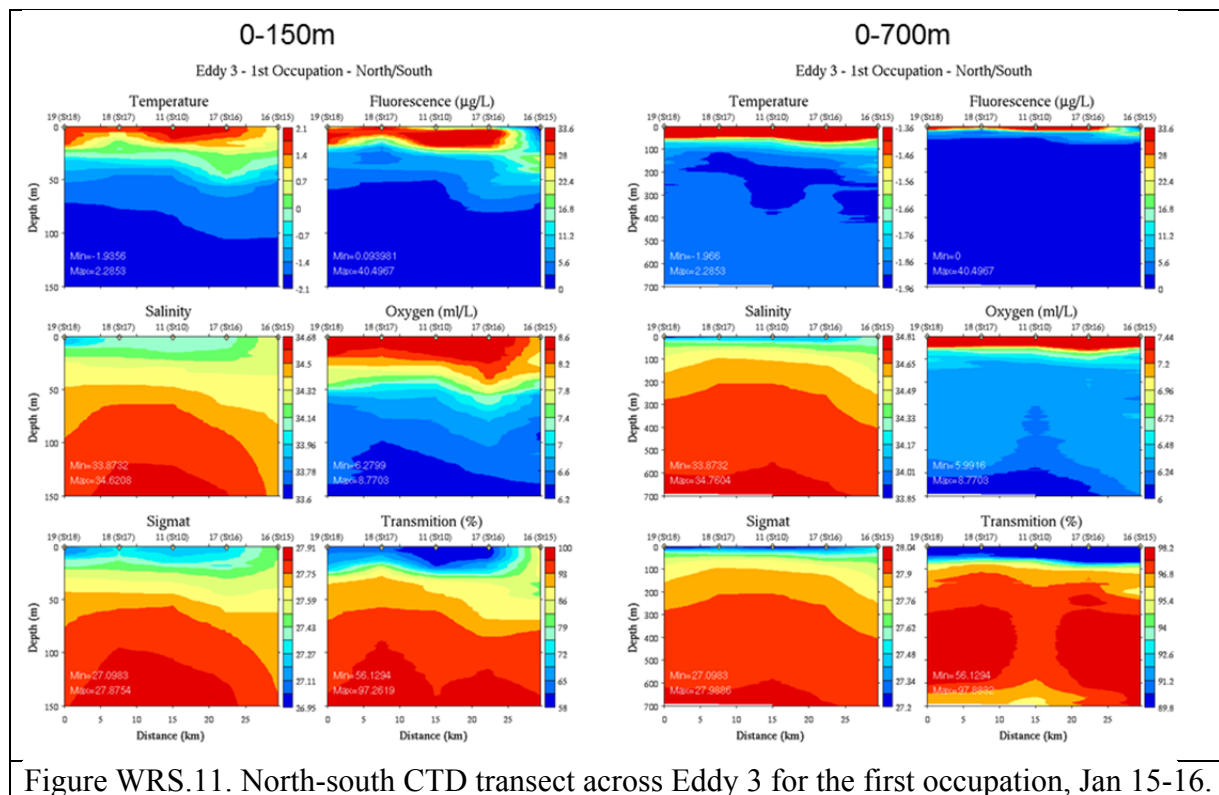
Figure WRS.11. North-south CTD transect across Eddy 3 for the first occupation, Jan 15-16.
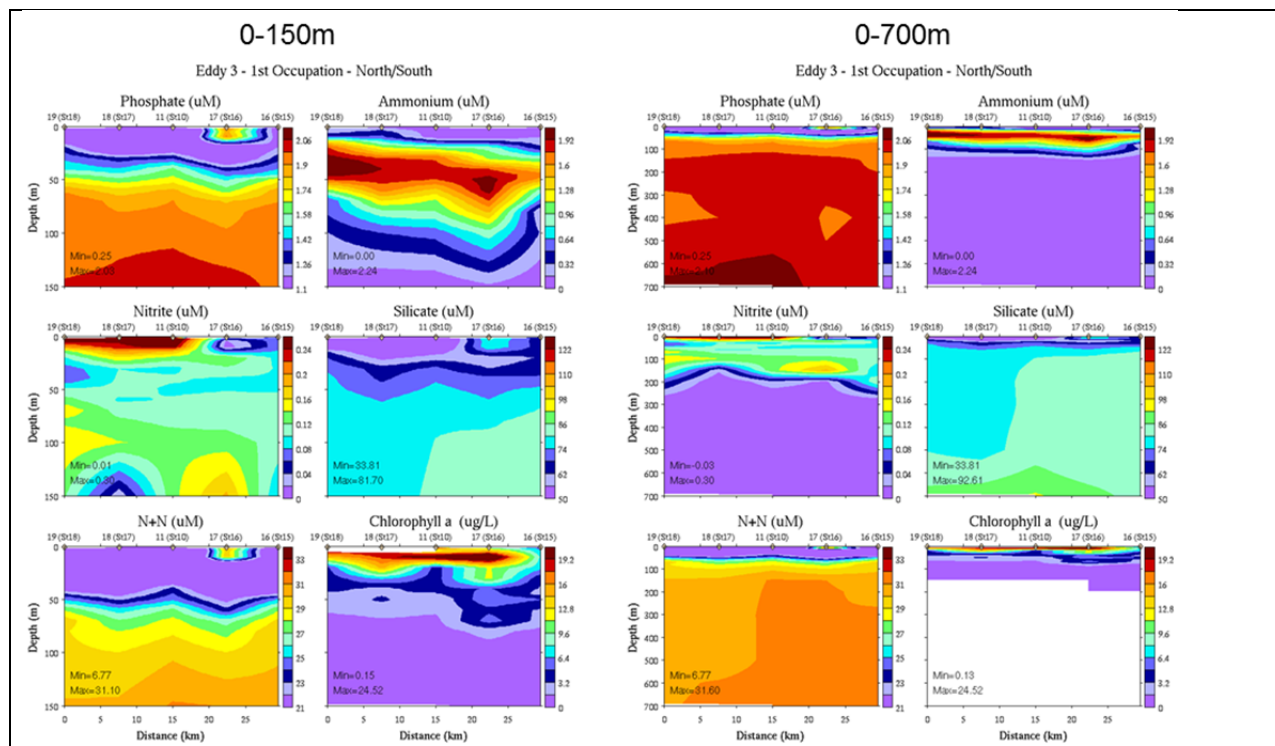
Figure WRS.12. Nutrient and chlorophyll concentrations from the north-south CTD transect across Eddy 3 for the first occupation, Jan 15-16.
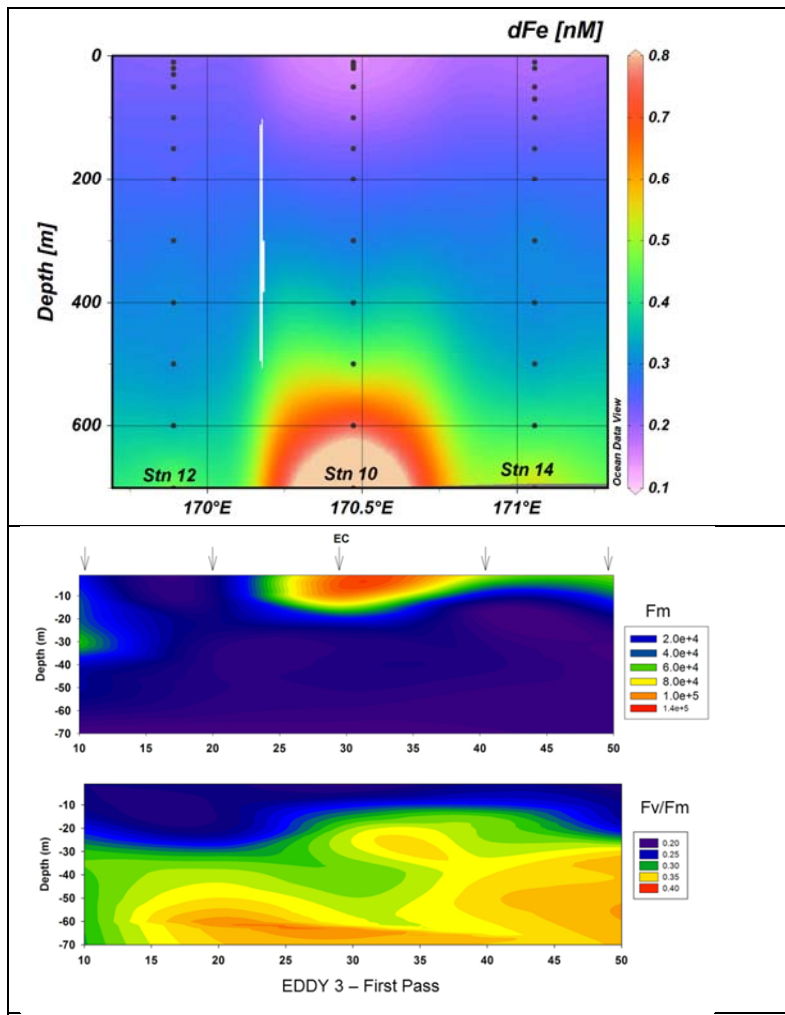
Figure WRS.13. Dissolved iron concentration along first the east-west transect of Eddy 3, Jan 15-16.
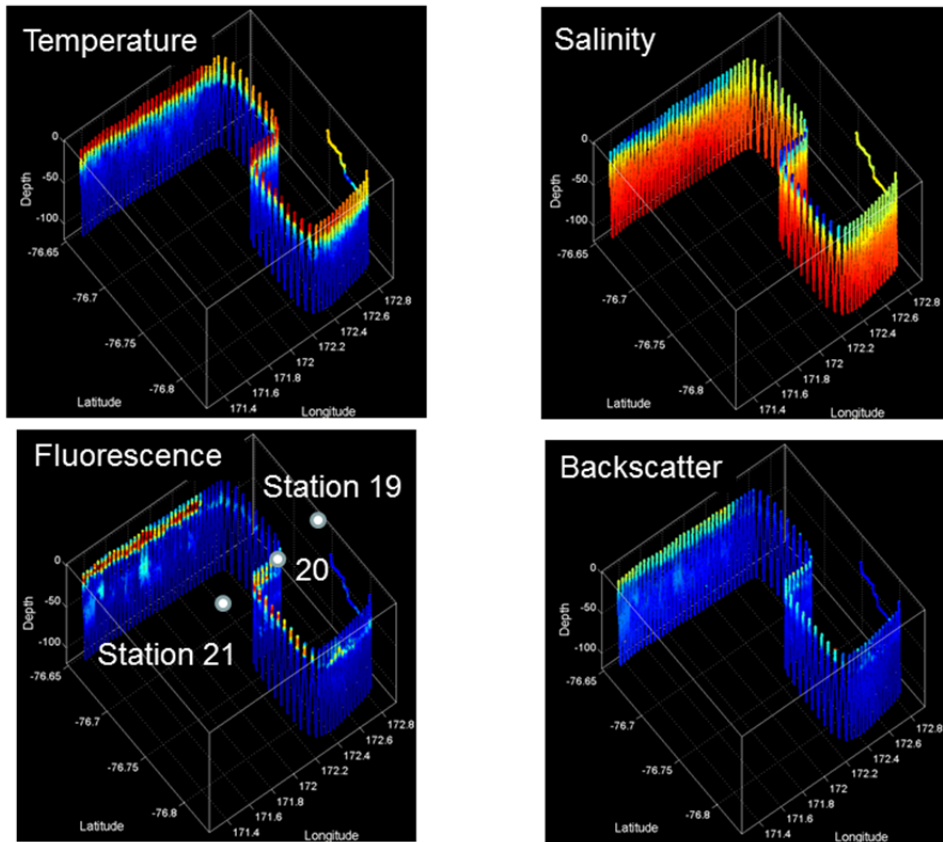
Figure WRS.14. VPR survey of the frontal region between high-biomass and low-biomass regions (VPR5).
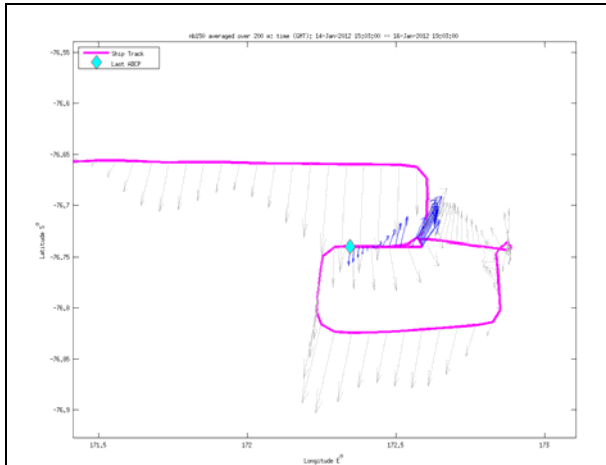
Figure WRS.15. 0-200m velocity vectors for the VPR survey of the frontal region between high-biomass and low-biomass regions (VPR5).
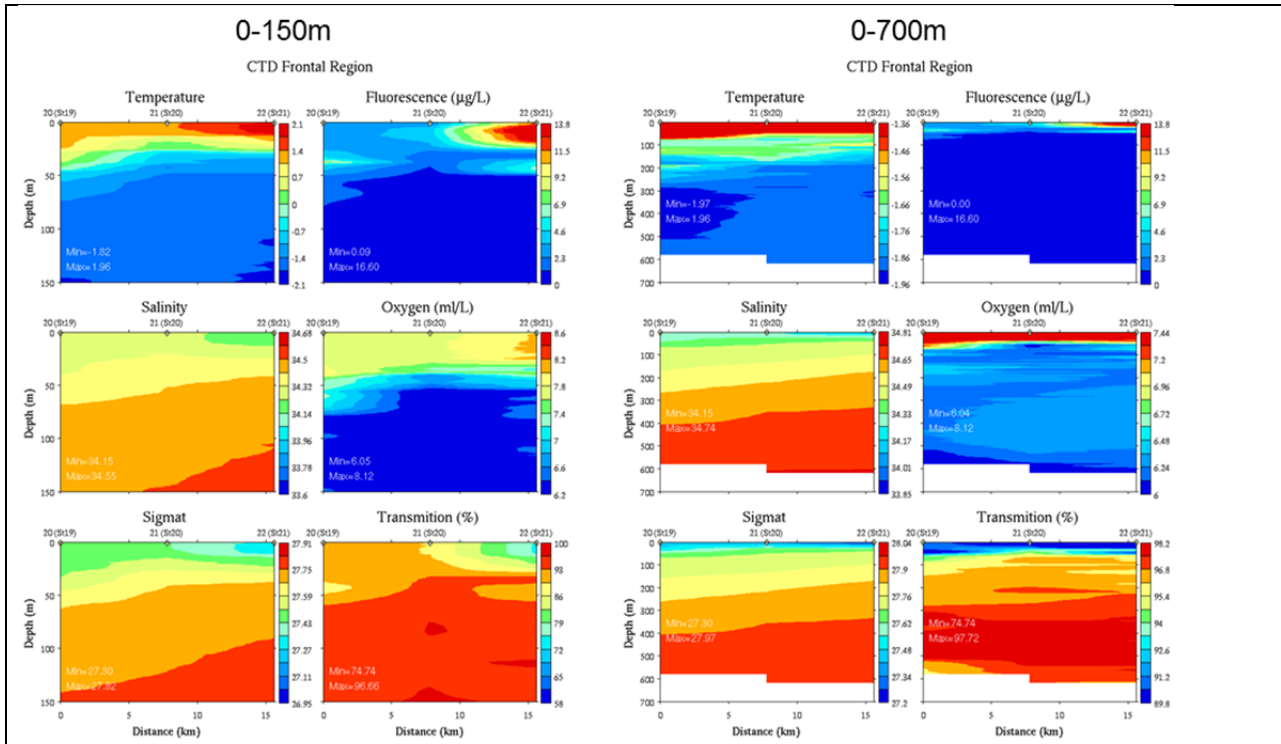
Figure WRS.16. East-west CTD transect across the frontal region mapped in Figure . Note the axes are such that east is to the left and west is to the right.
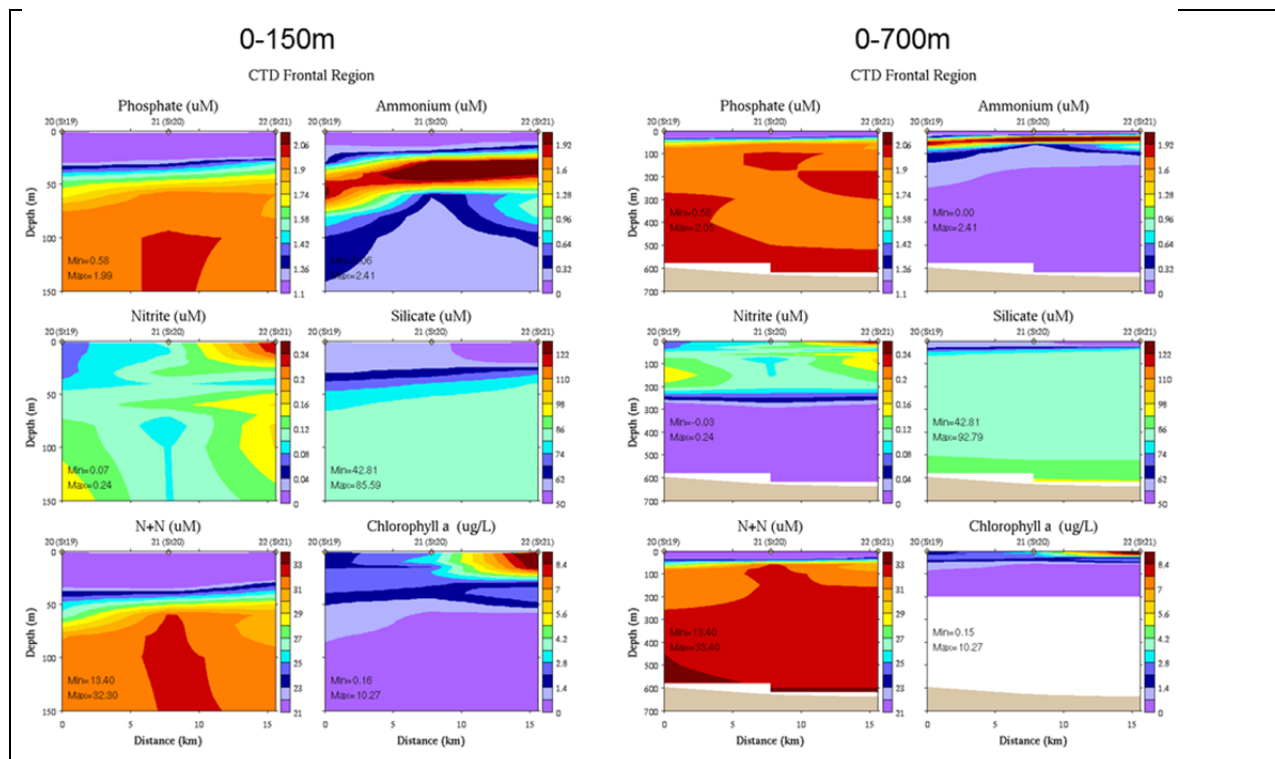
Figure WRS.17. Nutrient and chlorophyll concentrations from the east-west CTD transect across the frontal region mapped in Figure . Note the axes are such that east is to the left and west is to the right.
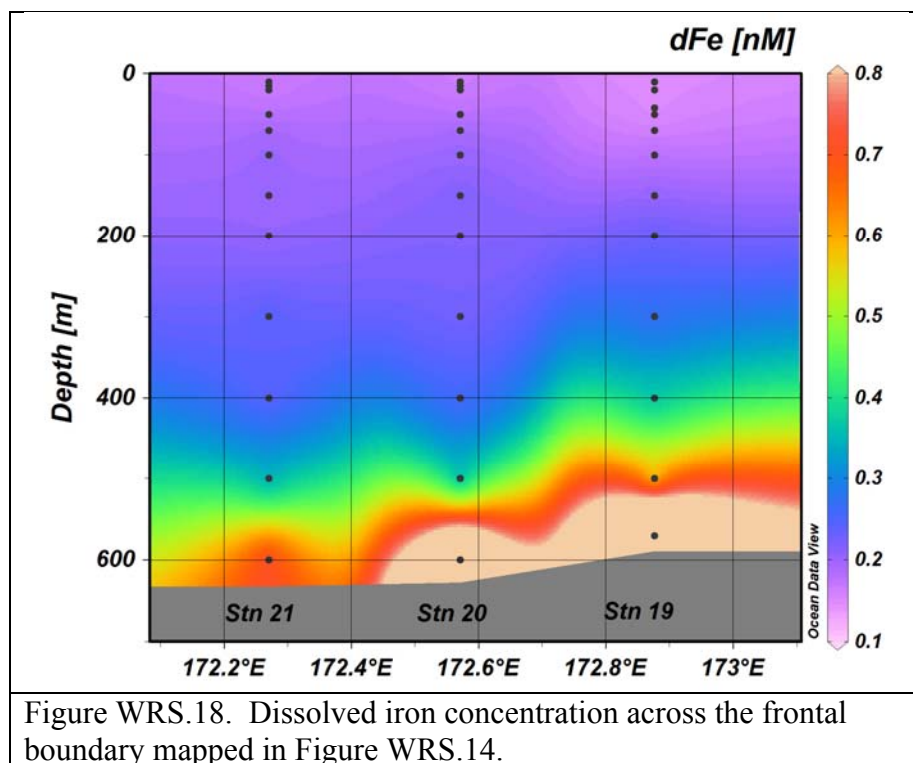
Figure WRS.18. Dissolved iron concentration across the frontal boundary mapped in Figure WRS.14.
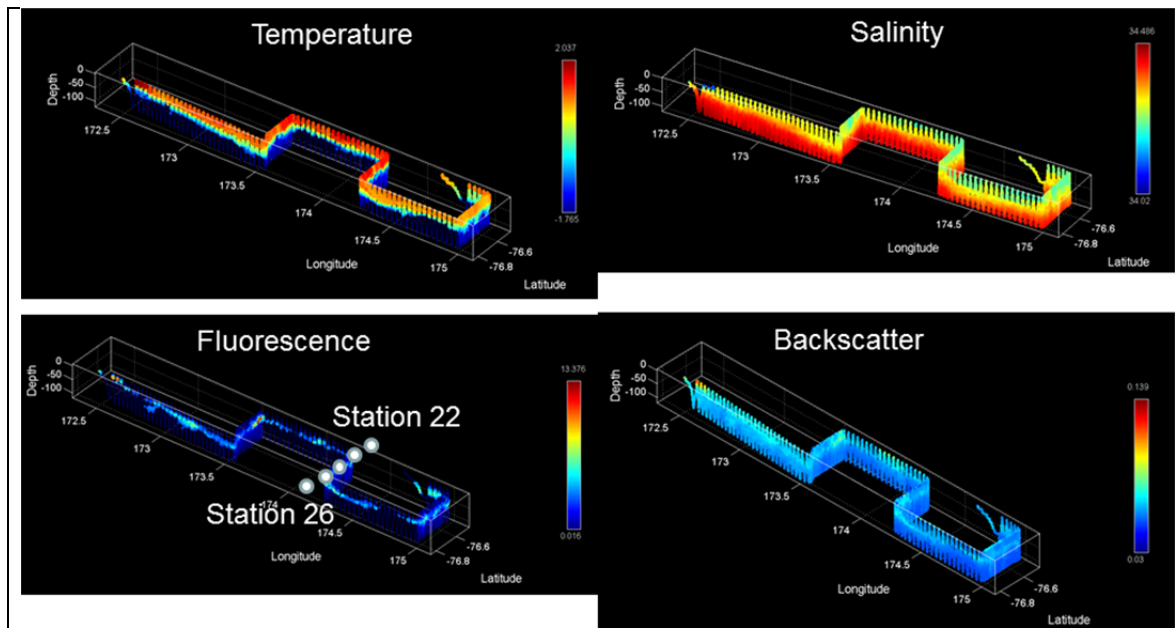
Figure WRS.19. VPR survey of the low-biomass region (VPR6).
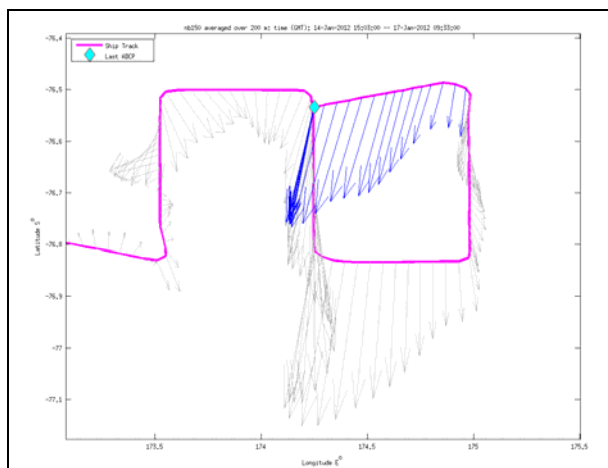
Figure WRS.20. 0-200m velocity vectors for the VPR survey of the low-biomass regions (VPR6).
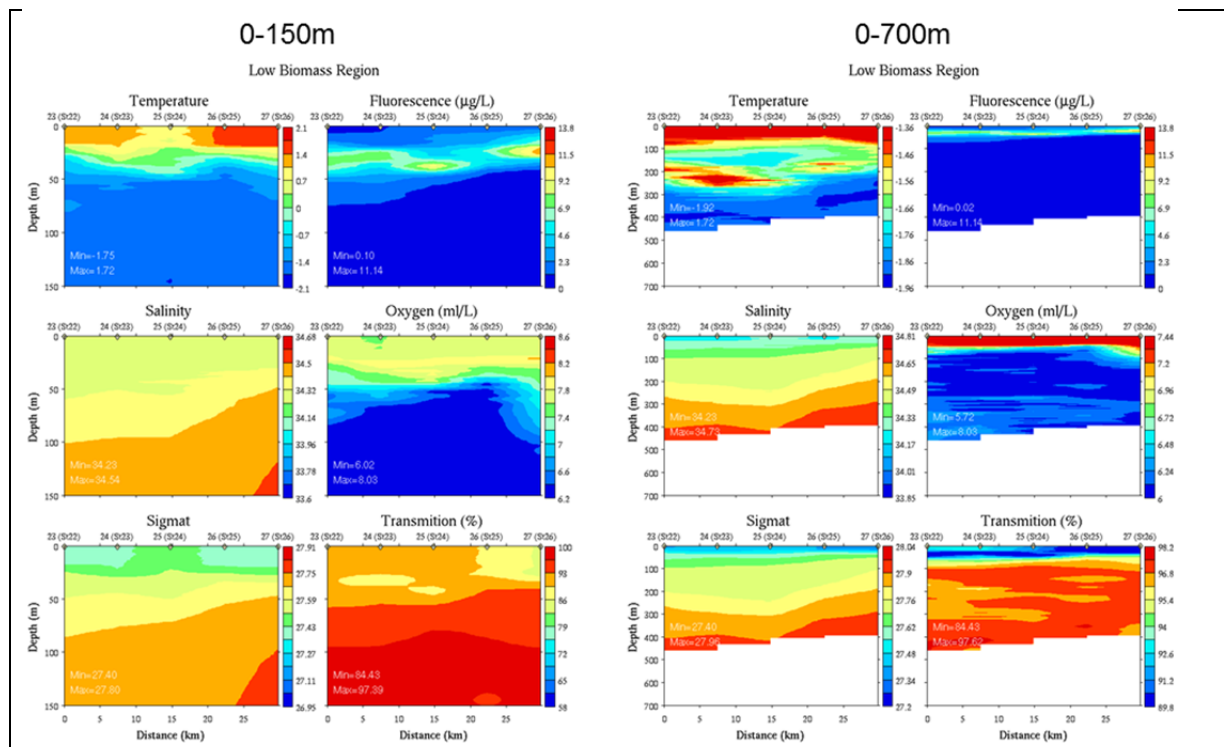
Figure WRS.21. North-south CTD transect across the low-biomass region mapped in Figure .
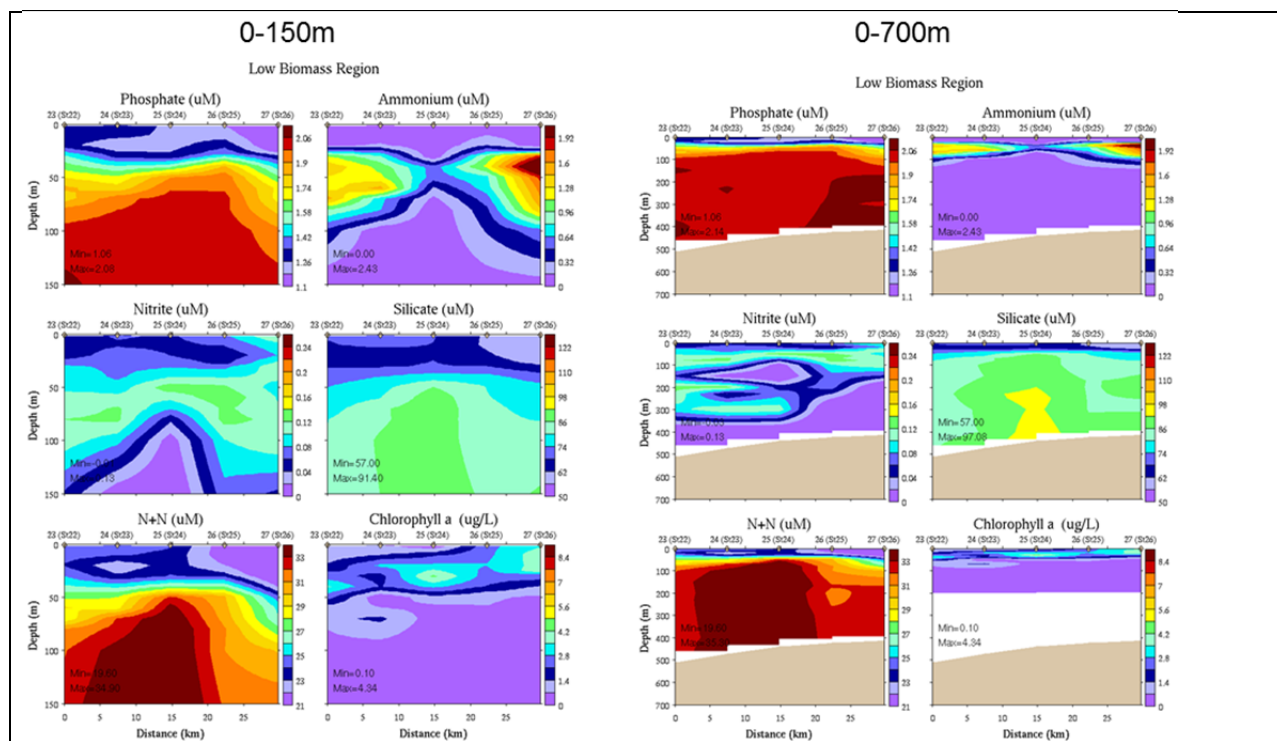
Figure WRS.22. Nutrient and chlorophyll concentrations from the north-south CTD transect across the low biomass region mapped in Figure .
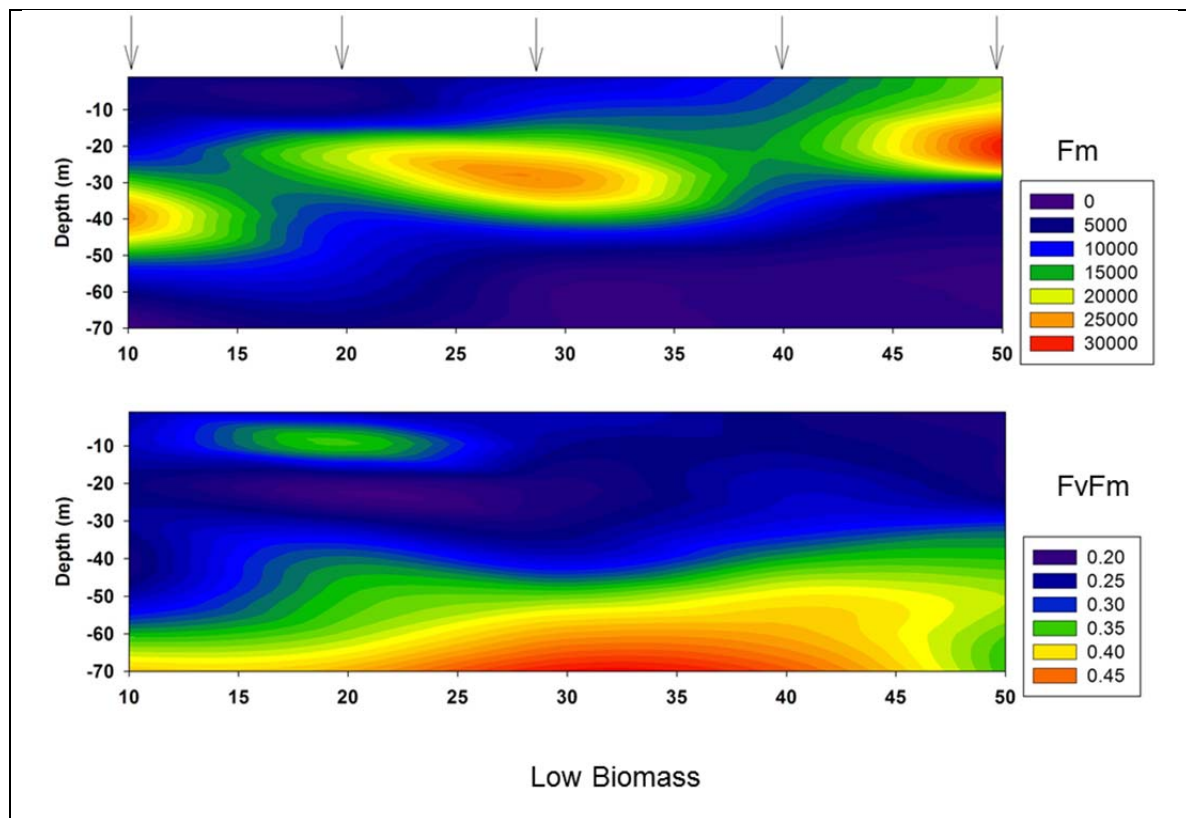
Figure WRS.23. Fm and Fv/Fm from the north-south CTD transect across the low biomass region mapped in Figure .
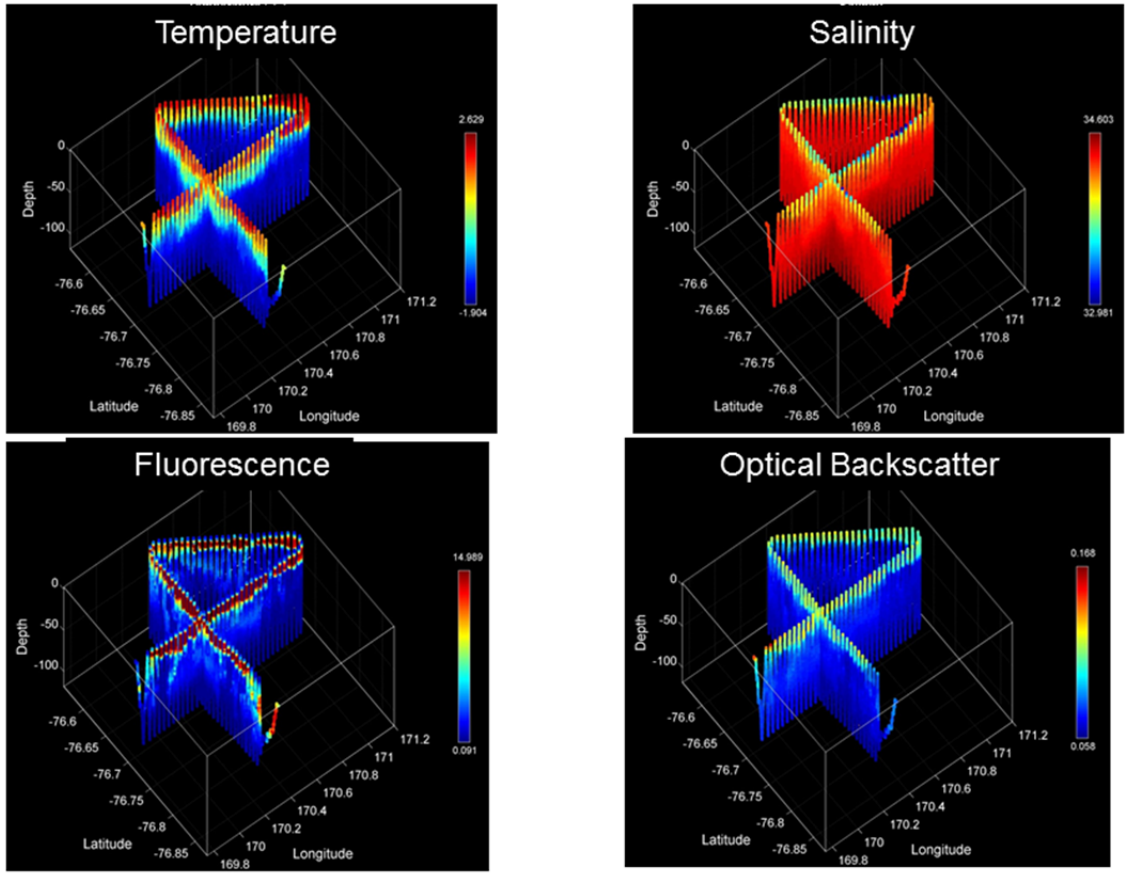
Figure WRS.24. Second VPR survey of Eddy 3 (VPR7).
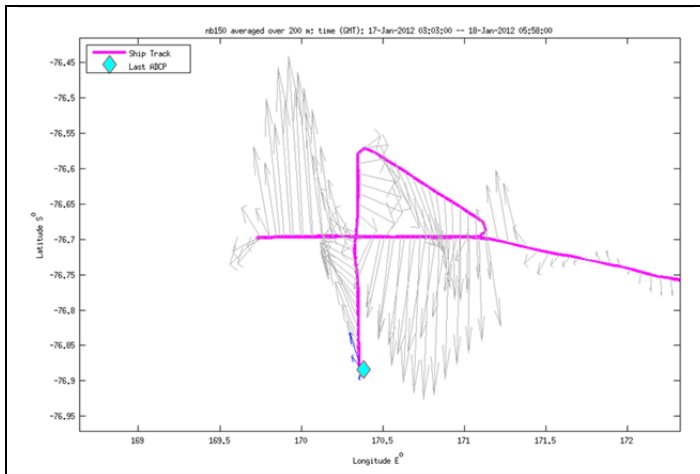
Figure WRS.25. 0-200m velocity vectors for the second VPR survey of Eddy 3 (VPR7).
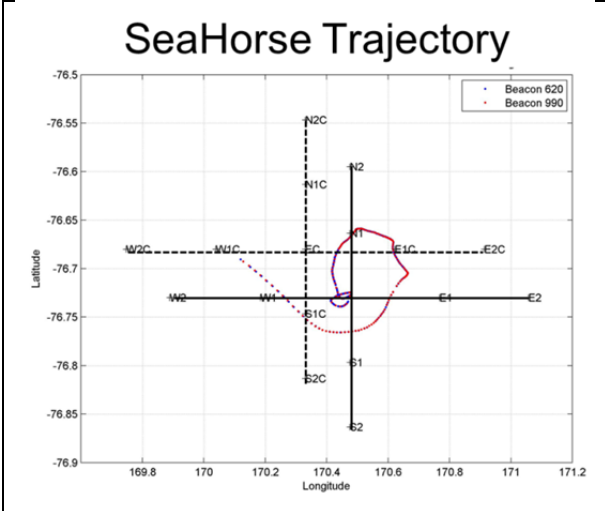
Figure WRS.26. SeaHorse trajectory relative to the first (solide) and second (dashed) CTD surveys of Eddy 3.
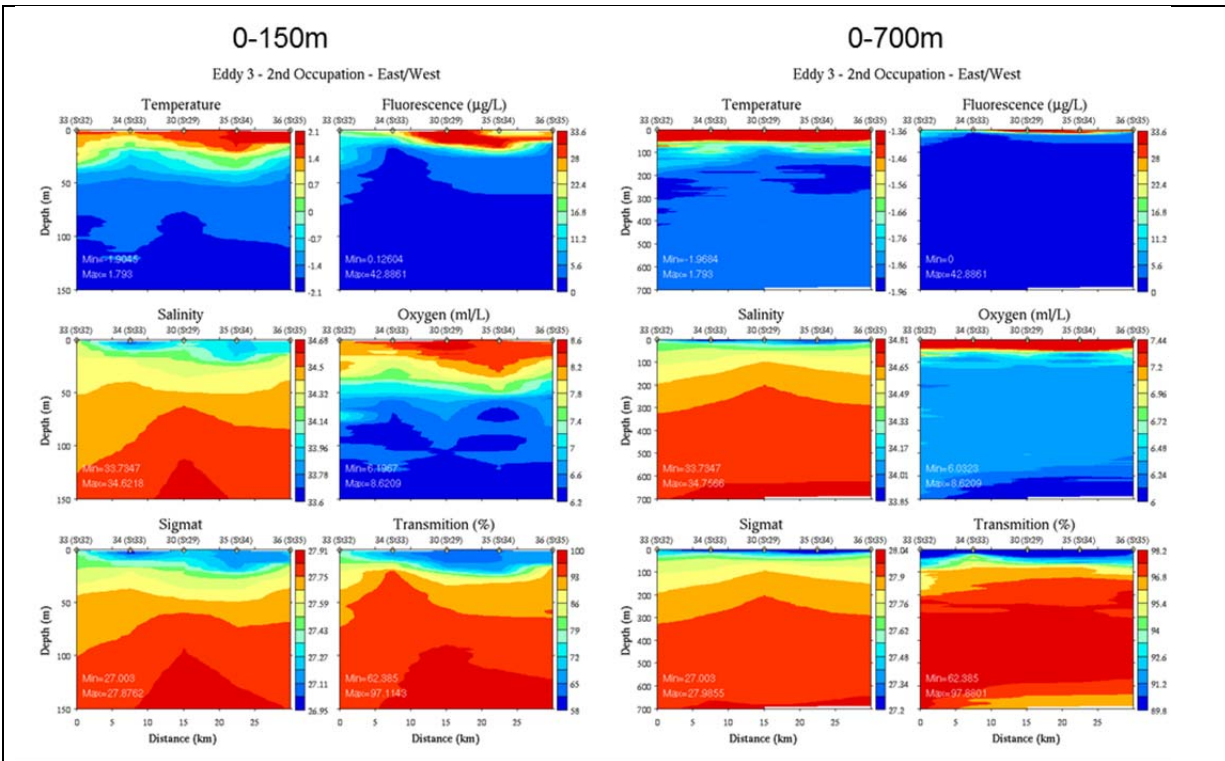
Figure WRS.27. East-west CTD transect across Eddy 3 for the second occupation, Jan 18-19.
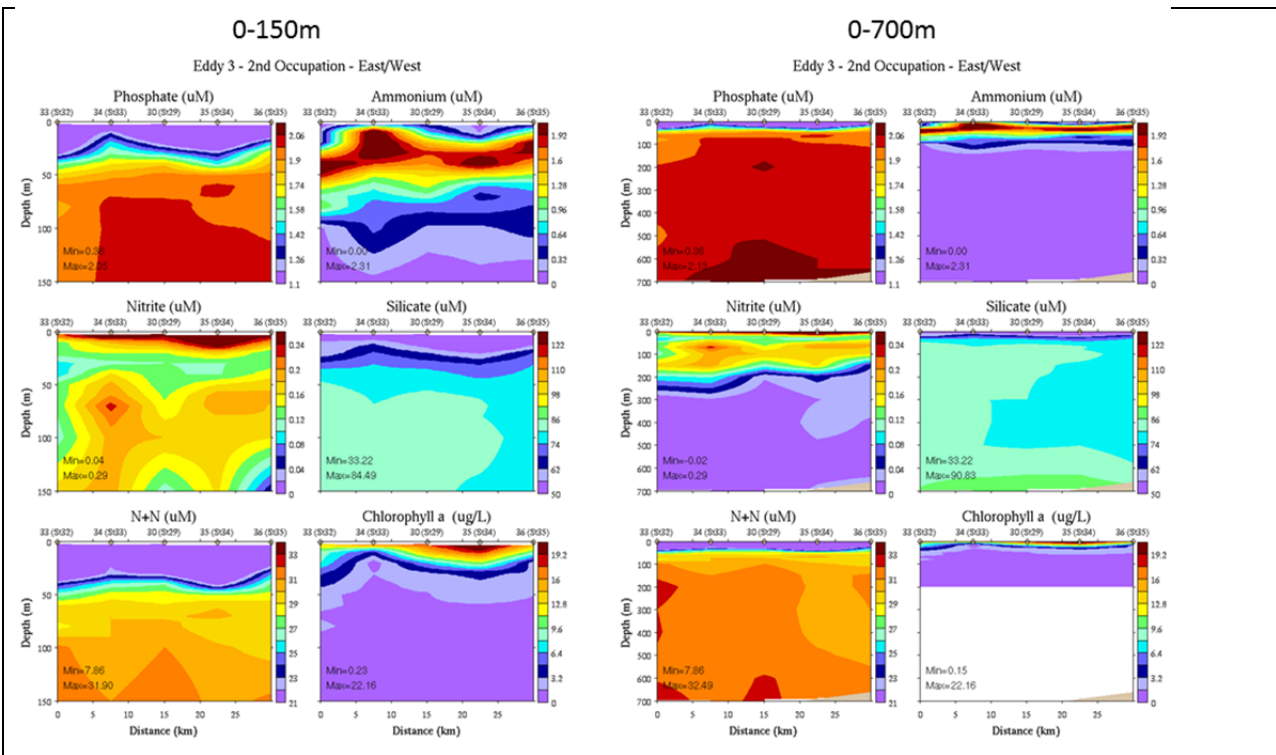
Figure WRS.28. Nutrient and chlorophyll concentrations from the east-west CTD transect across Eddy 3 for the second occupation, Jan 18-19.
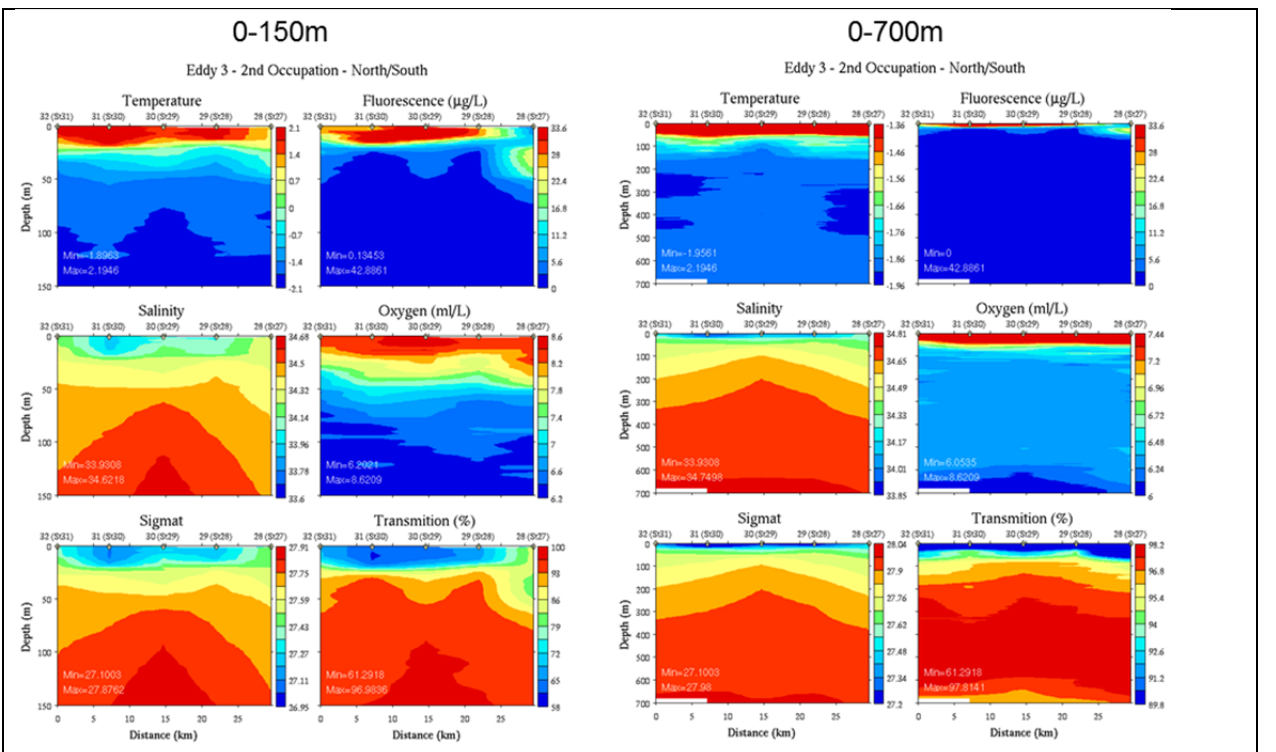
Figure WRS.29. North-south CTD transect across Eddy 3 for the second occupation, Jan 18-19.
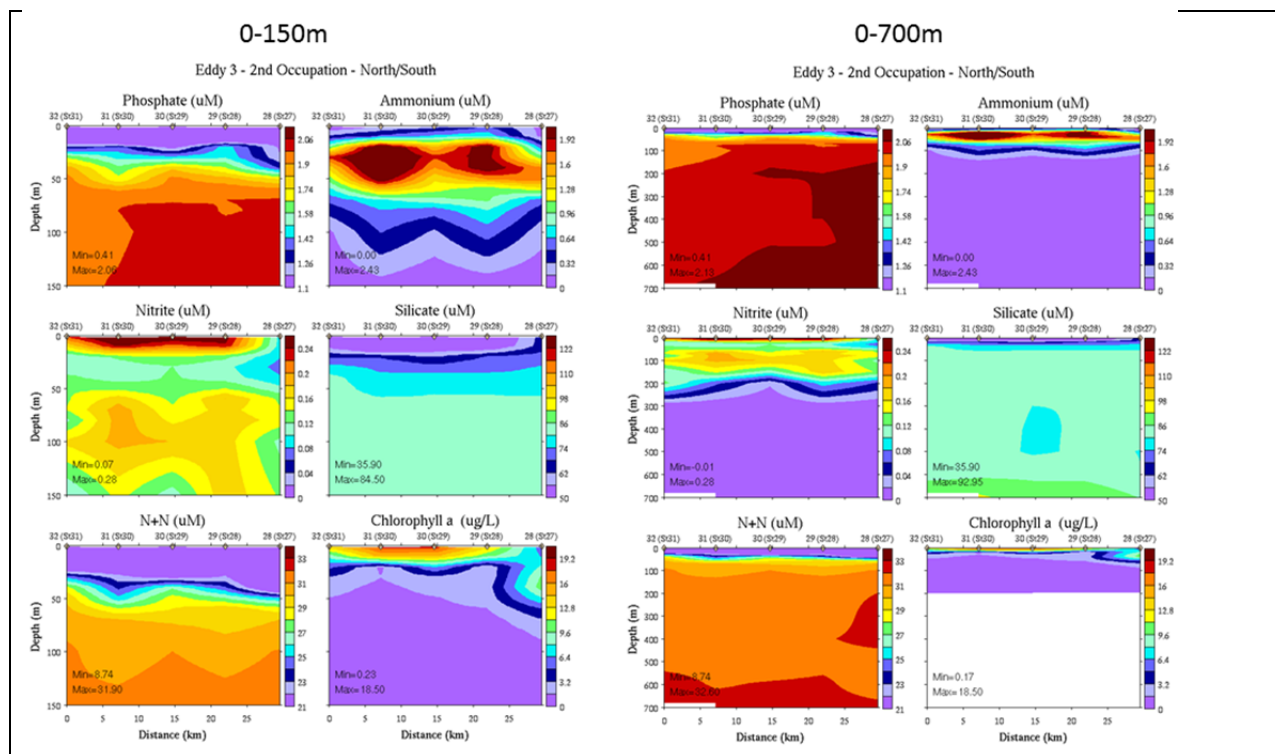
Figure WRS.30. Nutrient and chlorophyll concentrations from the north-south CTD transect across Eddy 3 for the second occupation, Jan 18-19.
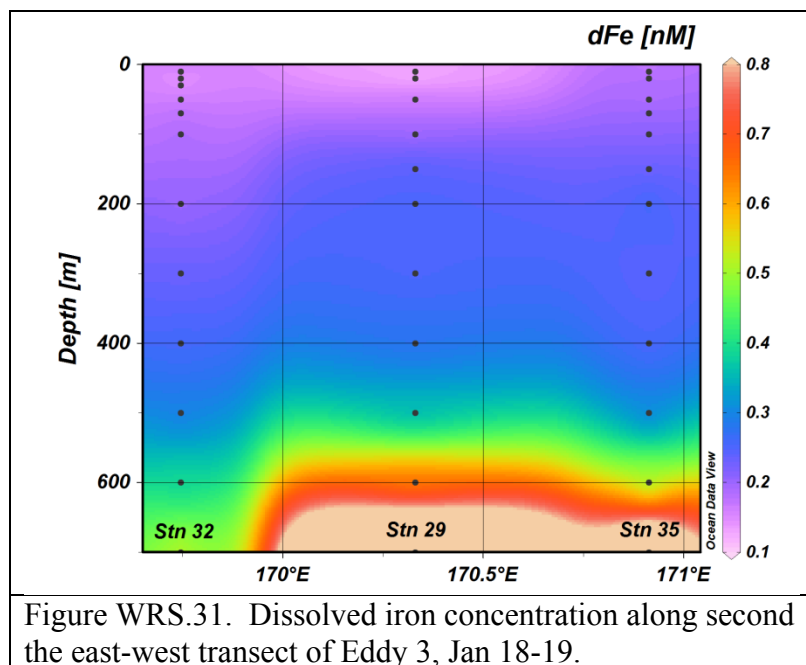
Figure WRS.31. Dissolved iron concentration along second the east-west transect of Eddy 3, Jan 18-19.
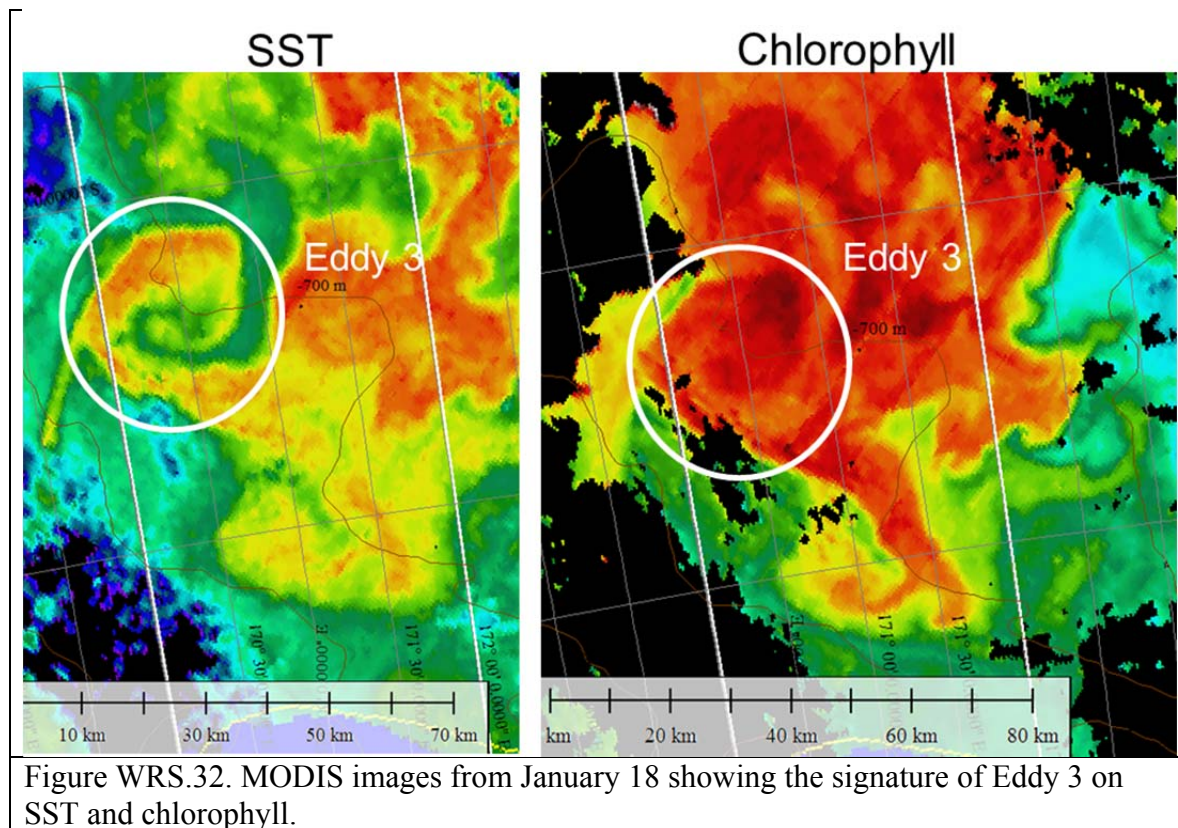
Figure WRS.32. MODIS images from January 18 showing the signature of Eddy 3 on SST and chlorophyll.
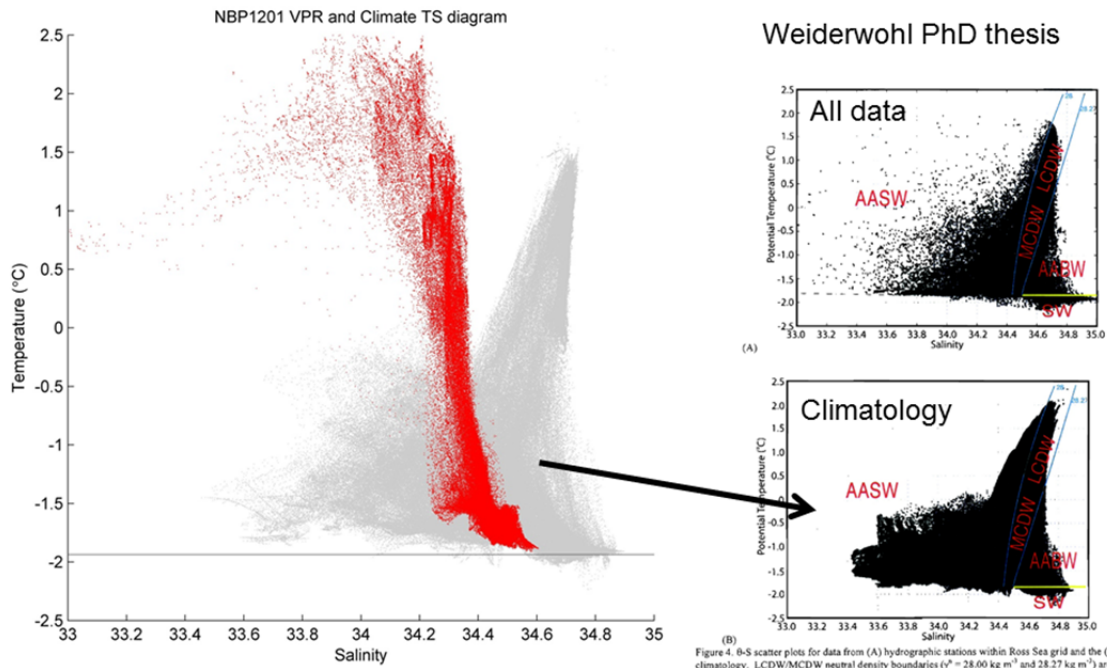
Figure WRS.33. Temperature-salinity characteristics from VPR tows 4-5-6-7 (red), which span the high-biomass region (including the waters of Eddy 3) as well as the low-biomass region. Gray dots are the Orsi and Weiderwohl (2009) climatology (lower right). All CTD measurements that went in to the climatology are indicated at the upper right. Source: Weiderwohl thesis, obtained from Mike Dinniman.
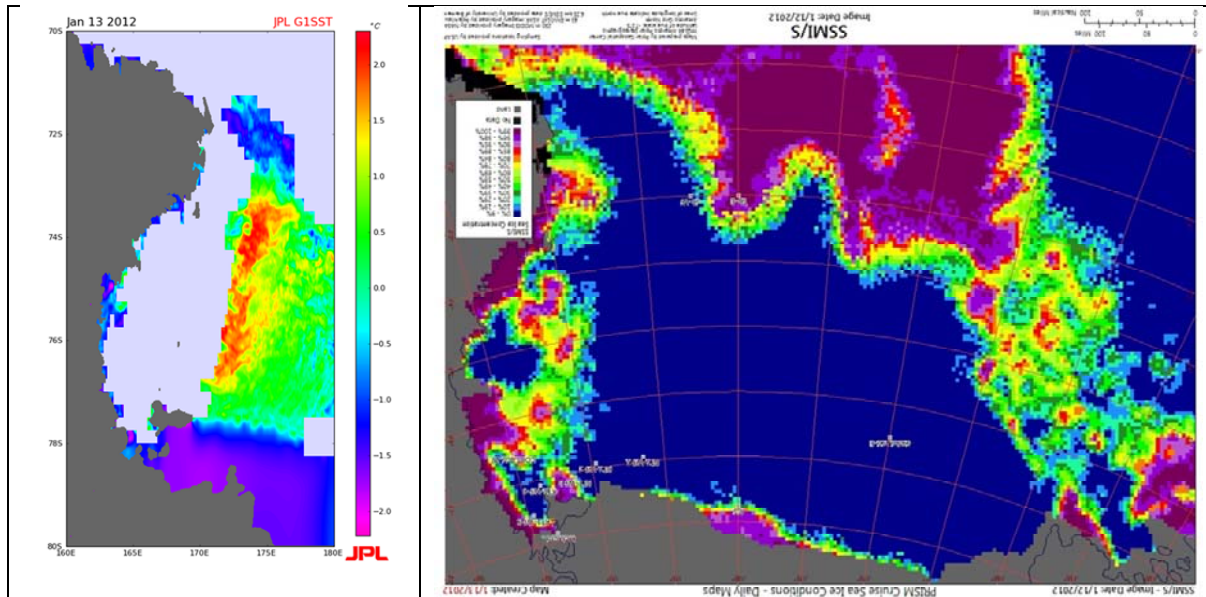
Figure WRS.34. Left: Satellite SST composite from January 13, 2012 Source: JPL). Right: SSSM/I ice coverage for the same date.
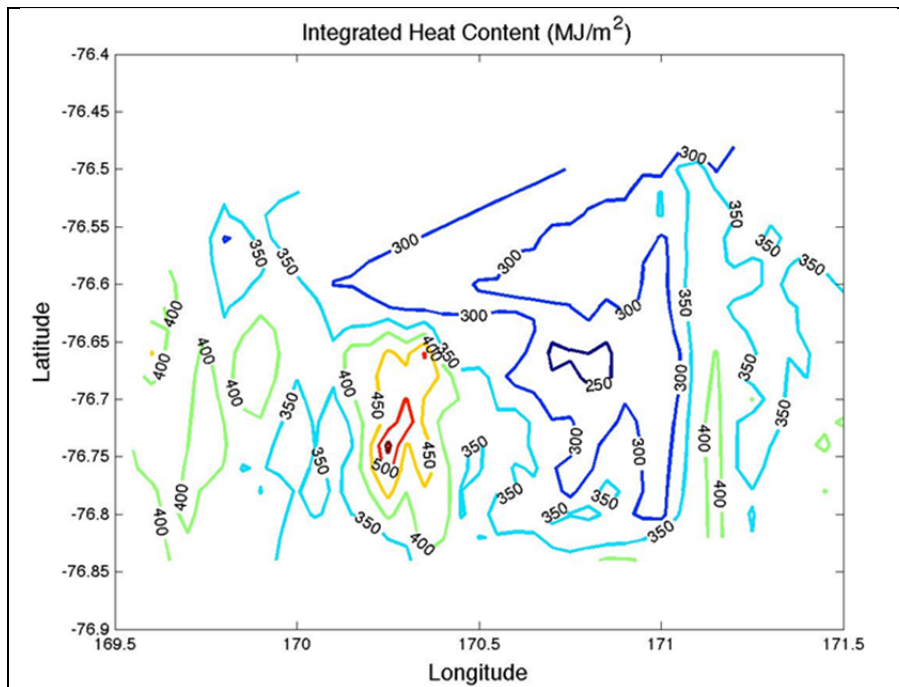
Figure WRS.35. Surface-100m integrated heat content content relative to in situ freezing. Largest heat content is slightly west of eddy center, ca. -76.74S / 170.25E. Source: John Klinck.
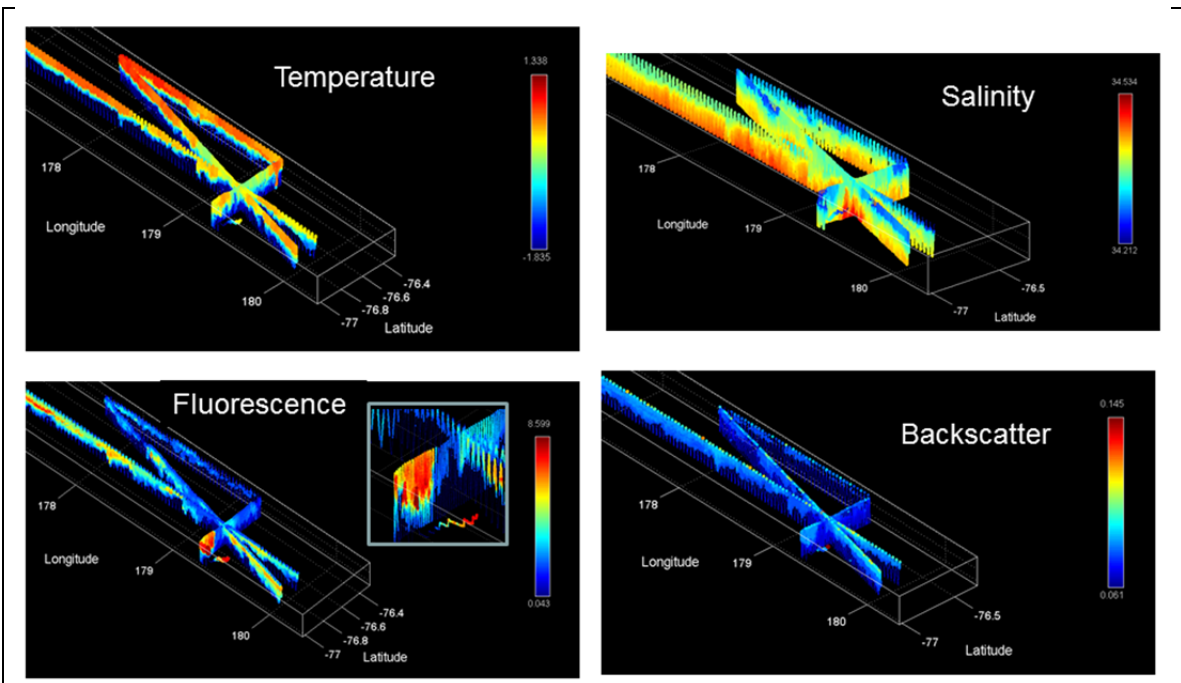
Figure RB.1. Ross Bank VPR survey (VPR9) January 20-21.
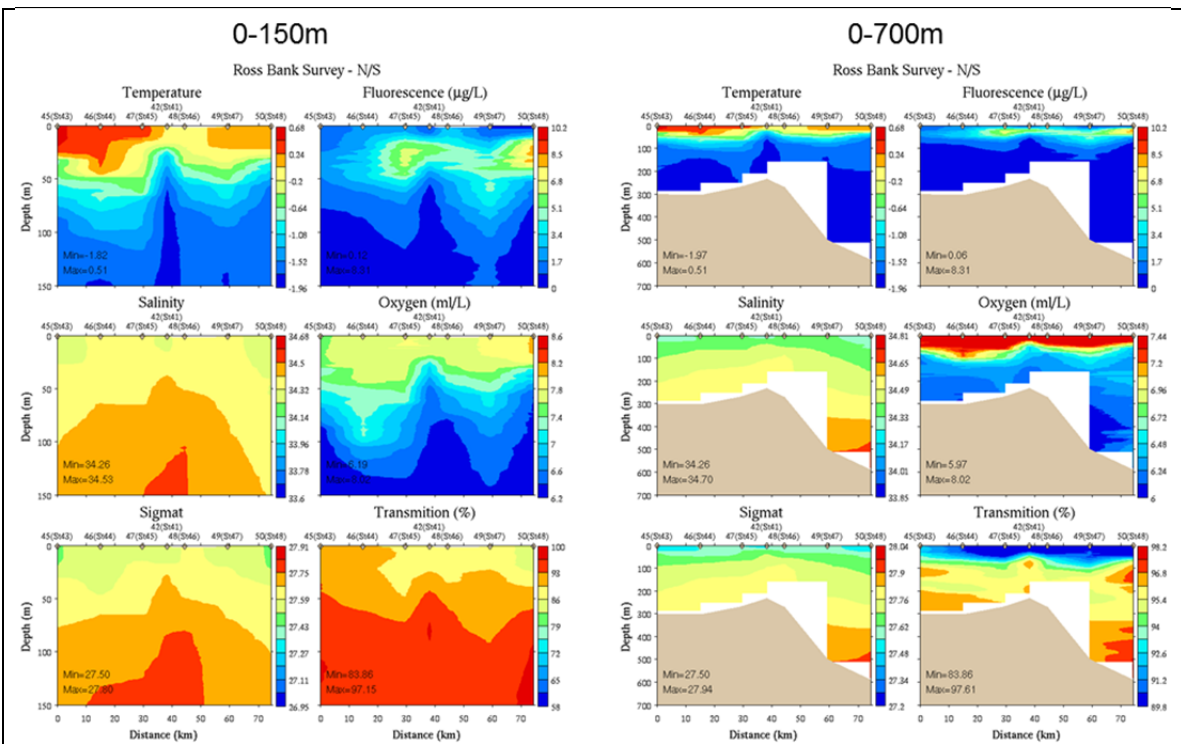
Figure RB.2. North-south CTD transect across Ross Bank.

Figure RB.3. North-south nutrient sections across Ross Bank.
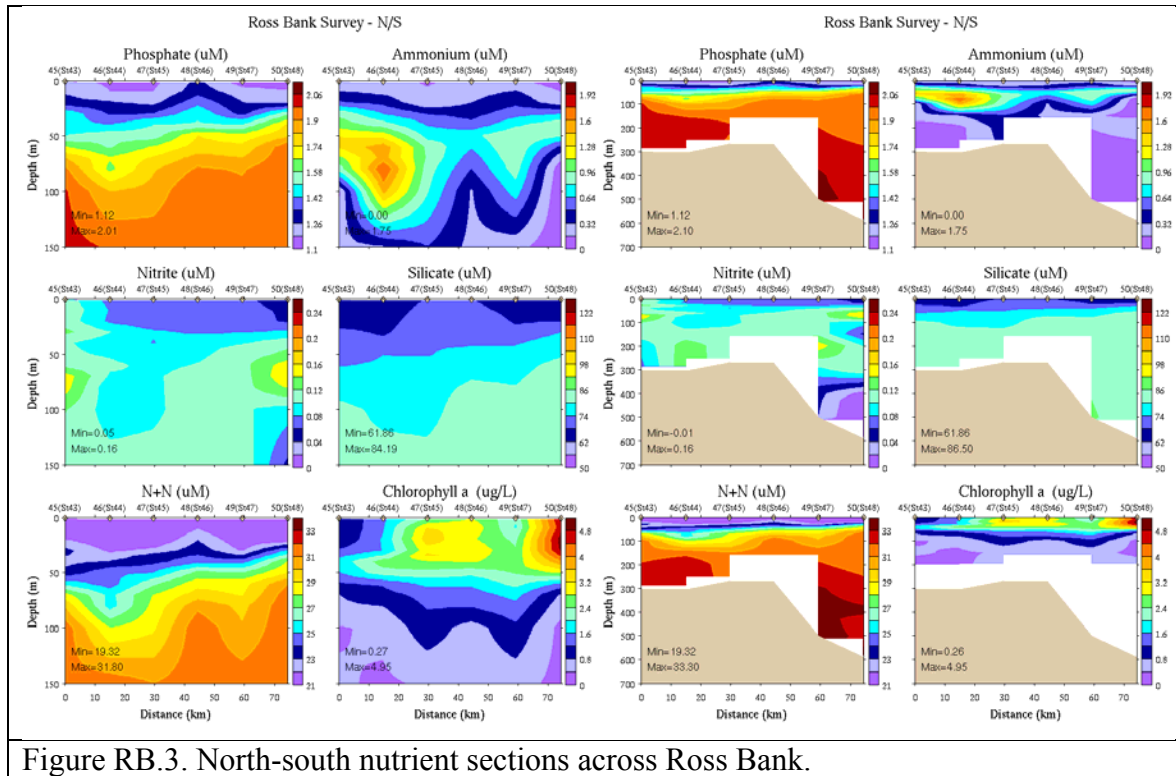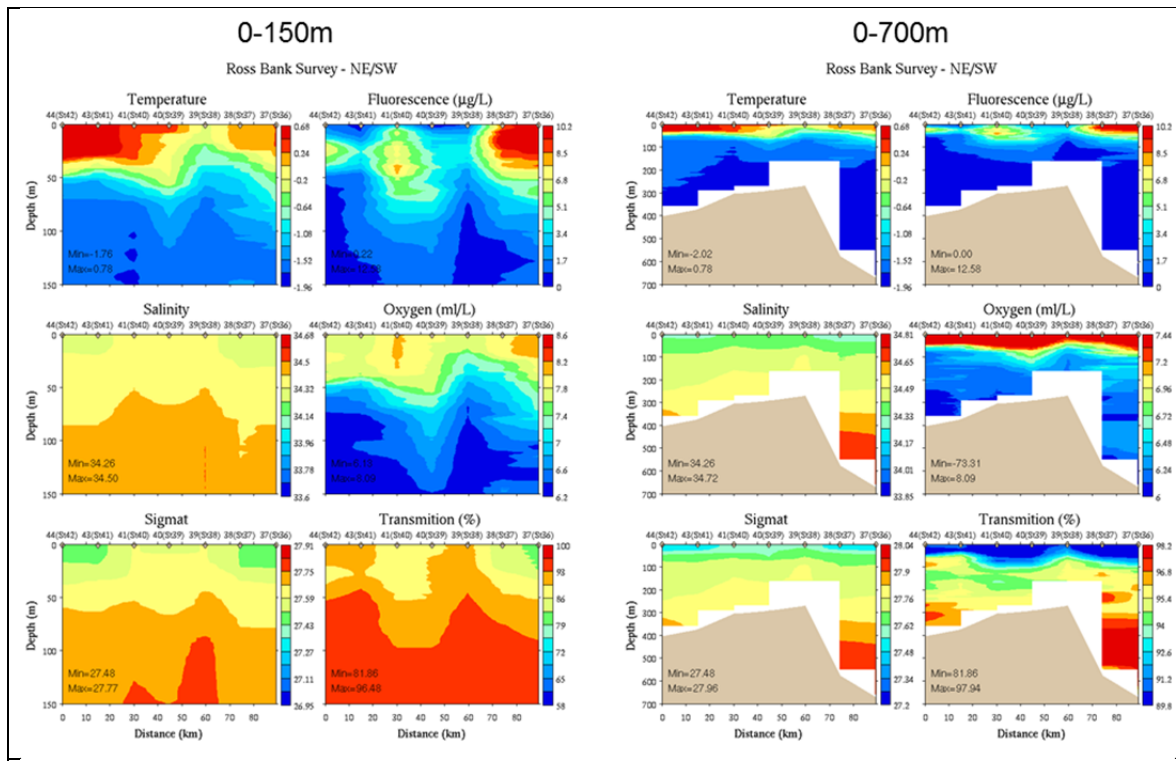
Figure RB.4. Northwest - southeast CTD transect across Ross Bank.
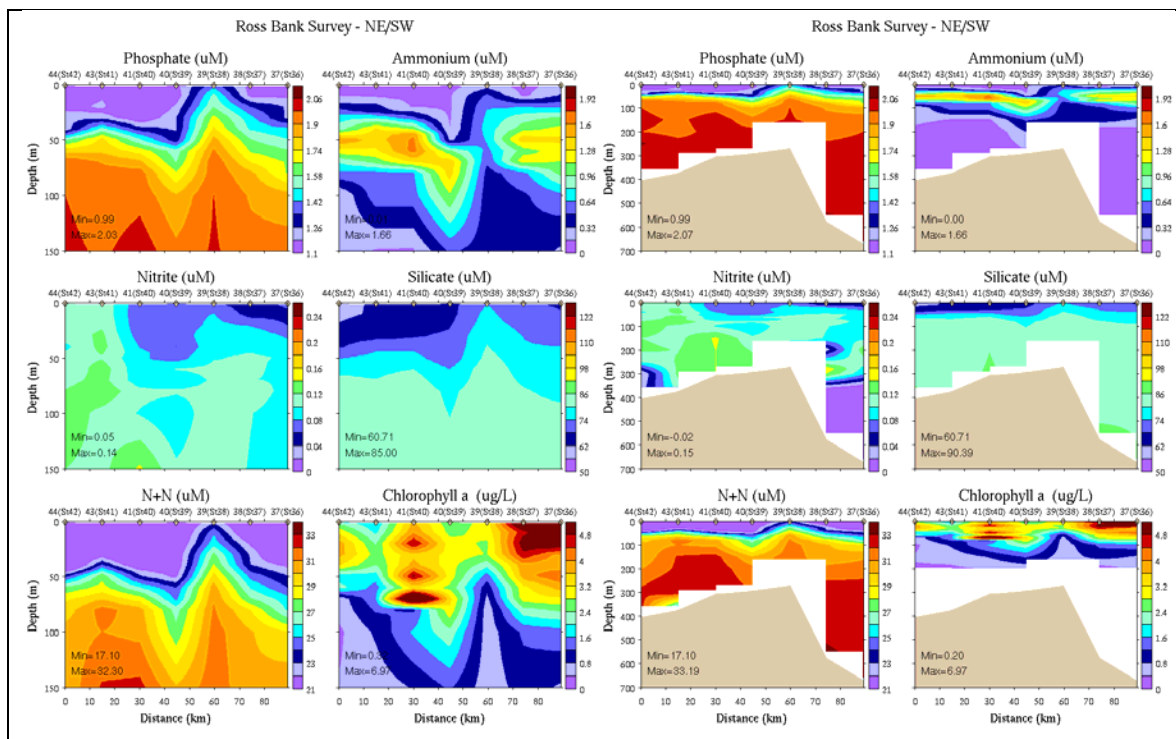
Figure RB.5. Northwest - southeast nutrient section across Ross Bank.
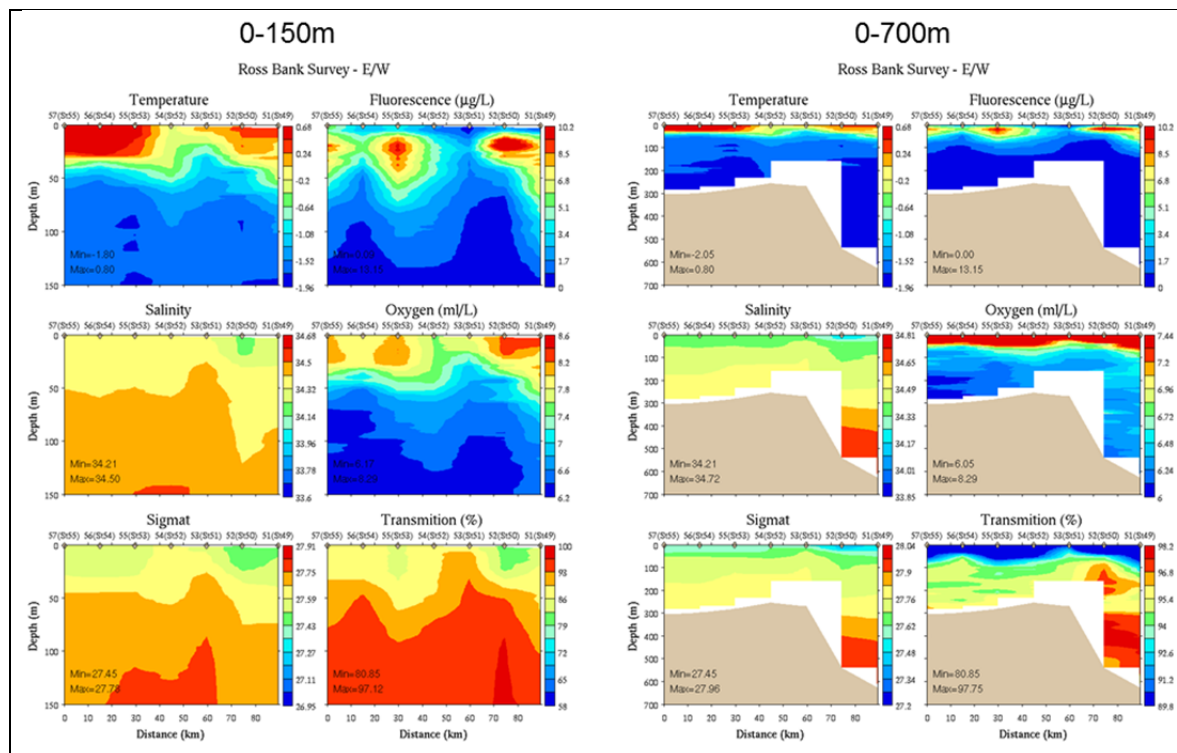
Figure RB.6. East-west CTD transect across Ross Bank.
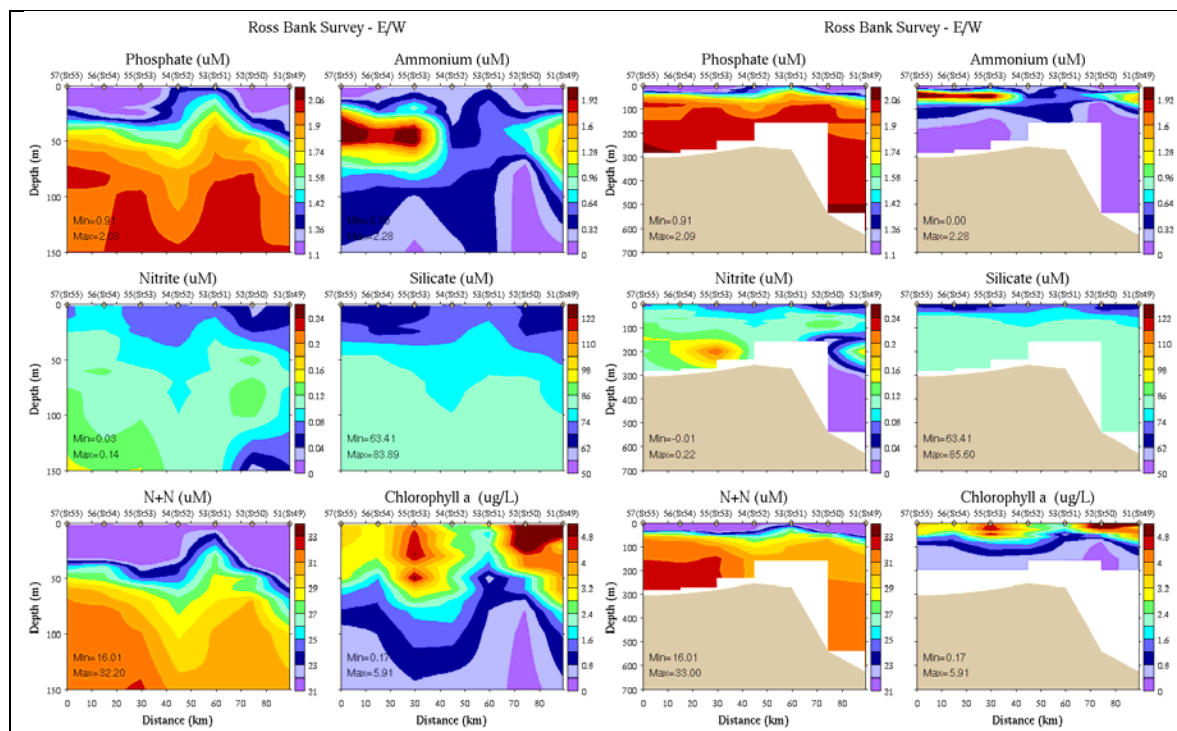
Figure RB.7. East-west nutrient section across Ross Bank.
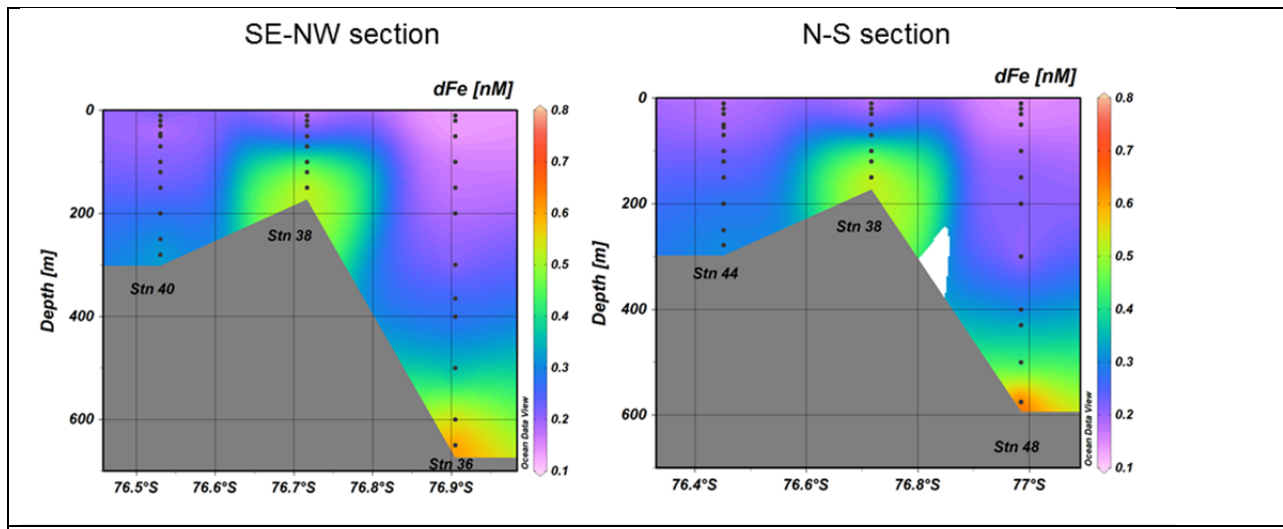
Figure RB.8. Dissolved iron concentration along the southeast-northwest and north-south sections across Ross Bank.
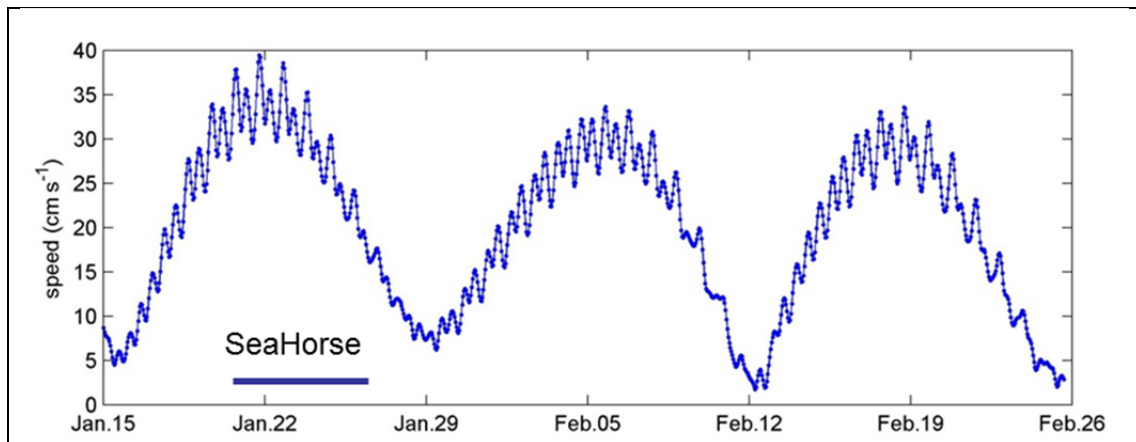
Figure RB.9. Ross Bank tidal velocity amplitude from the Erofeeva et al (2005) model. Time period of the SeaHorse deployment is indicated by a solid bar.
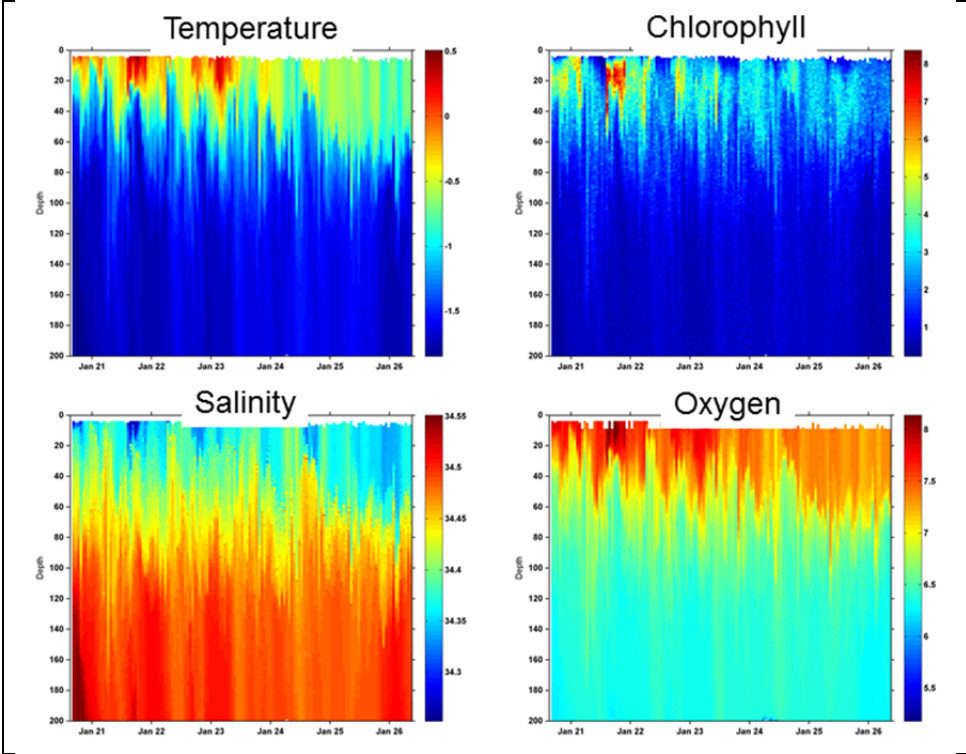
Figure RB.10. Time-series of temperature, salinity, fluorescence, and oxygen from the SeaHorse delployment on Ross Bank.
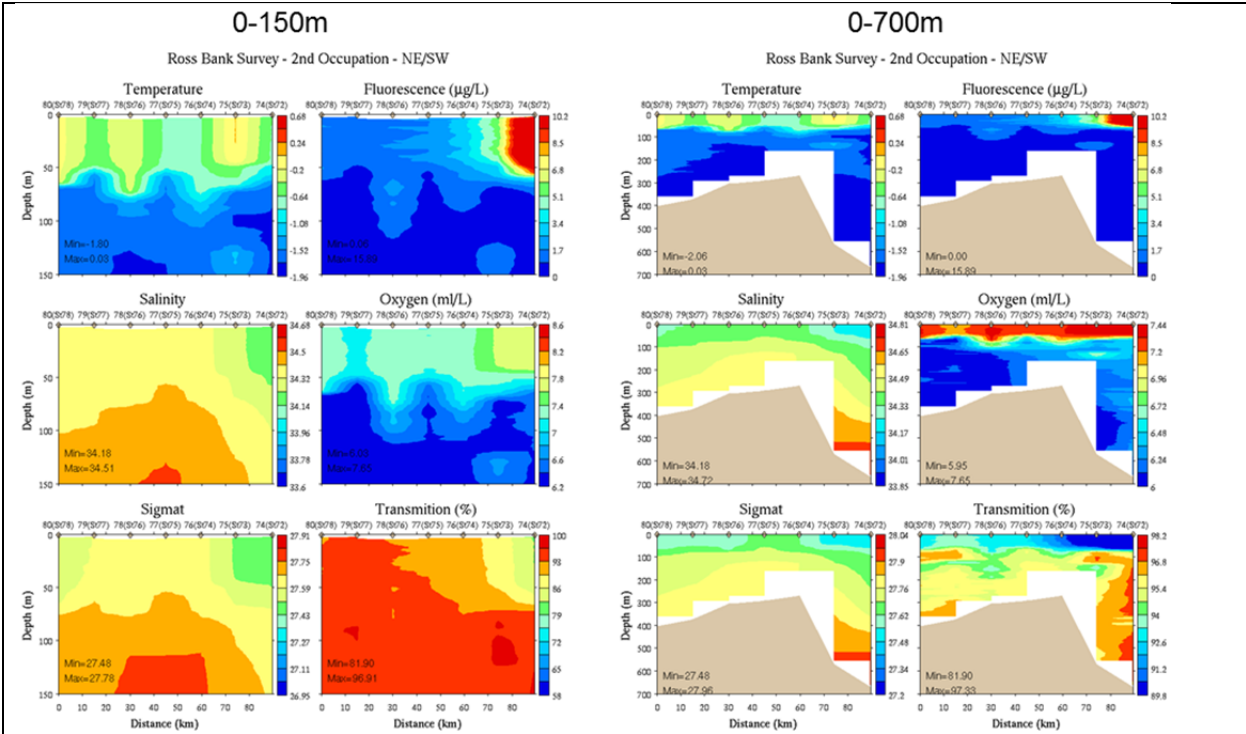
Figure RB.11. Second occupation of the northwest - southeast CTD transect across Ross Bank.
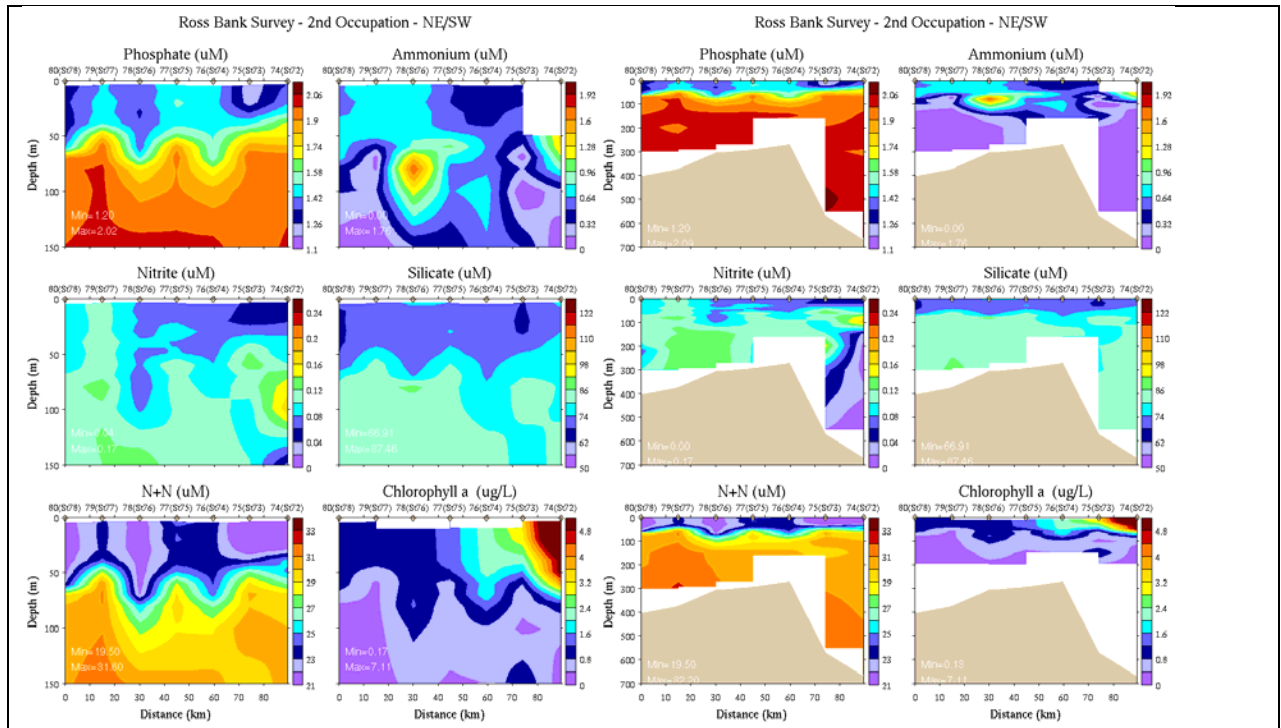
Figure RB.12. Second occupation of the northwest - southeast nutrient section across Ross Bank.
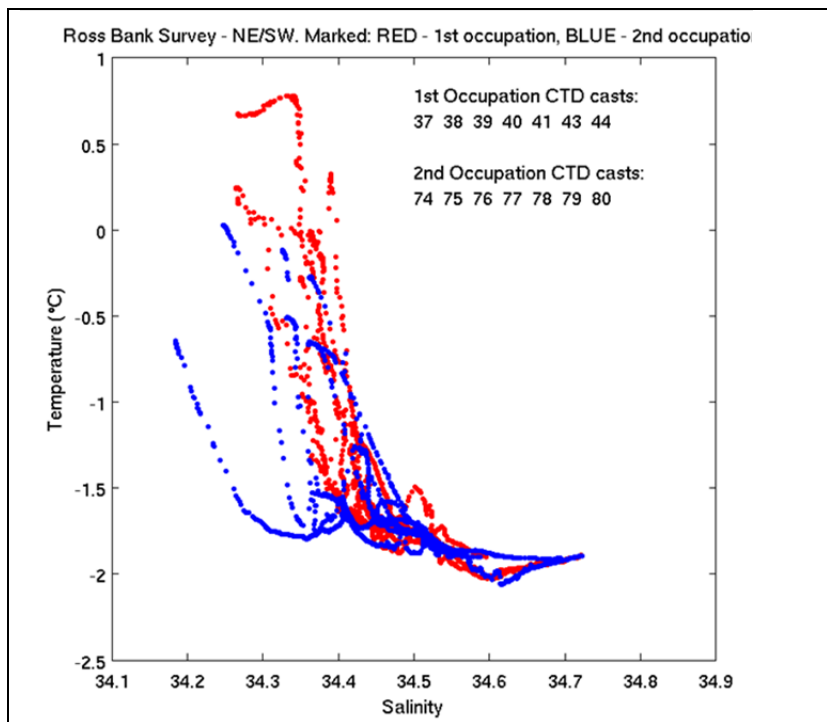
Figure RB.13. Temperature – salinity characteristics from CTD profiles along the northwest-southeast transect across Ross Bank: occupation 1 (red) and occupation 2 (blue).
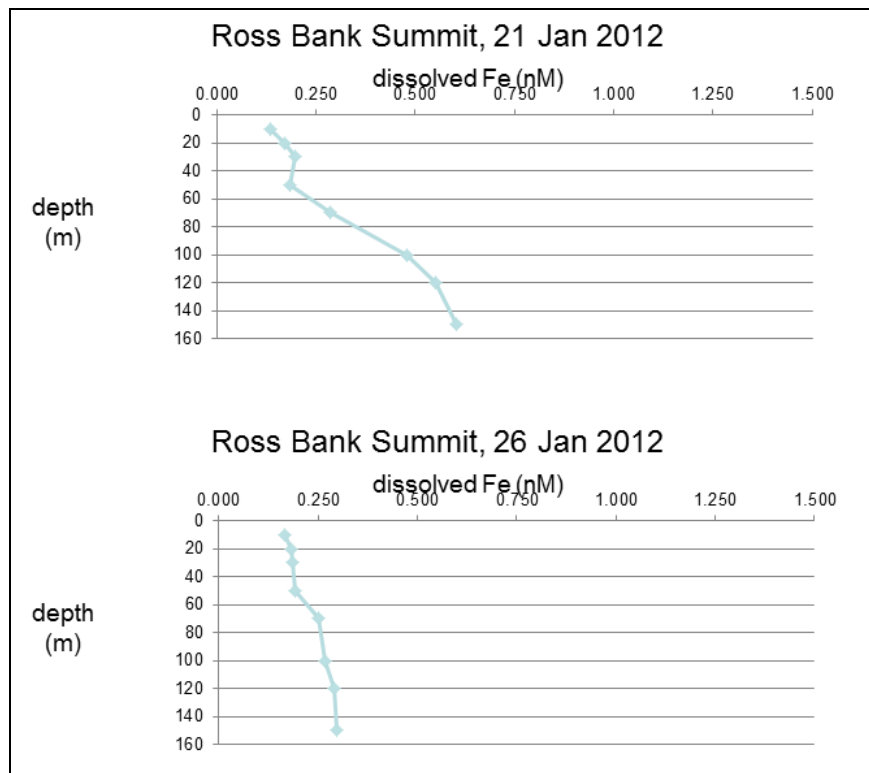
Figure RB.14. Dissolved iron on the first (top) and second (bottom) occupations of the crest of Ross Bank.
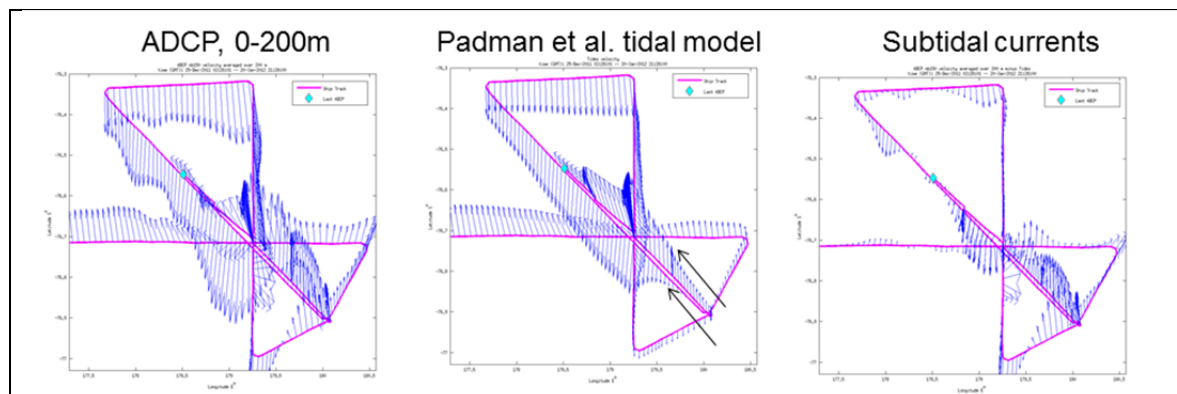
Figure RB.15. A portion of the Ross Bank VPR/ADCP survey.
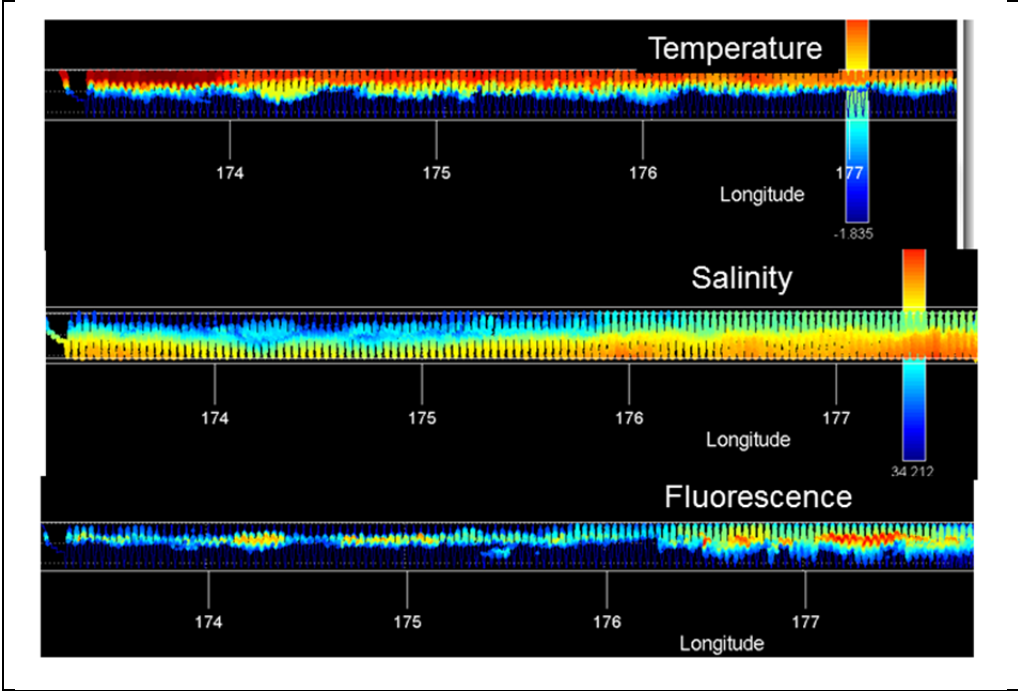
Figure RB.16. A portion of the VPR survey leading up to Ross Bank.
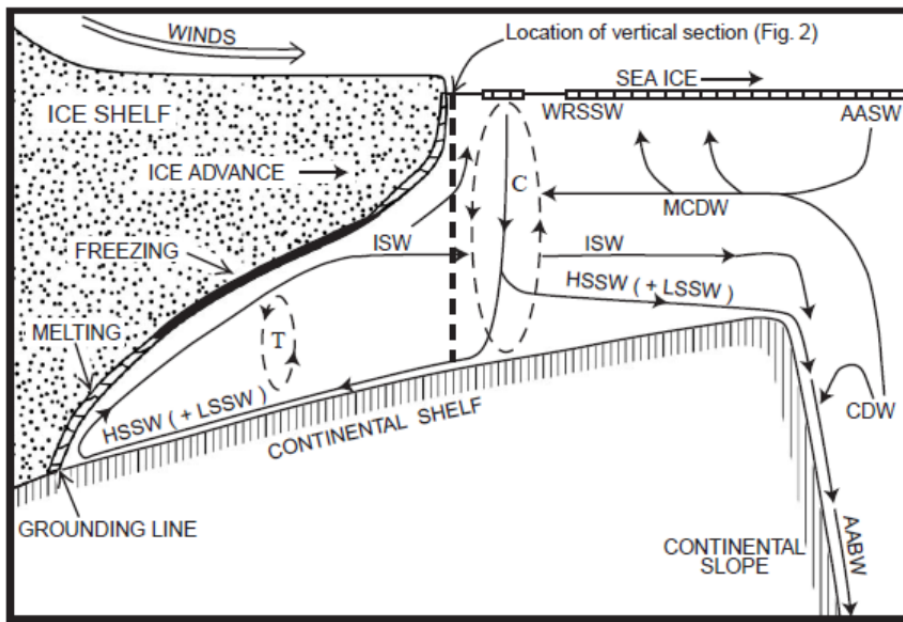
Figure RIS.1.   Schematic diagram of circulation and water mass formation in a vertical plane perpendicular to the Ross Ice Shelf front. AASW = Antarctic Surface Water, CDW = Circumpolar Deep Water, MCDW = Modified Circumpolar Deep Water, WRSSW = Western Ross Sea Surface Water, ISW = Ice Shelf Water, HSSW = High Salinity Shelf Water, LSSW = Low Salinity Shelf Water, AABW = Antarctic Bottom Water. Winter convective mixing is designated by the dashed circulation cell labeled C and tidal mixing is designated by the dashed circulation cell labeled T. From Smethie and Jacobs (2005).
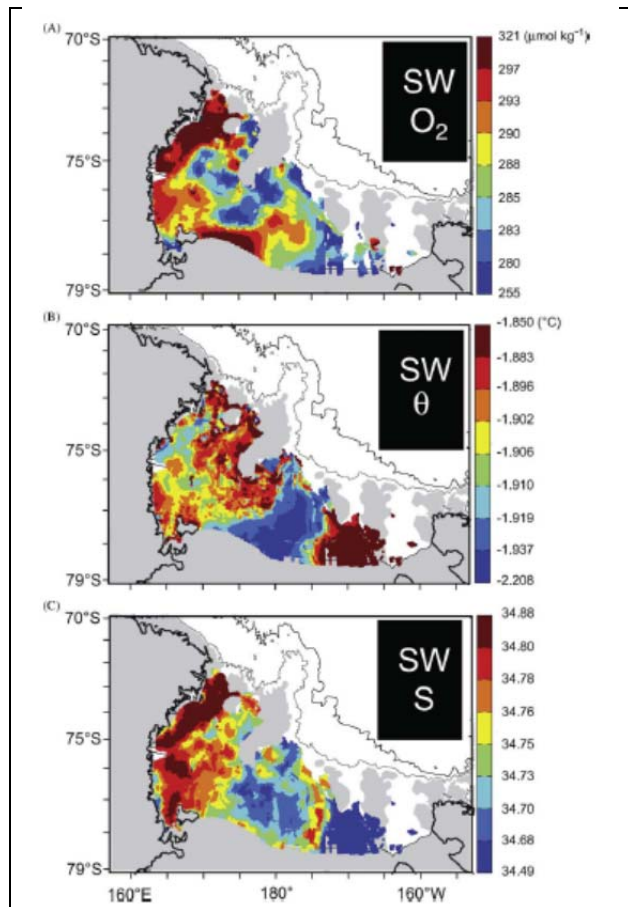
Figure RIS.2. Dissolved oxygen, potential temperature, and salinity of bottom shelf waters (SW), defined as neutral density $\gamma^n > 28.27$ kg m^{-3} and $\theta < -1.85°C$. Depths greater than 500m are shaded, and the thin lines show the 1000 and 3000m isobaths. From Orsi and Wiederwohl (2009).
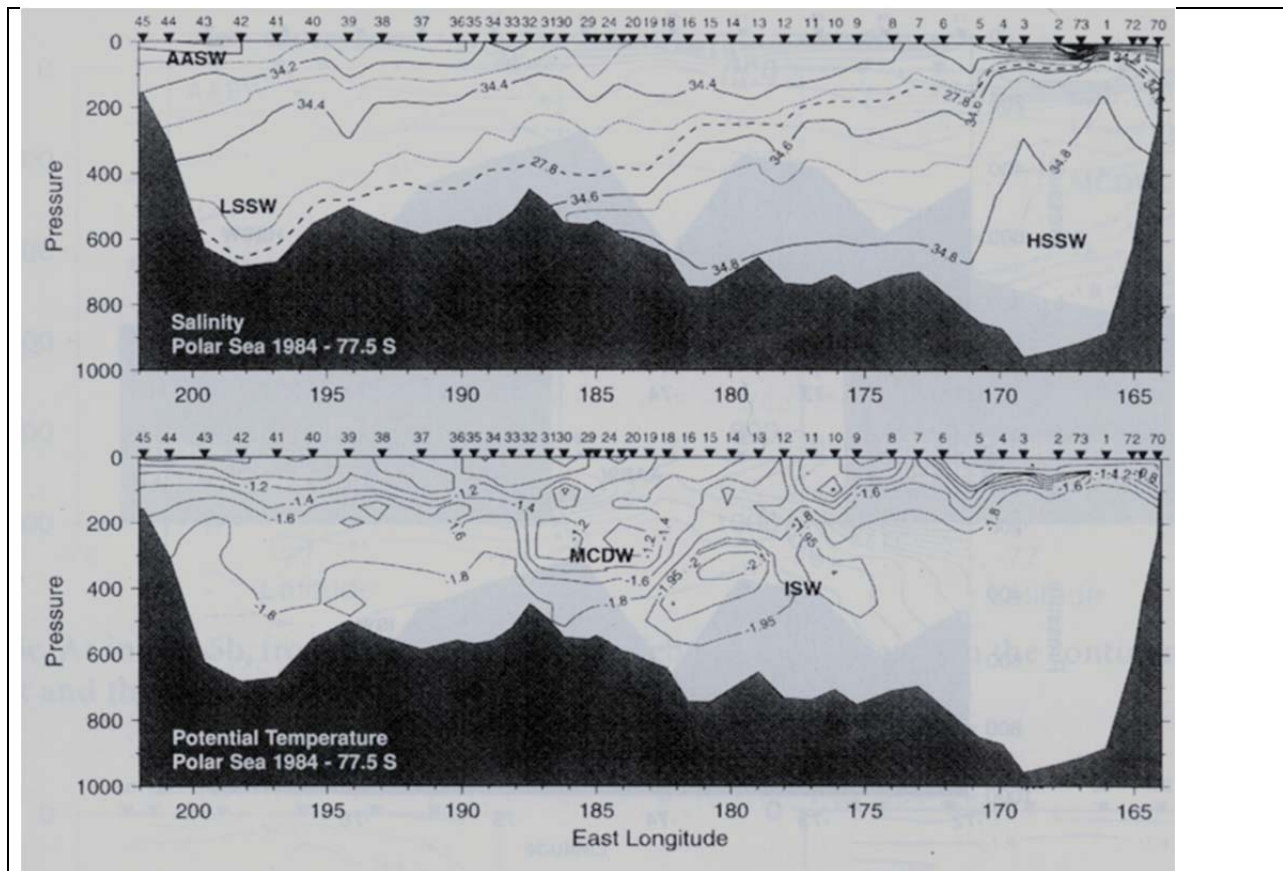
Figure RIS.3. Salinity and temperature in a quasi-zonal section along the Ross Ice Shelf and westward across McMurdo Sound occupied during February 1984. From Jacobs and Giulvi, 1999.
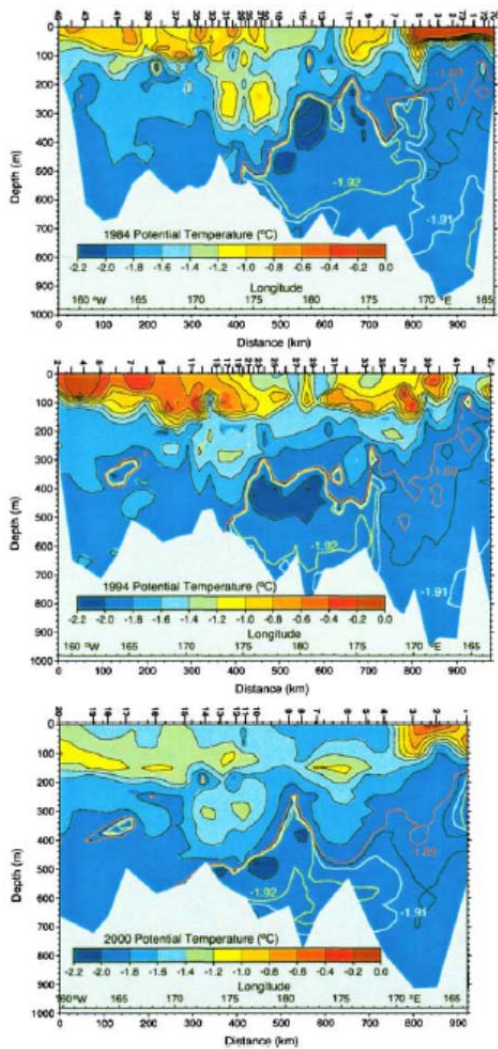
Figure RIS.4. Vertical sections of potential temperature along the front of the Ross Ice Shelf in 1984, 1994, and 2000. The views are southward, looking into the sub-ice cavity. The colored potential temperature isolines are as follows: red = -1.89°C; white=-1.91°C; yellow=-1.92°C. From Smethie and Jacobs, 2005.
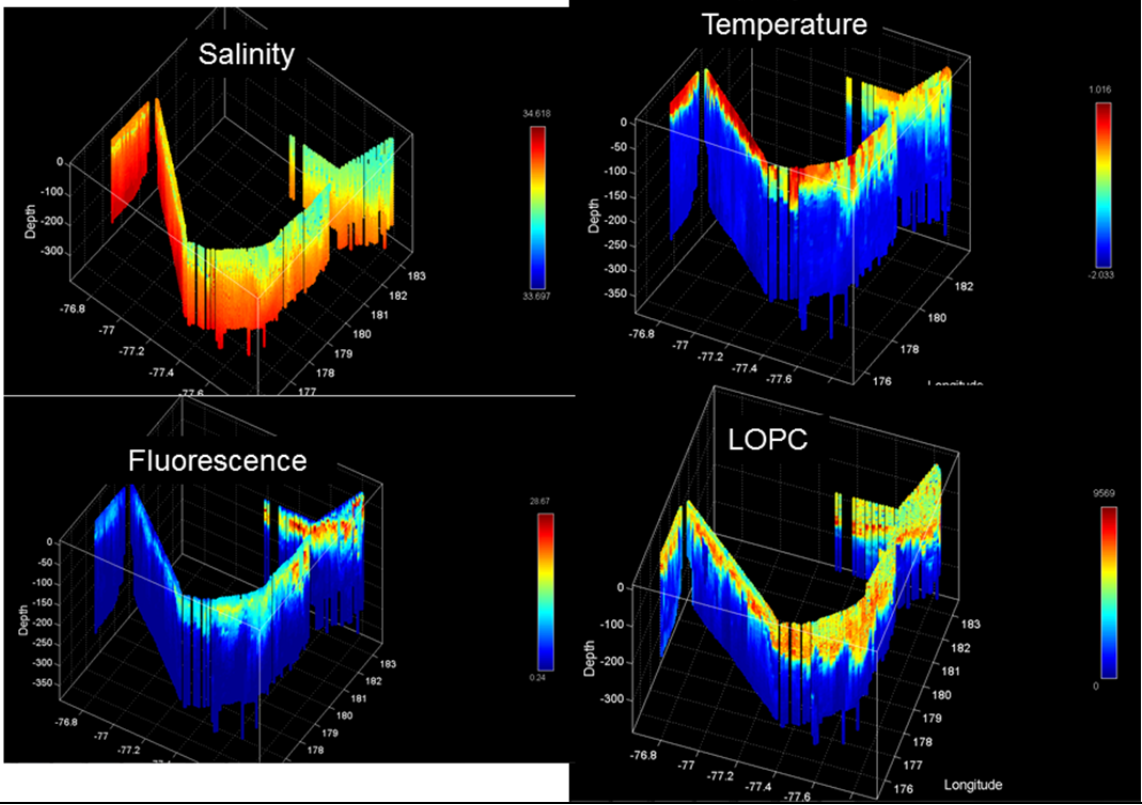
Figure RIS.5. Ross Ice Shelf MVP survey.
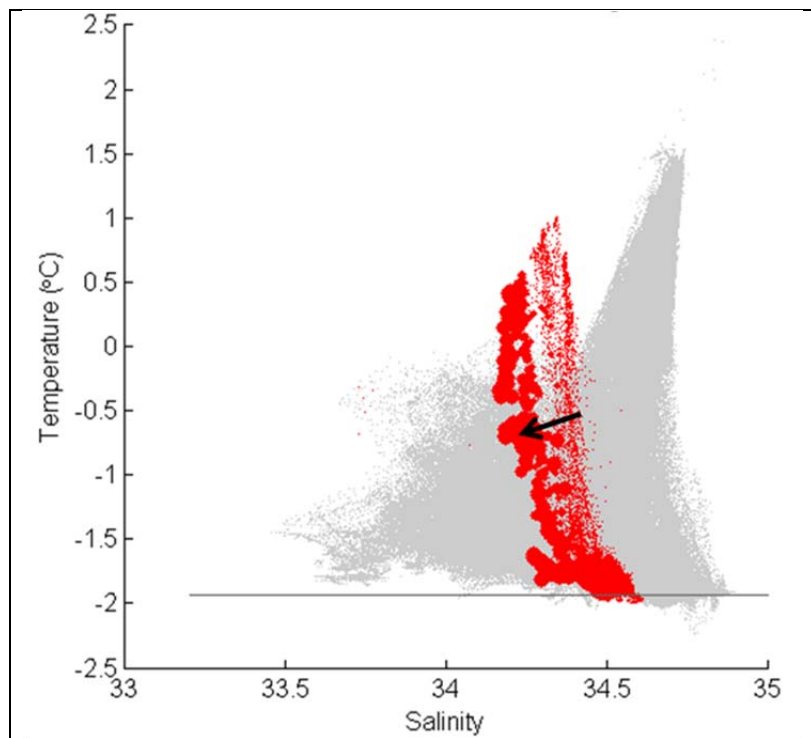
Figure RIS.6. Temperature – salinity characteristics from the MVP survey on approach to the Ross Ice Shelf.
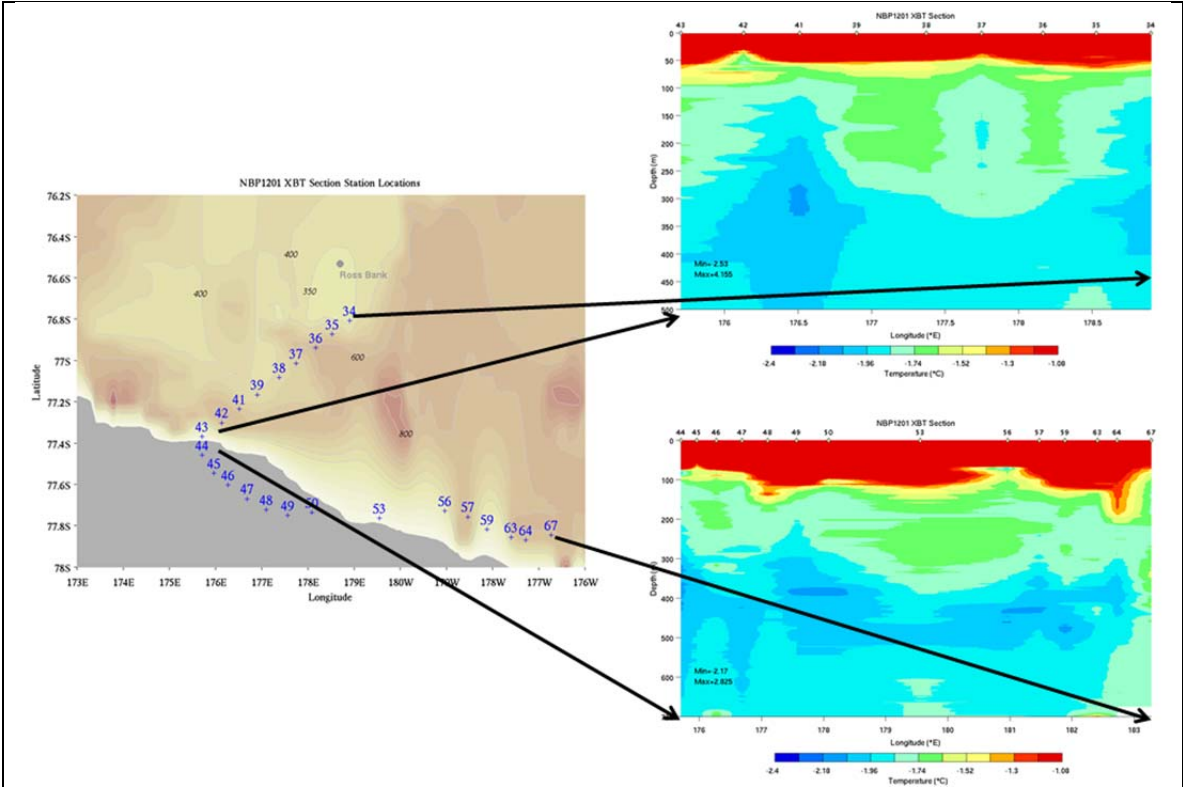
Figure RIS.7. Ross Ice Shelf XBT survey.
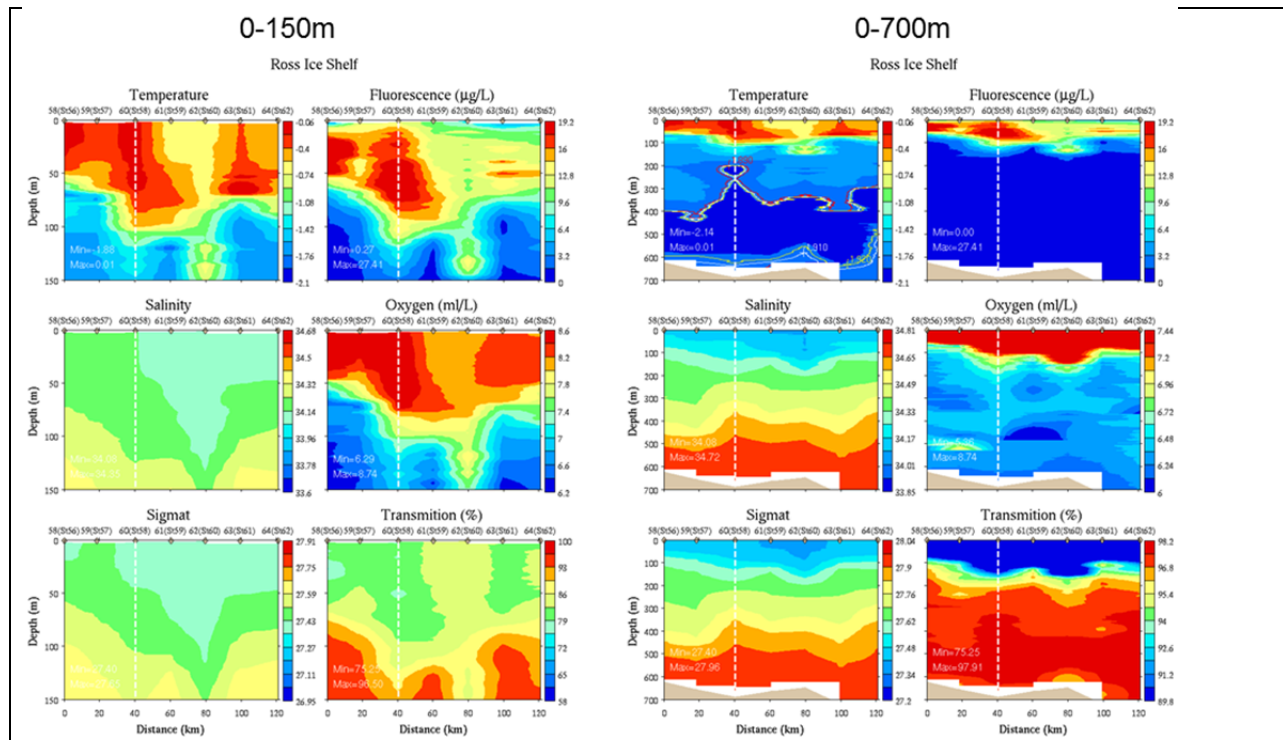
Figure RIS.8. Ross Ice Shelf CTD survey. North-south and east-west segments are divided by the dashed white line.
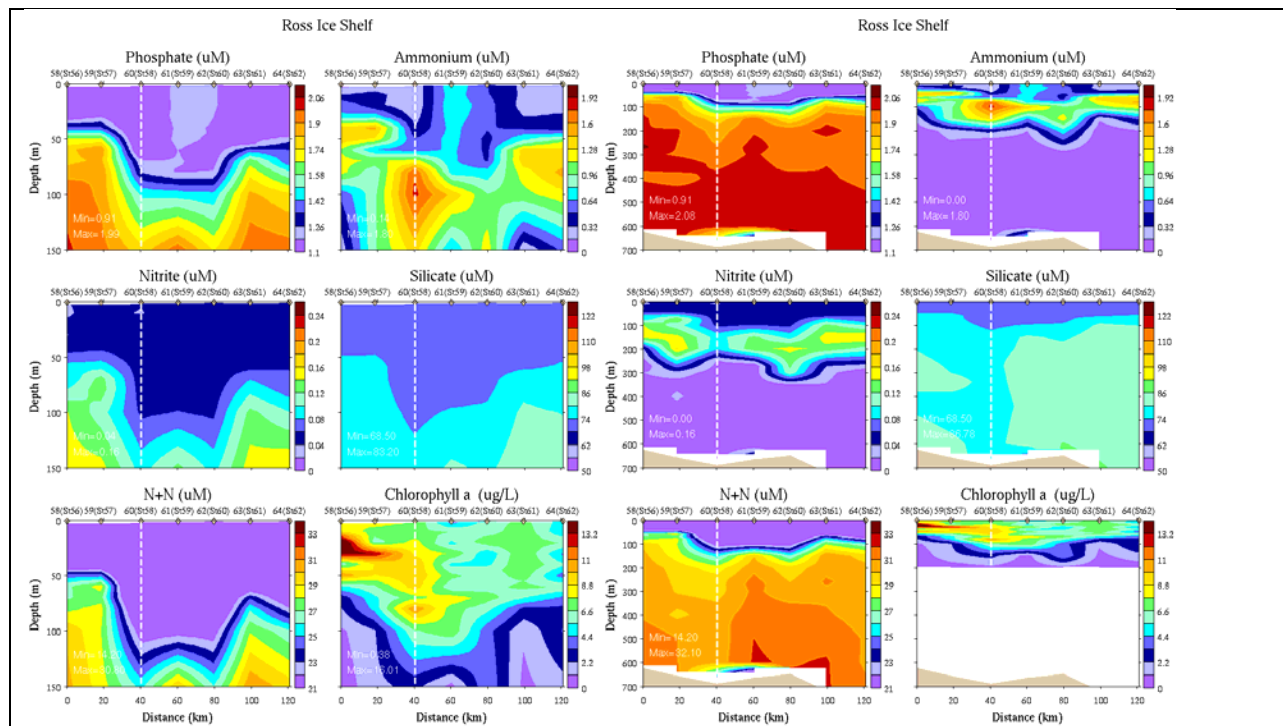
Figure RIS.9. Ross Ice Shelf survey. North-south and east-west segments are divided by the dashed white line.
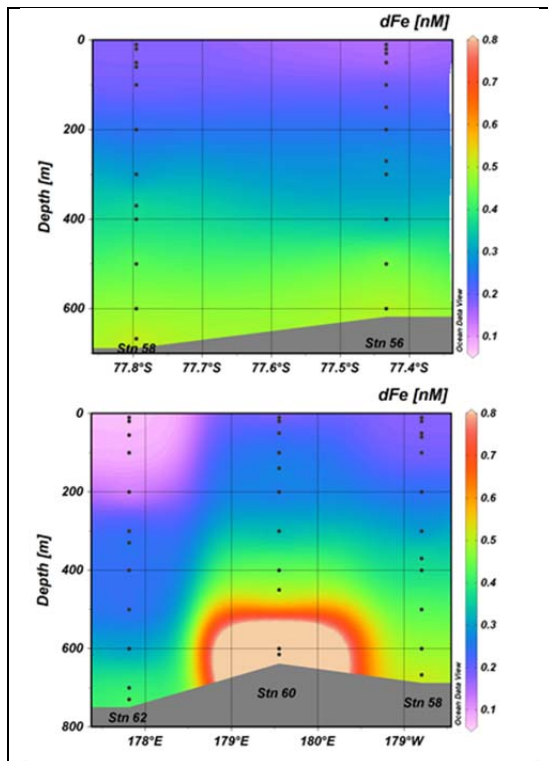
Figure RIS.10. Dissolved iron from the north-south (top) and east-west (bottom) sections of the Ross Ice Shelf survey.
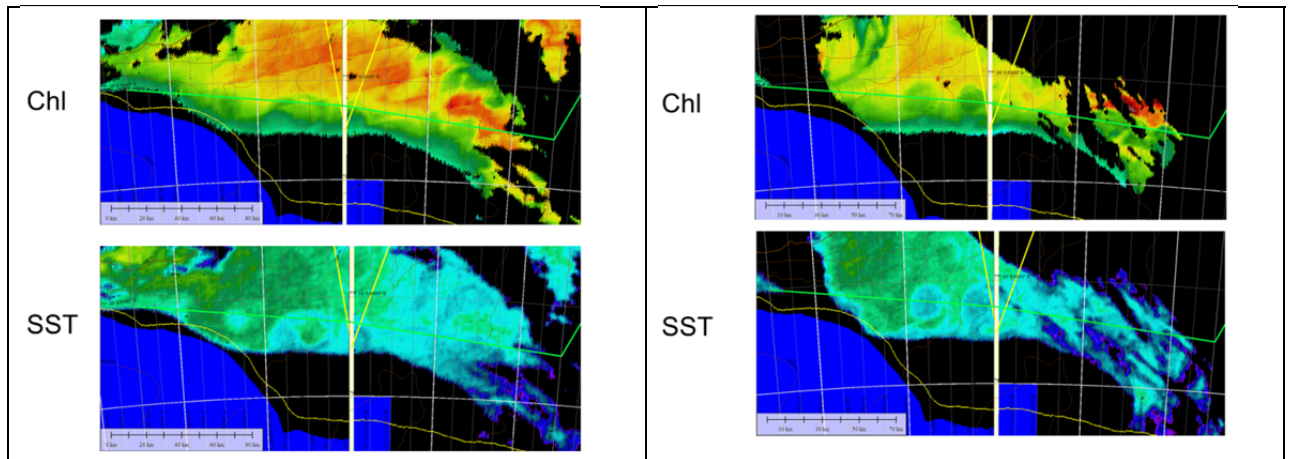
Figure RIS.11. MODIS Chl and SST images near the Ross Ice Shelf from January 22 (left) and January 25 (right).

Figure RIS.12. VPR / ADCP survey of Ross Ice Shelf Eddy, January 26 (VPR9).

Figure RIS.13. East-west section across the Ross Ice Shelf eddy.
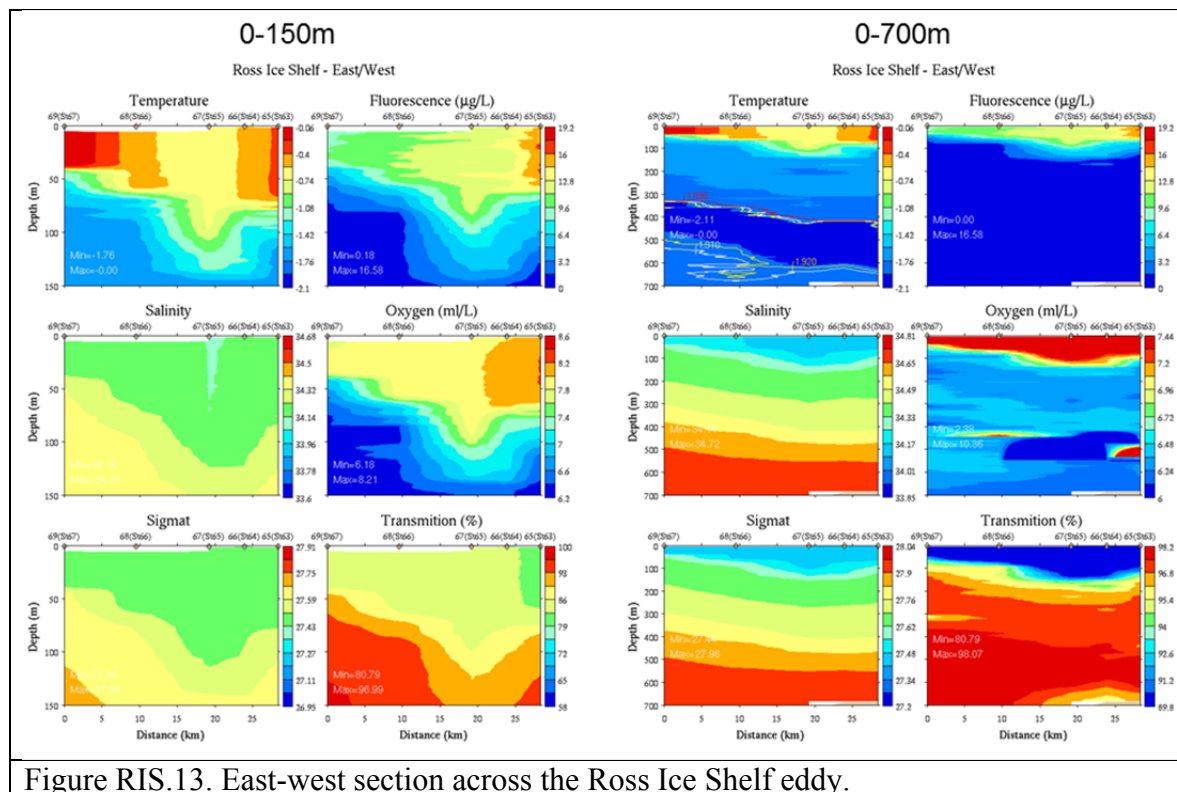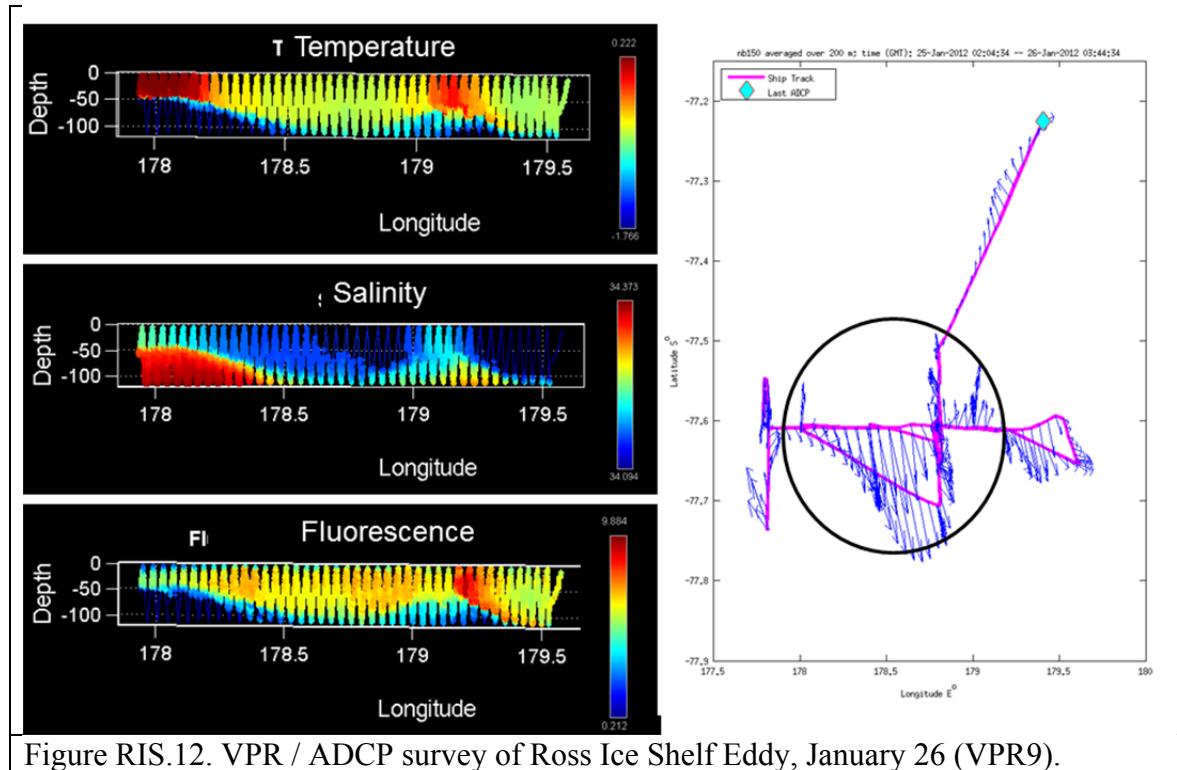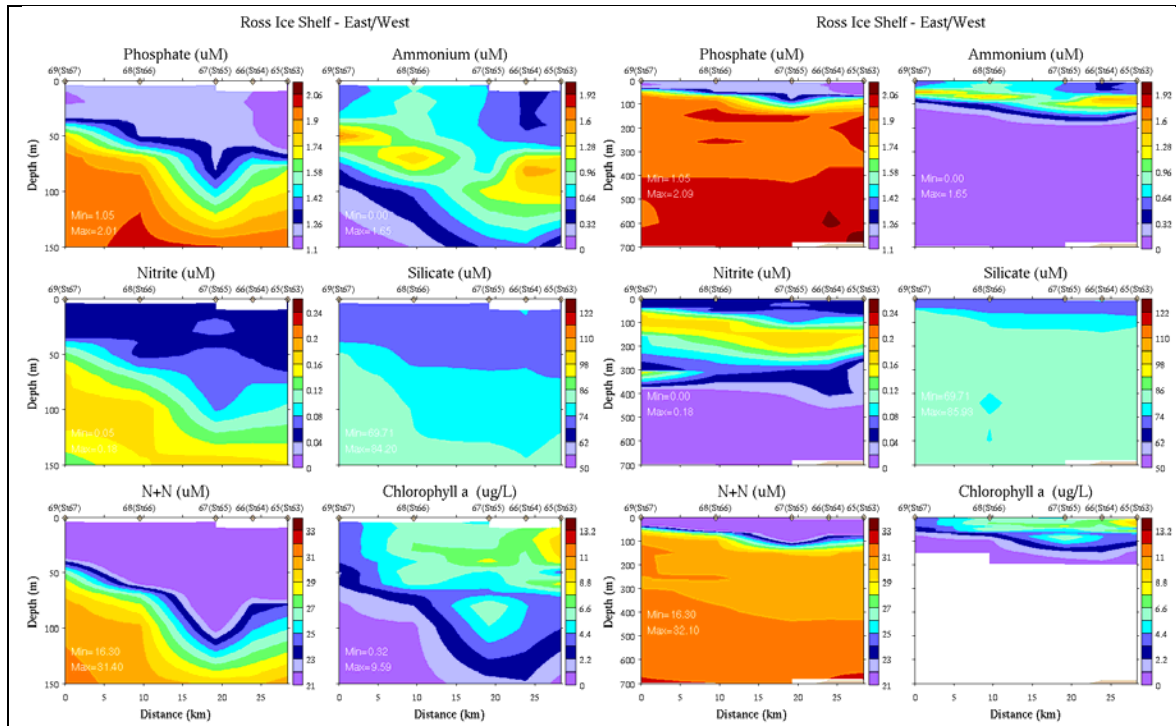
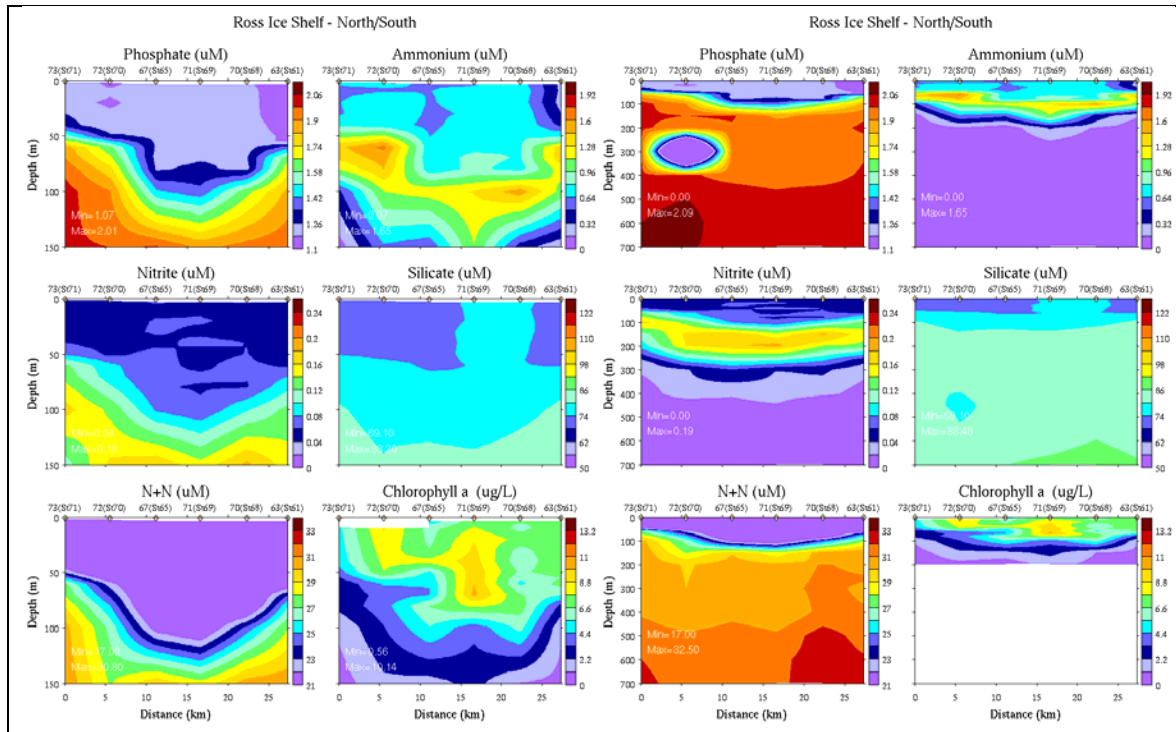Figure RIS.14. East-west section across the Ross Ice Shelf eddy.
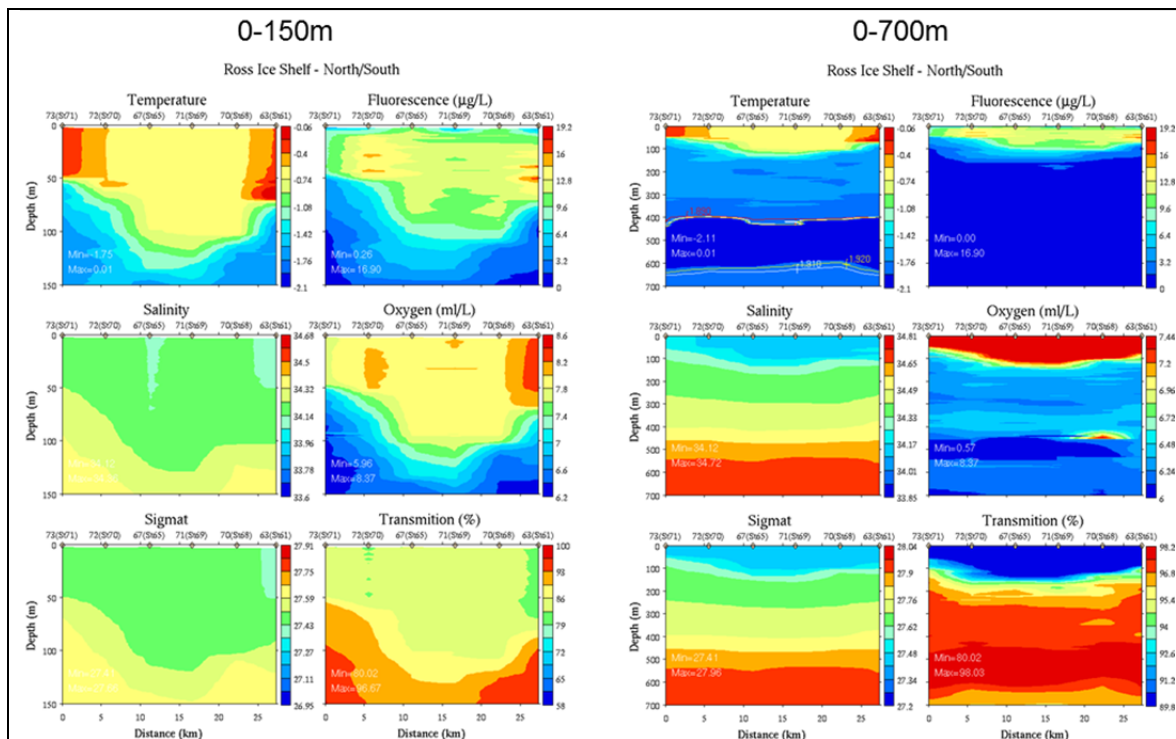
Figure RIS.15. North-south section across the Ross Ice Shelf eddy.

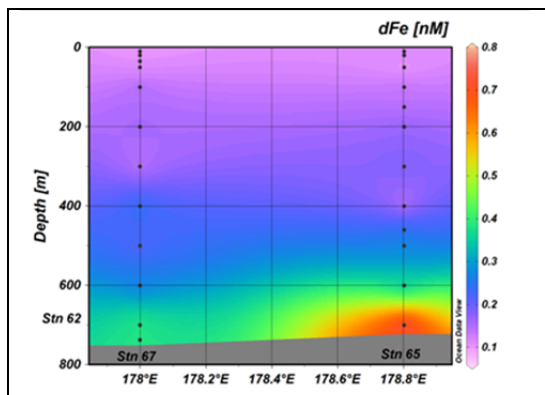Figure RIS.16. North-south section across the Ross Ice Shelf eddy.

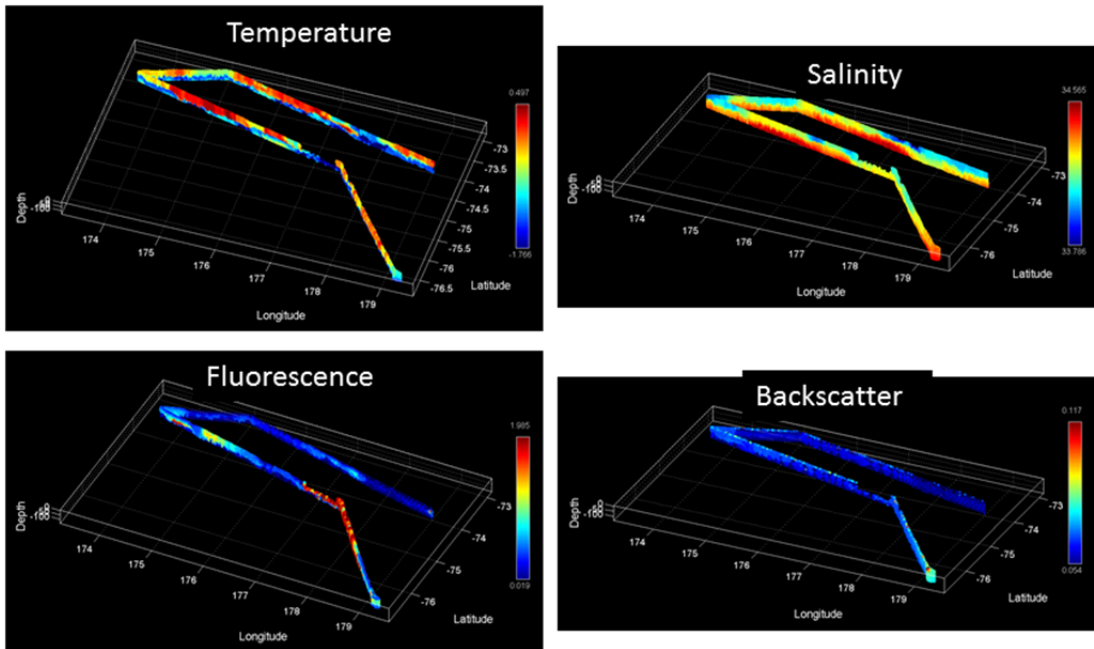Figure RIS.17. Dissolved iron from the east-west section of the Ross Ice Shelf eddy.

Figure JT.1. VPR survey from Ross Bank to Pennell Bank, across Joides Trough to Mawson Bank, northeastward along the crest of Mawson Bank, and then back across Joides Trough to Pennell Bank (VPR10).
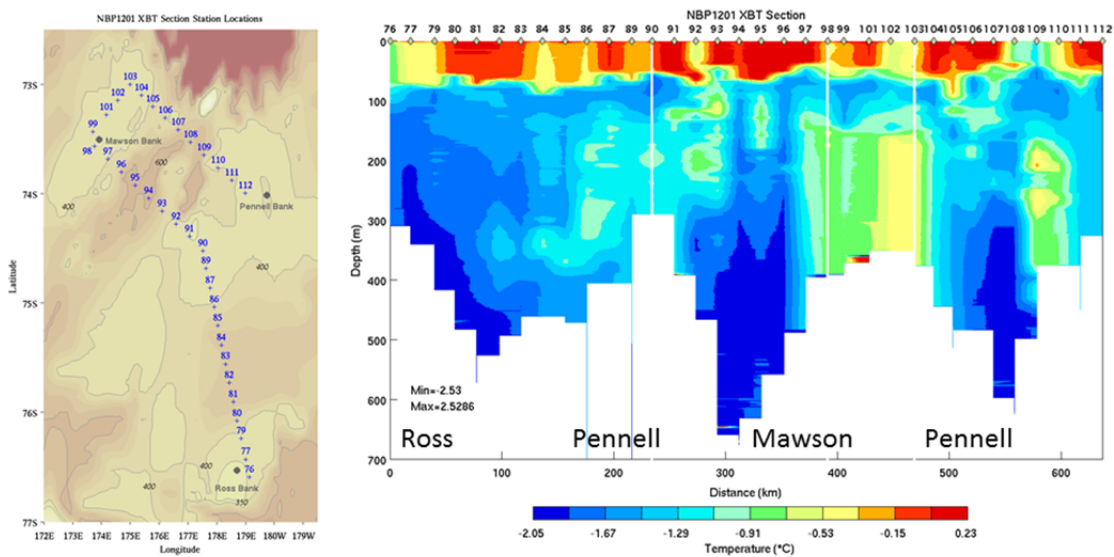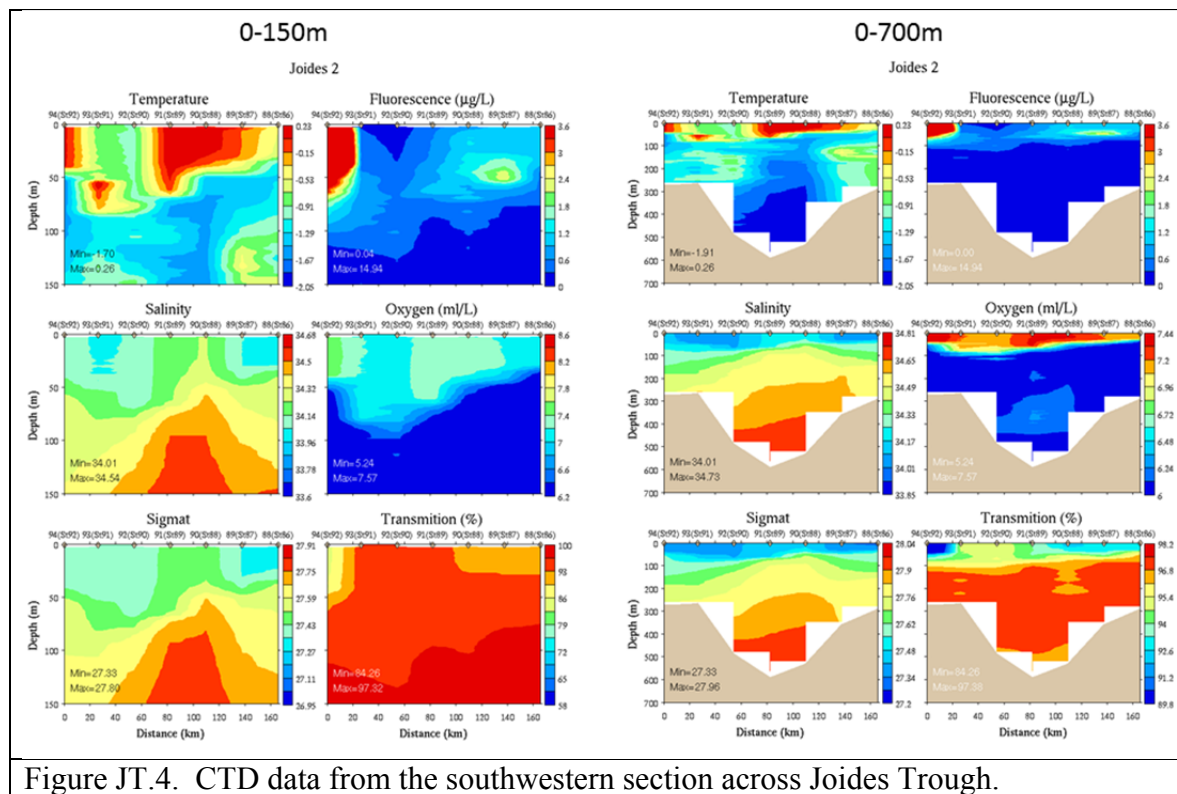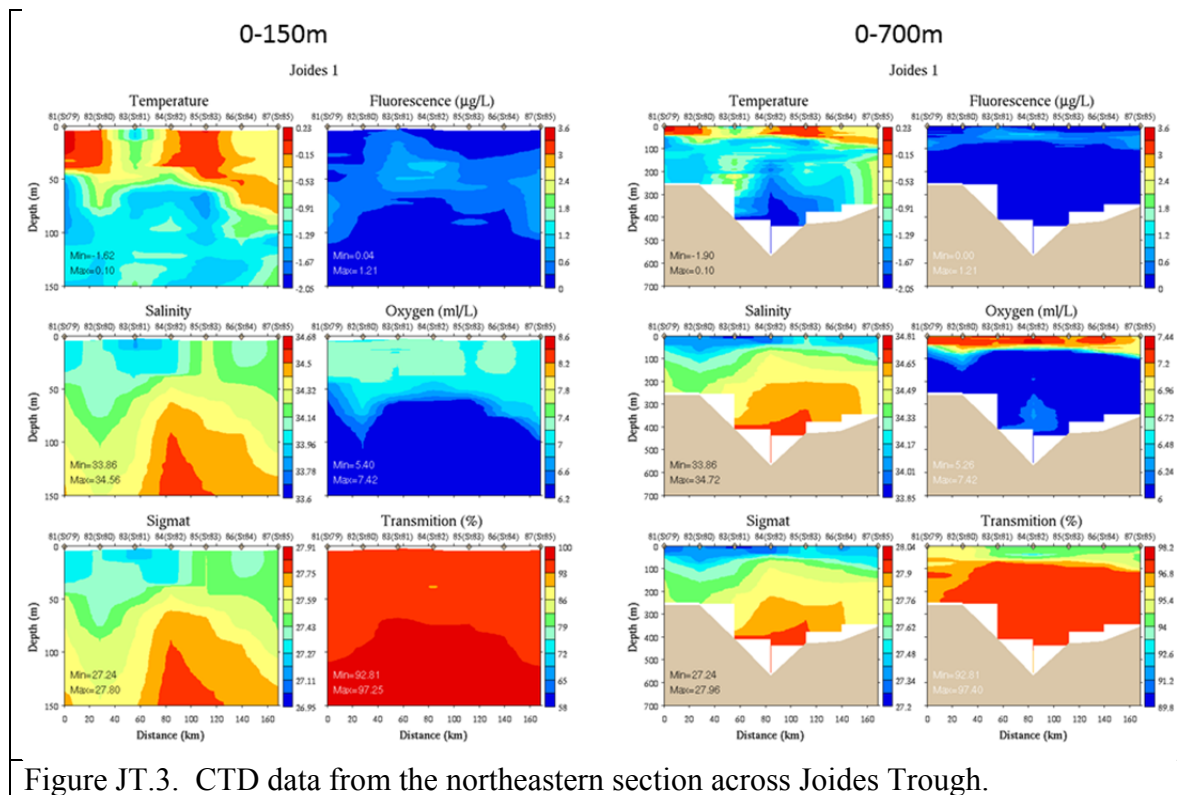

Figure JT.2. XBT survey from Ross Bank to Pennell Bank, across Joides Trough to Mawson Bank, northeastward along the crest of Mawson Bank, and then back across Joides Trough to Pennell Bank. Turning points in the XBT section are indicated as white vertical lines.

Figure JT.3. CTD data from the northeastern section across Joides Trough.

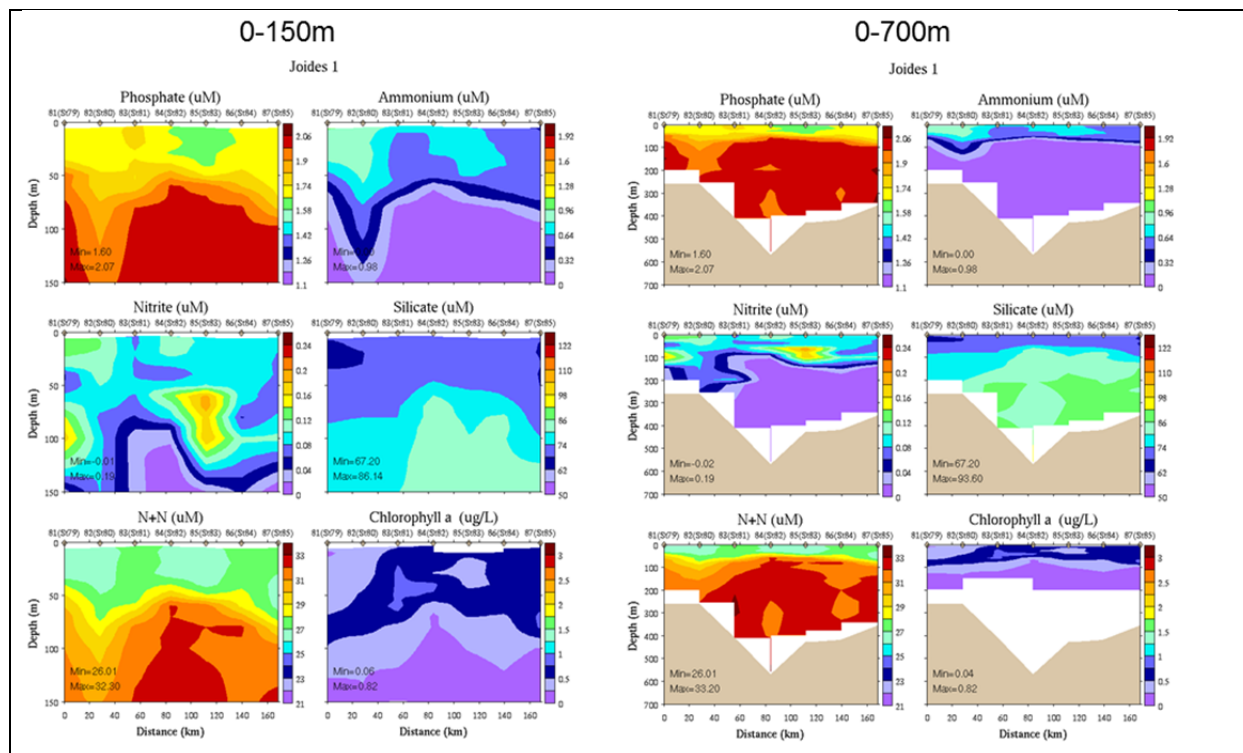Figure JT.4. CTD data from the southwestern section across Joides Trough.

Figure JT.5. Nutrient and chlorophyll data from the northeastern section across Joides Trough.
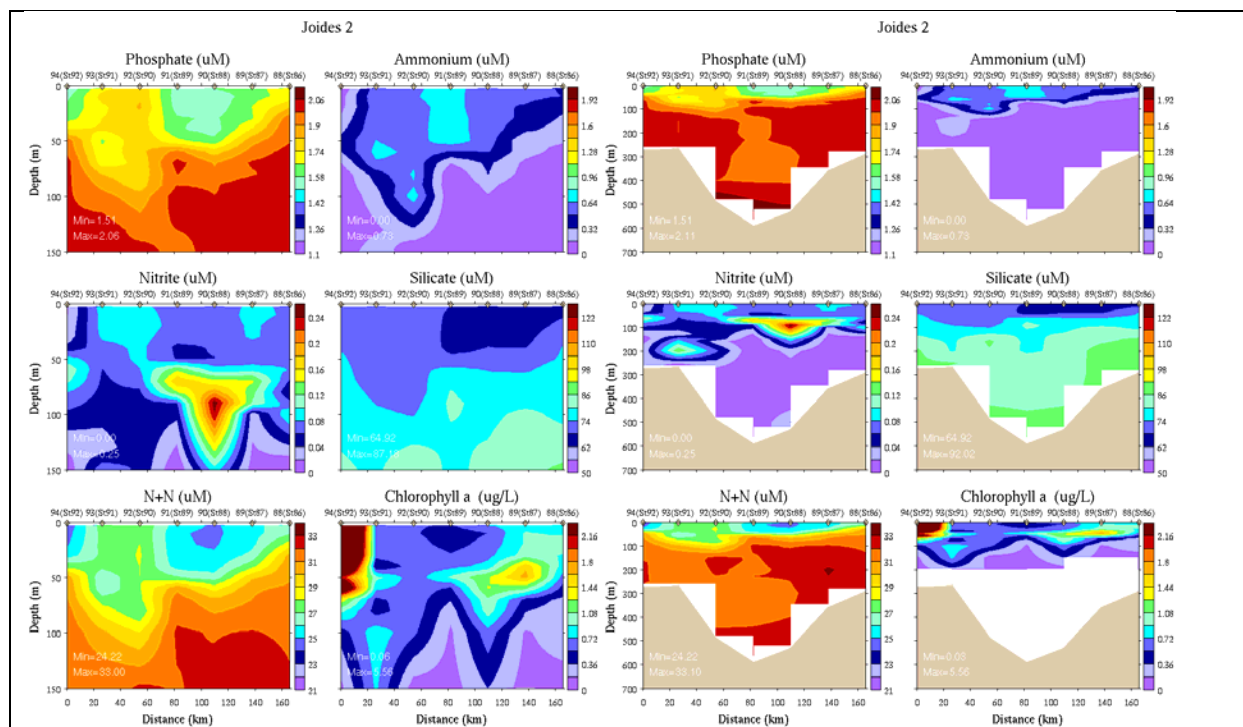

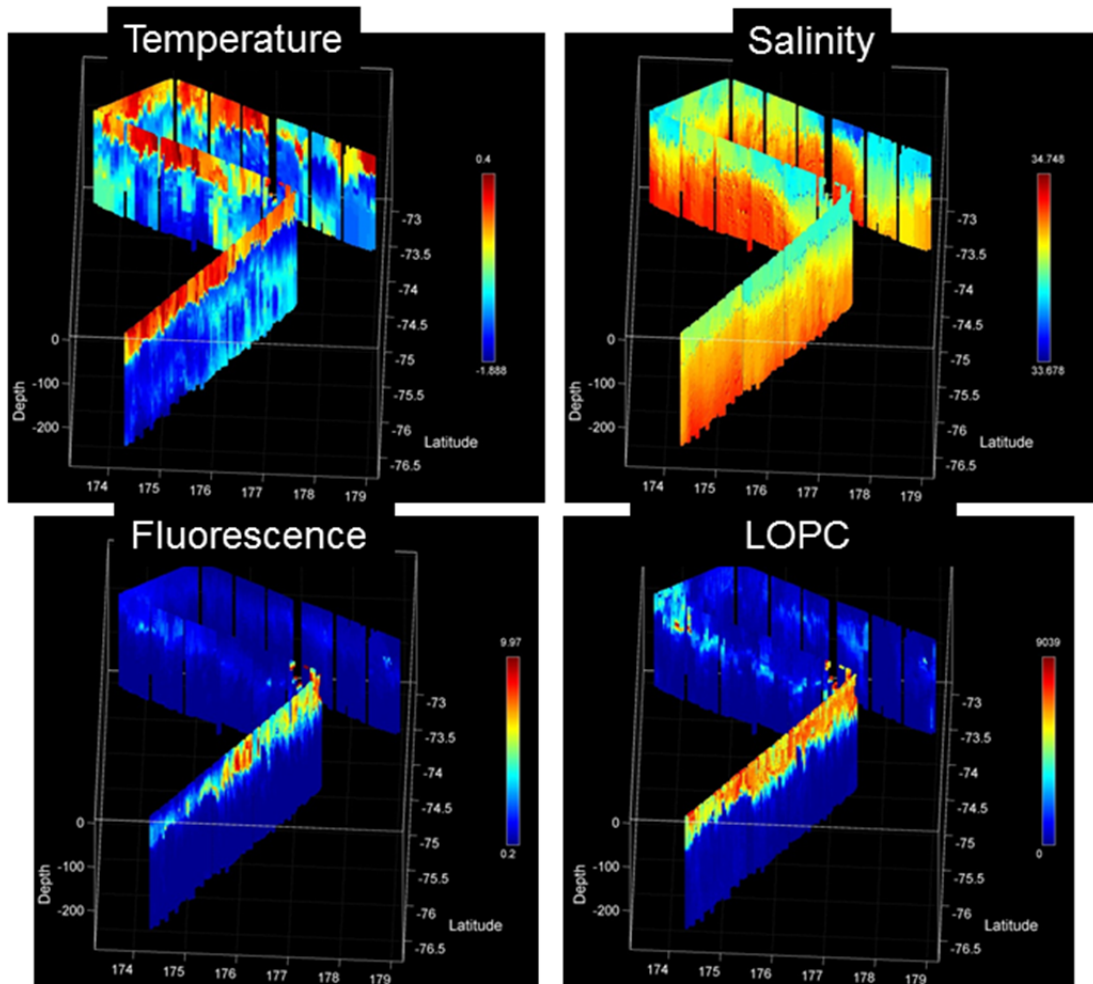Figure JT.6. Nutrient and chlorophyll data from the southwestern section across Joides Trough.

Figure JT.7. MVP survey along the two Joides Trough transects and then southward to the western Ross Sea.
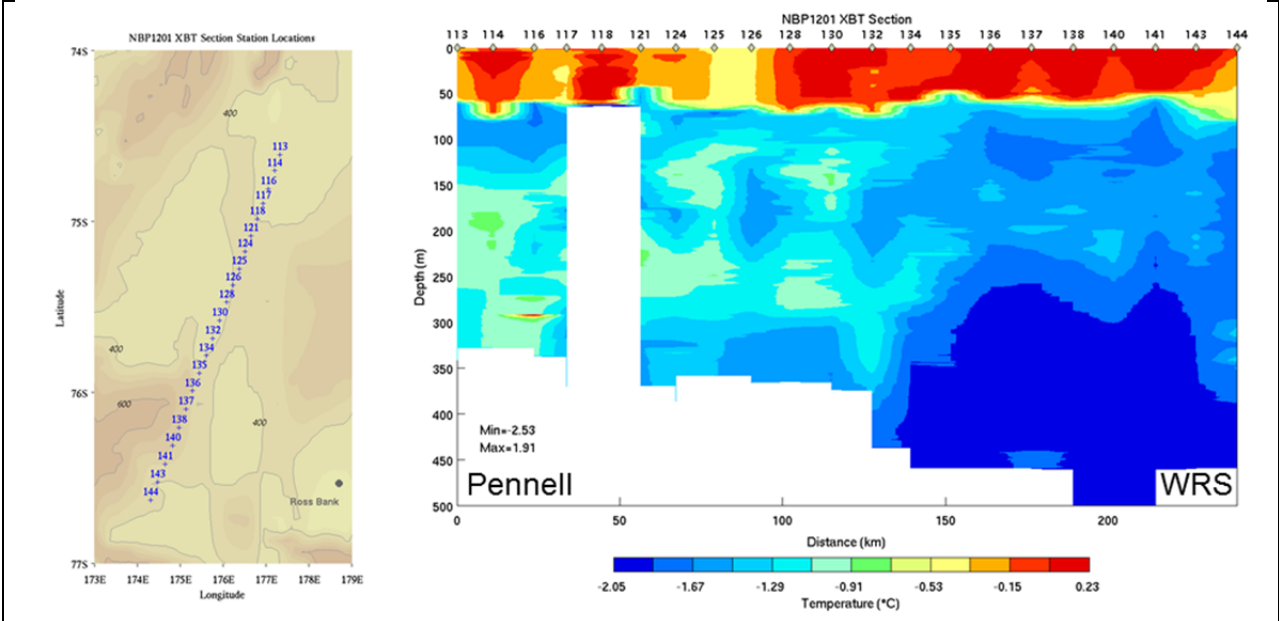
Figure JT.8. XBT transect from the easternmost station of the southwestern transect of Joides Trough (located on Pennell Bank) to the western Ross Sea.
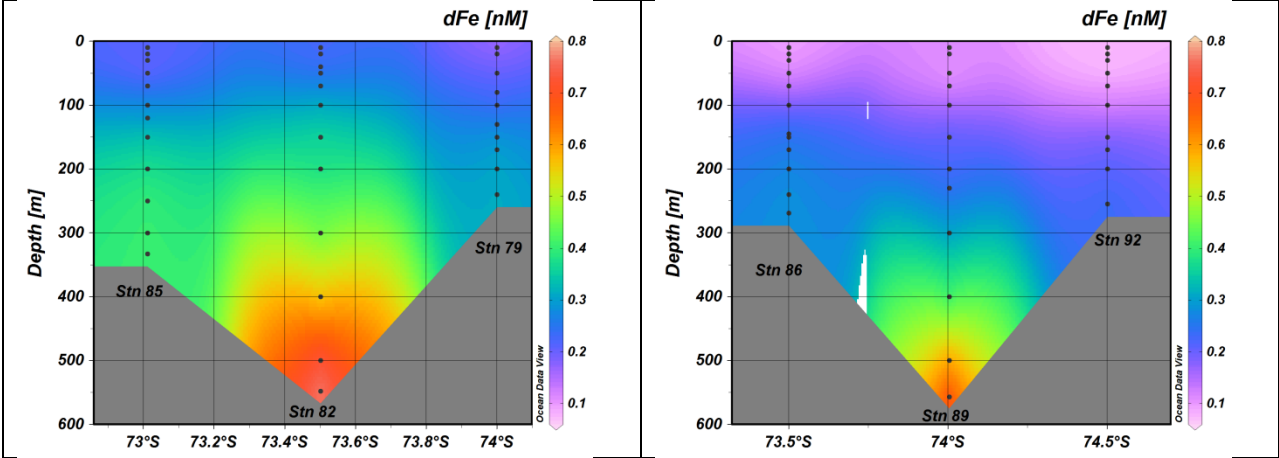

Figure JT.9. Dissolved iron concentrations along the northeast (left) and southwest (right) transects across Joides Trough.
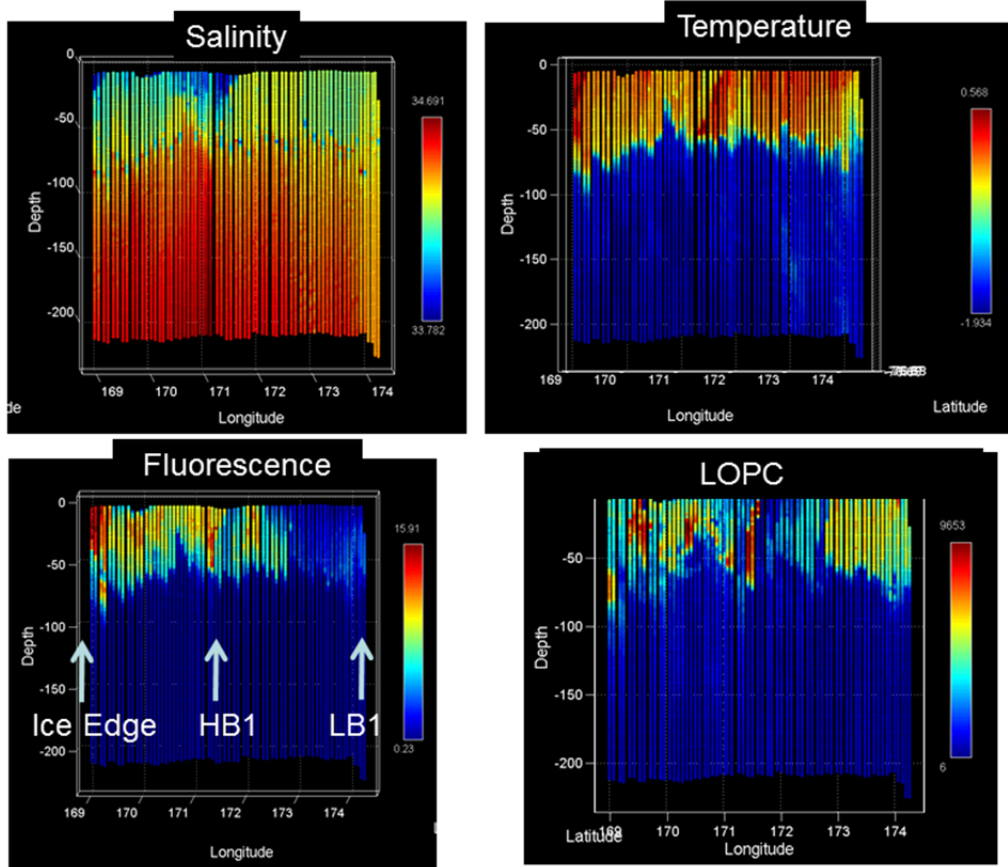
Figure WRS2.1. MVP survey along the second occupation of 76° 40'S.

Figure WRS2.2. CTD transect along the second occupation of 76° 40'S, including 3 stations further west that were inaccessible due to ice during the first occupation.

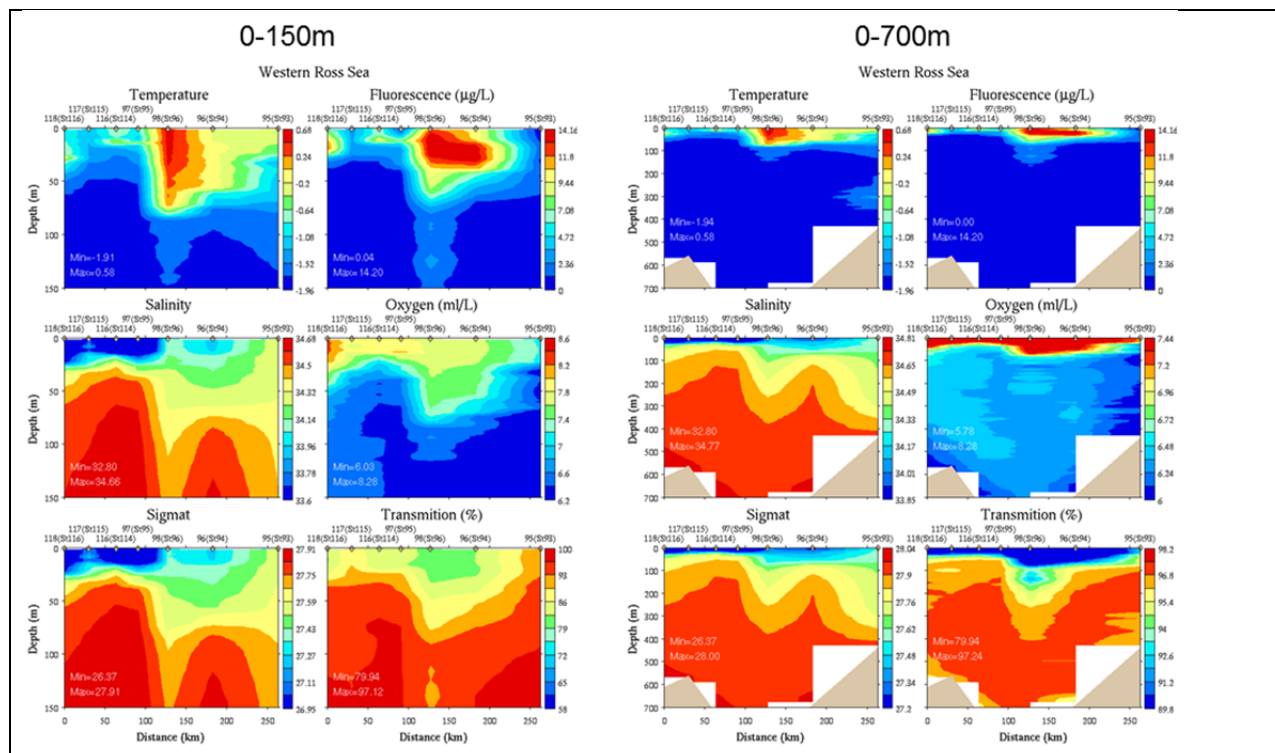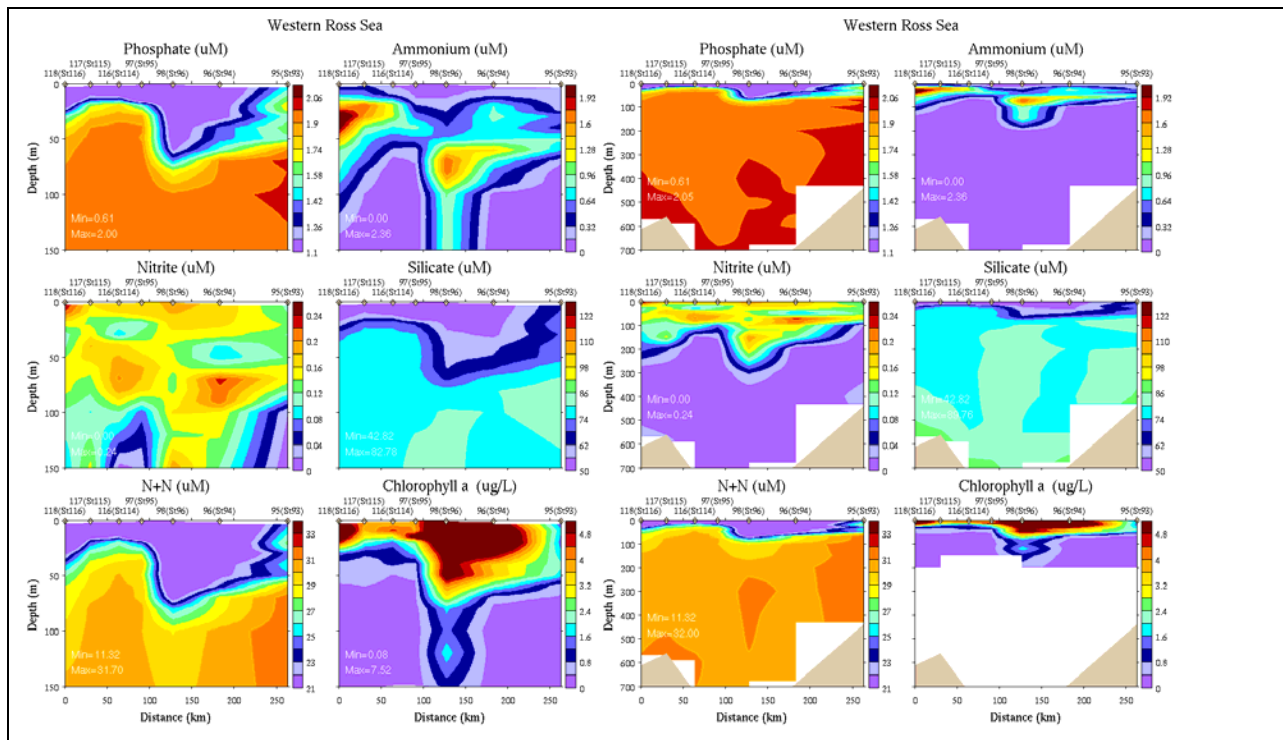Figure WRS2.3. Nutrient transect along the second occupation of 76° 40'S, including 3 stations further west that were inaccessible due to ice during the first occupation.
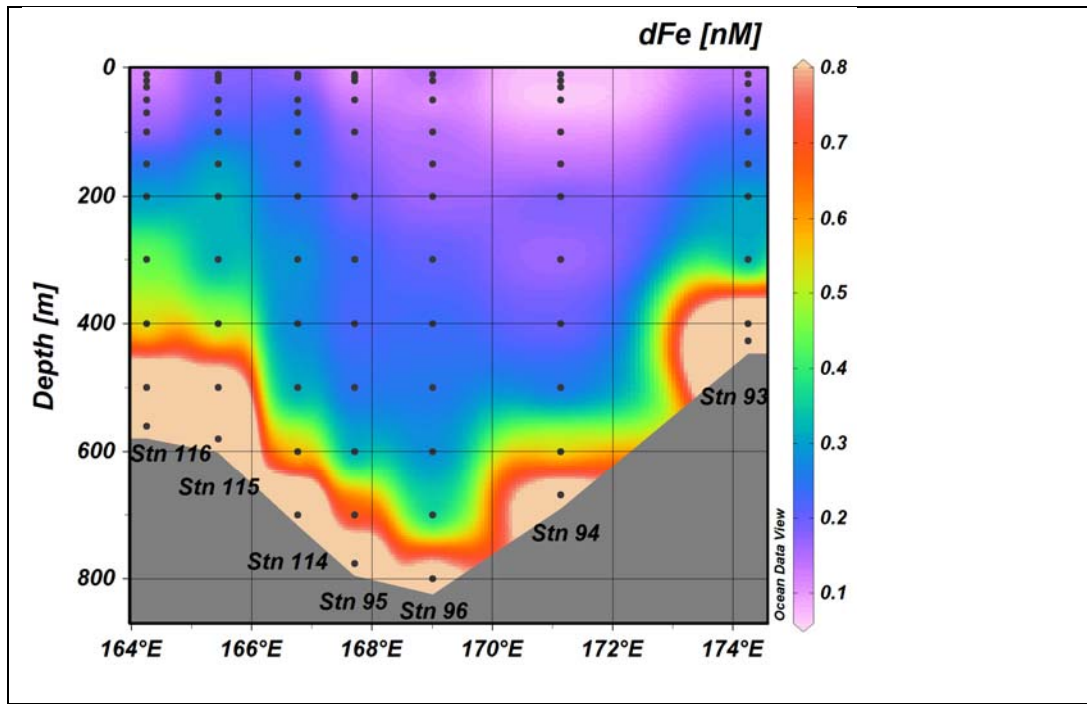
Figure WRS2.4. Dissolved iron along the CTD section shown in FigureWRS2.2,3.
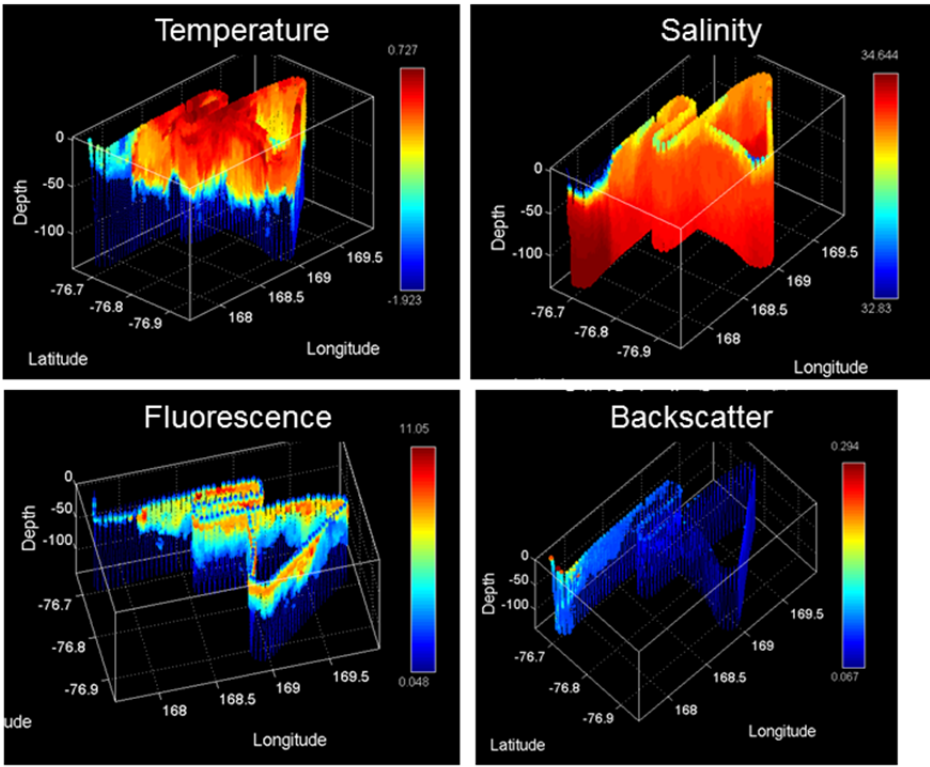
Figure WRS2.5. VPR survey of the Ice Edge Eddy (VPR11).
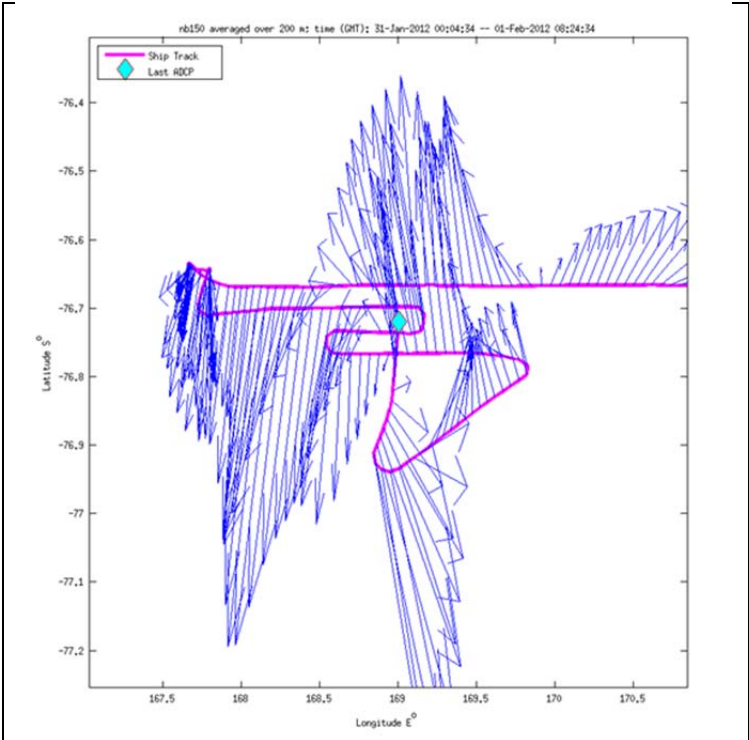
Figure WRS2.6. 0-200m ADCP velocity vectors for the VPR survey of the Ice Edge Eddy (VPR11).
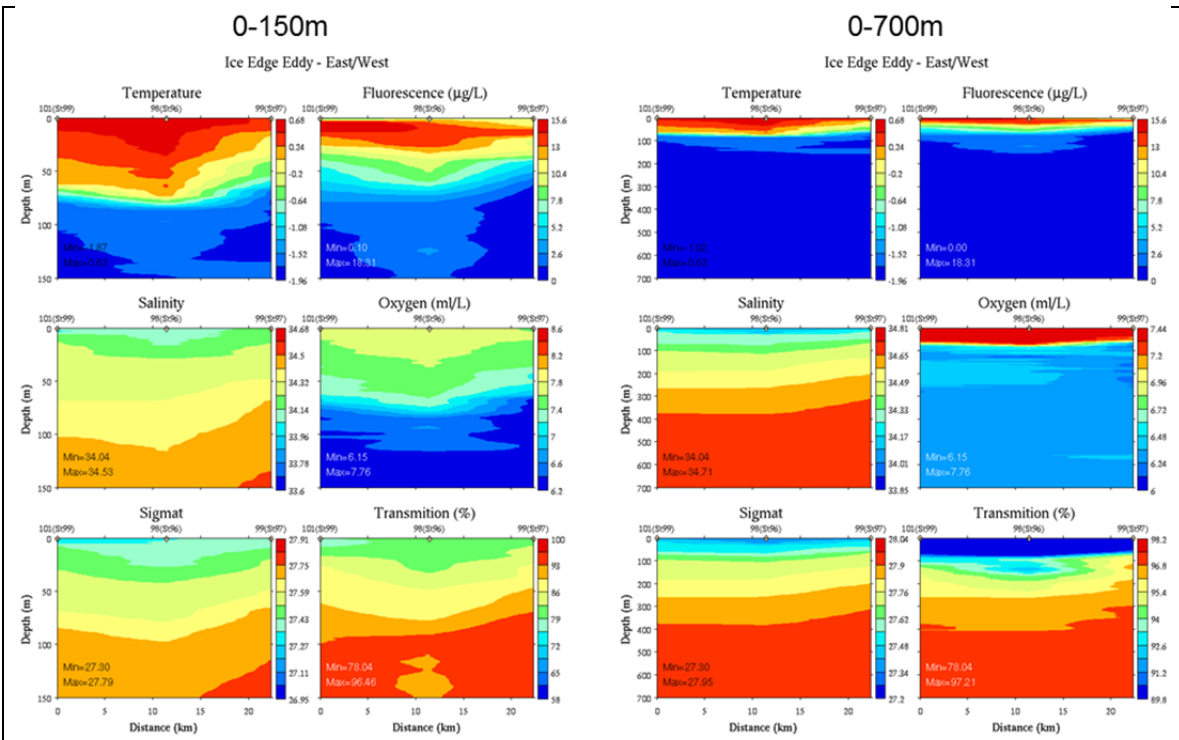
Figure WRS2.7. East-west section across the Ice Edge Eddy.
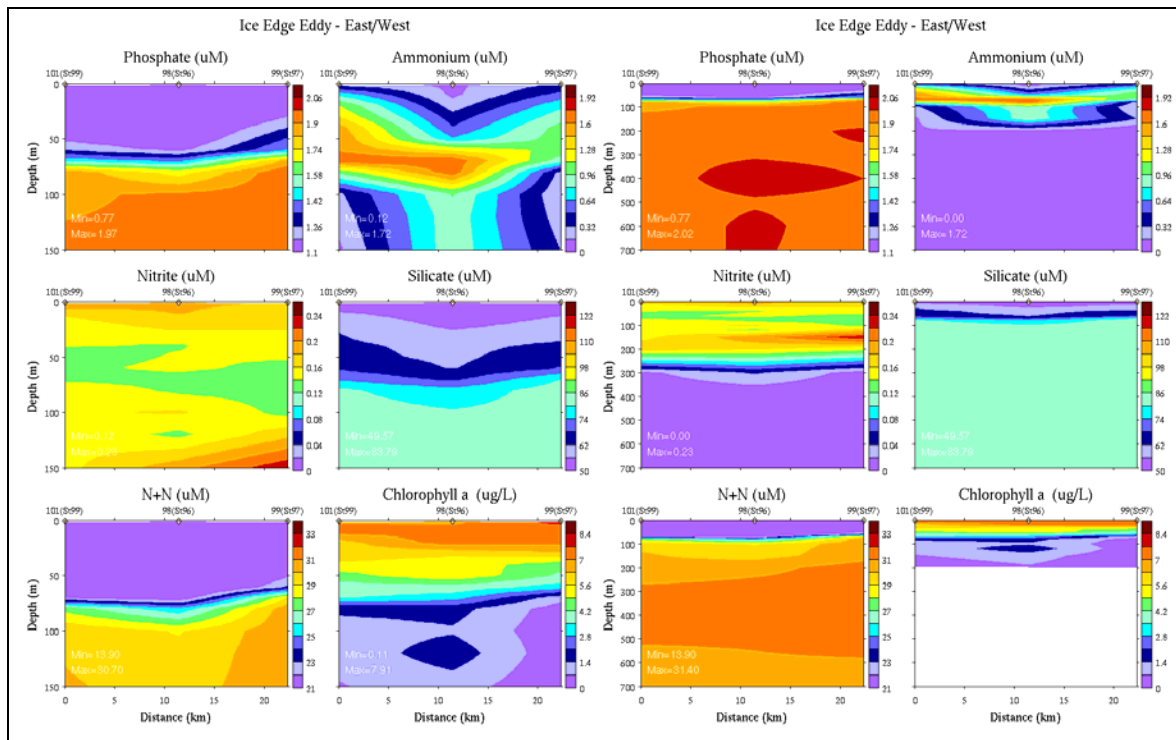
Figure WRS2.8. East-west section across the Ice Edge Eddy.
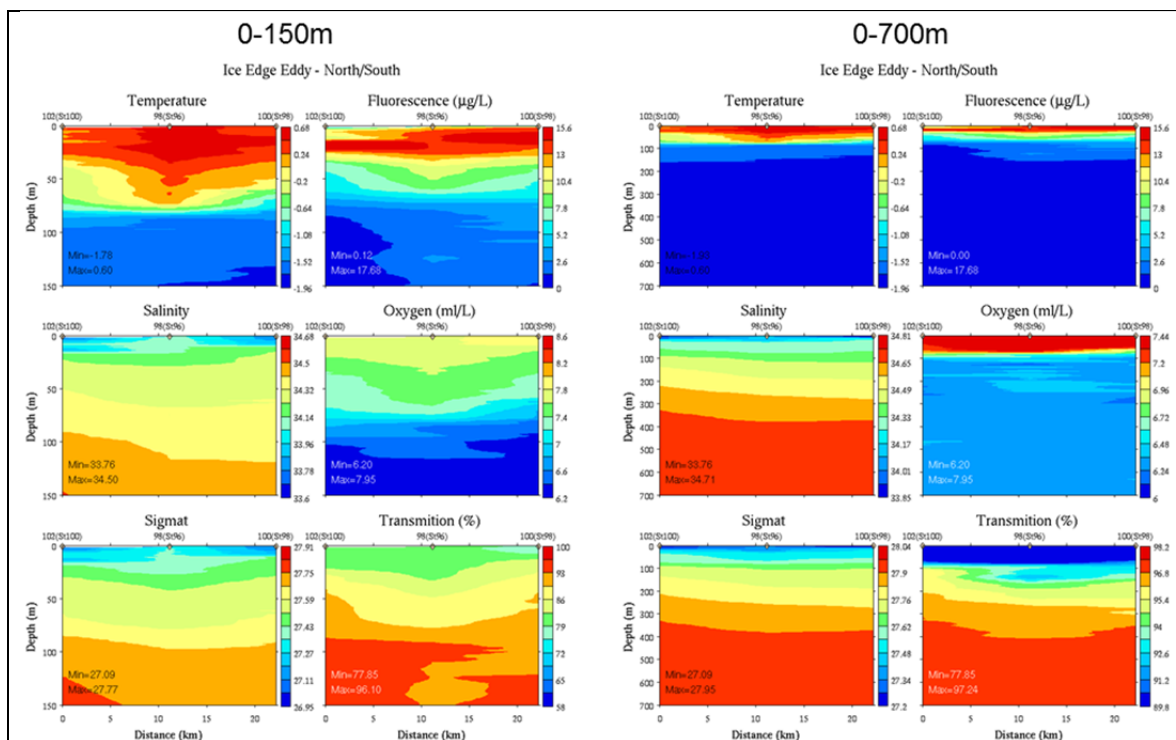
Figure WRS2.9. North-south section across the Ice Edge Eddy.
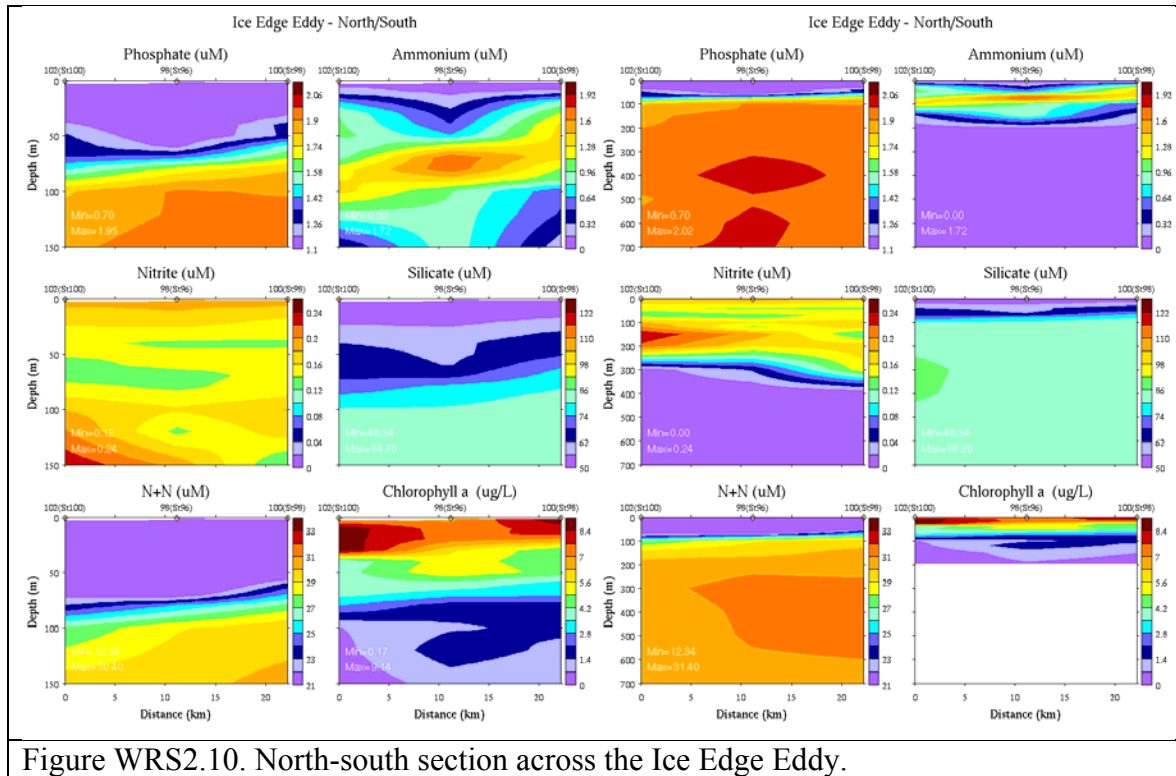
Figure WRS2.10. North-south section across the Ice Edge Eddy.
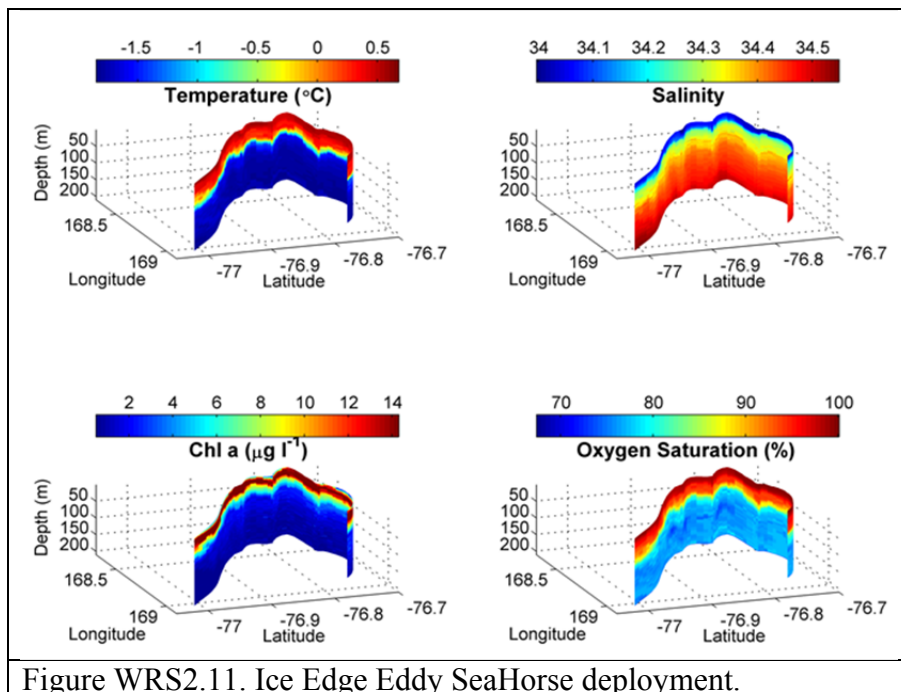
Figure WRS2.11. Ice Edge Eddy SeaHorse deployment.
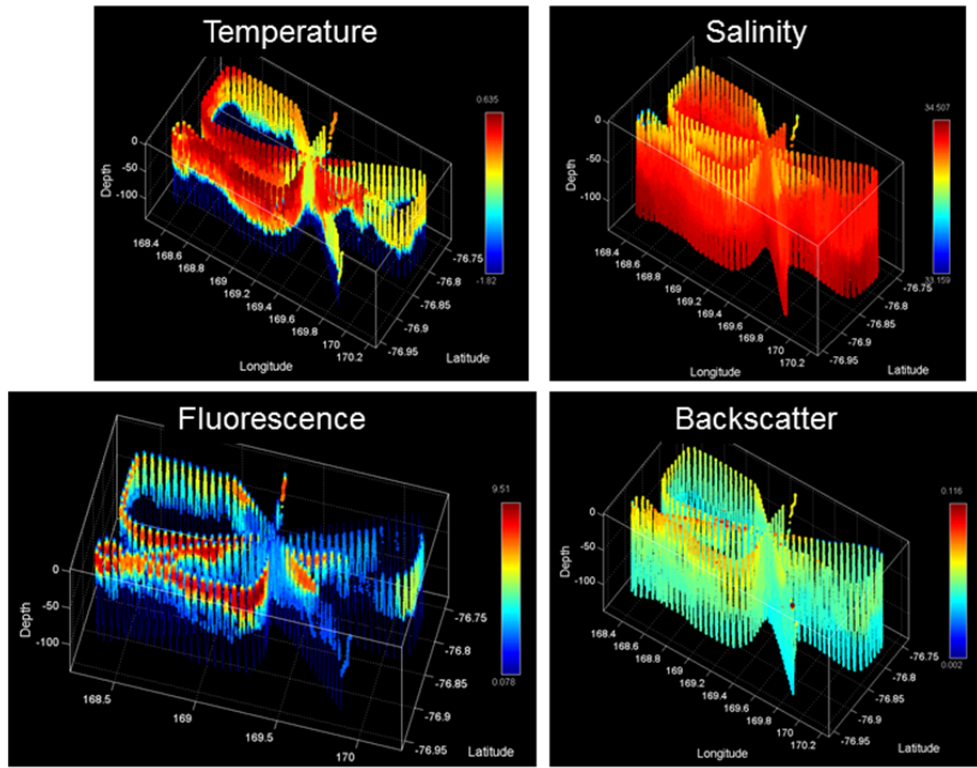
Figure WRS2.12. Second VPR survey of the Ice Edge Eddy (VPR13).
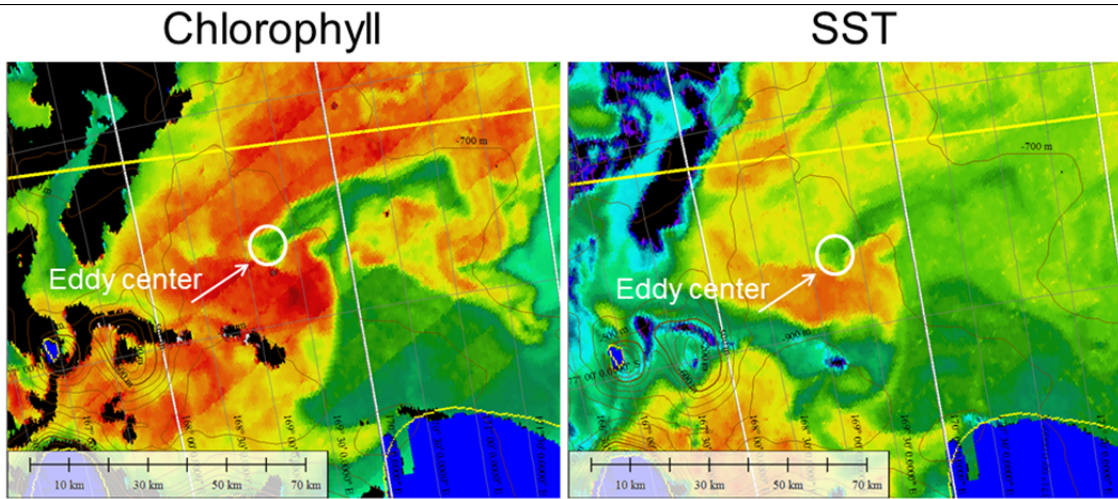
Figure WRS2.13. MODIS SST and chlorophyll imagery for February 4.
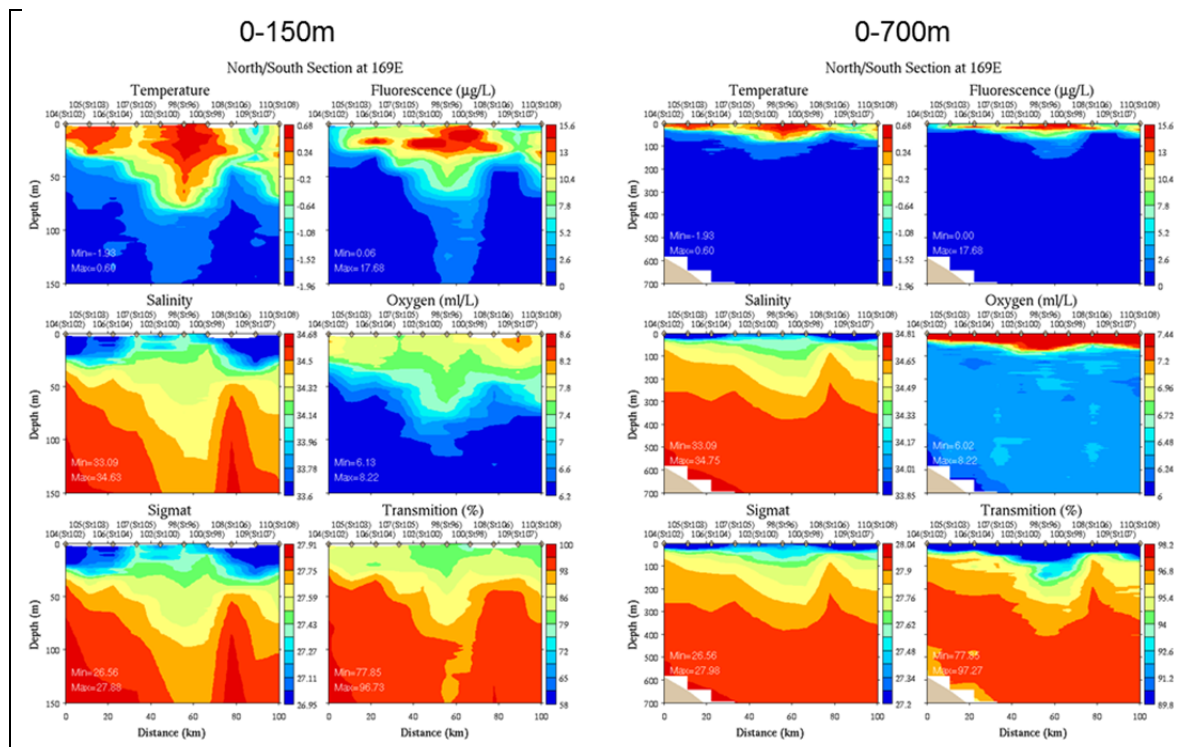
Figure WRS2.14. North-south CTD section along 169°E.
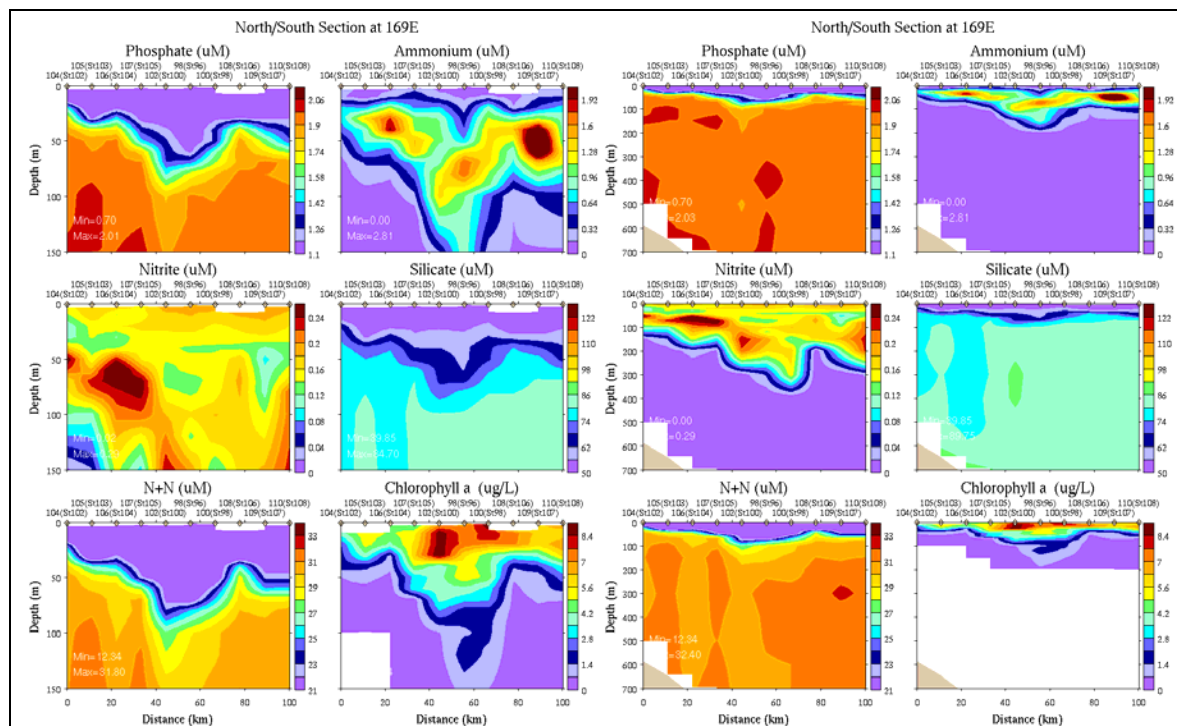
Figure WRS2.15. North-south nutrient section along 169°E.
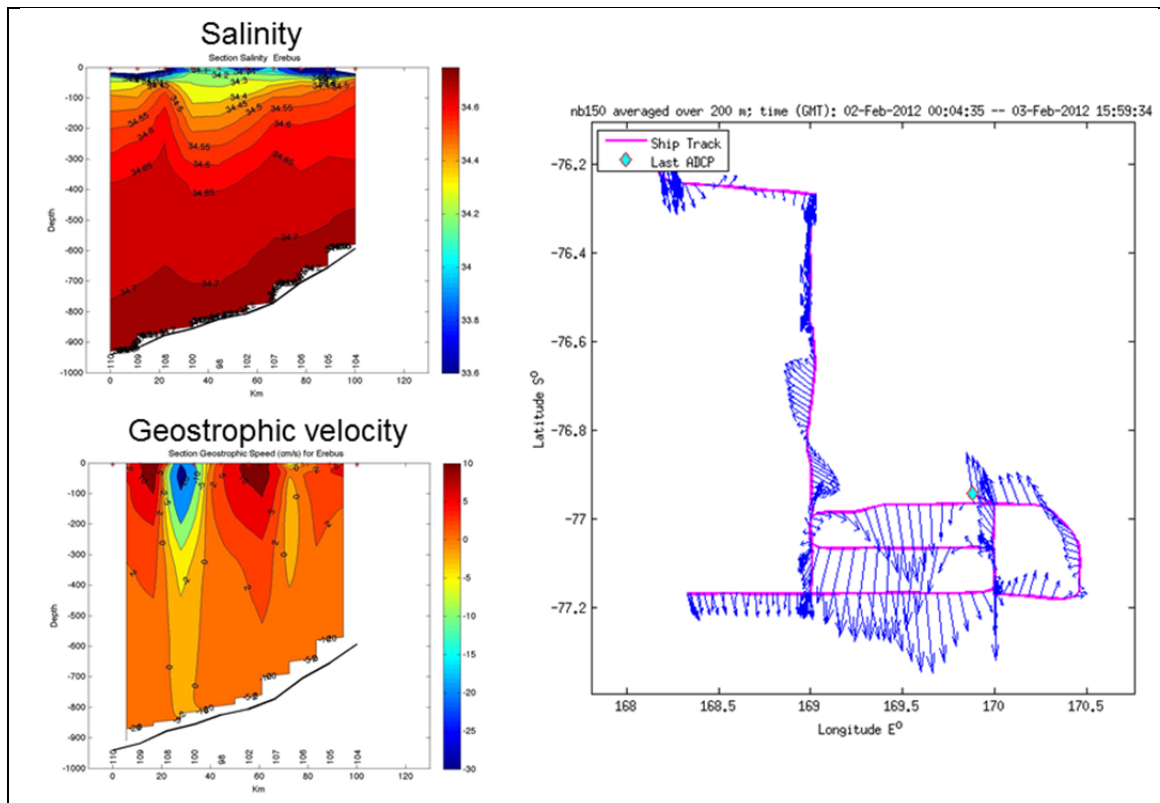
Figure WRS2.16. Left column: salinity and geostrophic velocity for the north-south section at 169°E (Source: John Klinck). Right column: 0-200m ADCP velocity vectors for the 169°E section followed by the frontal survey.
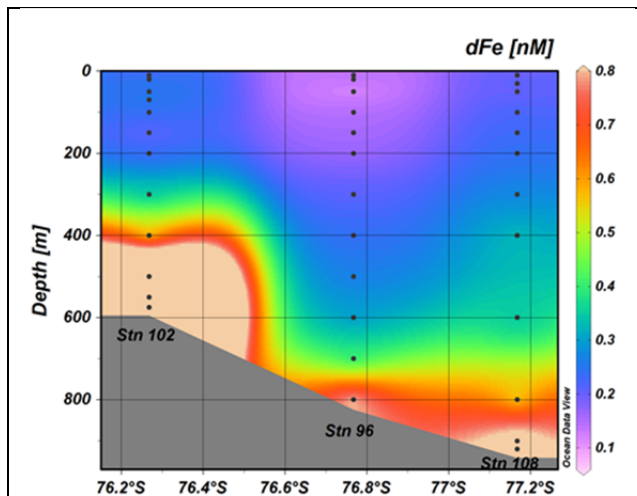
Figure WRS2.17. Dissolved iron concentration along the 169°E CTD section.
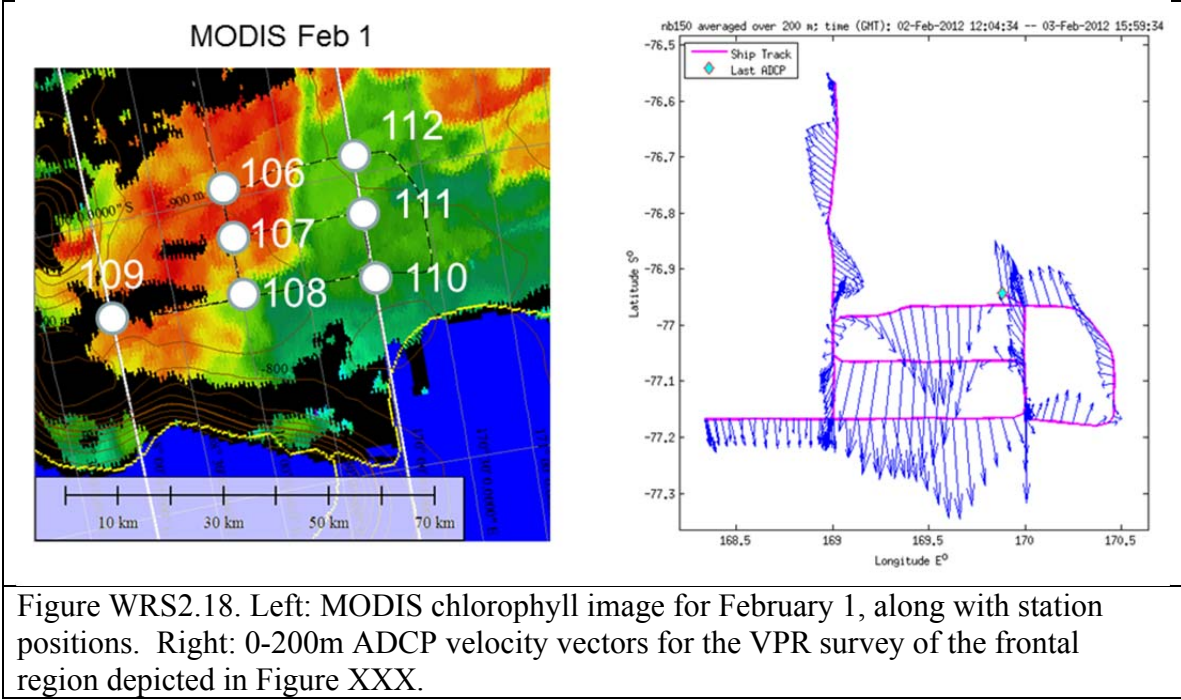
Figure WRS2.18. Left: MODIS chlorophyll image for February 1, along with station positions. Right: 0-200m ADCP velocity vectors for the VPR survey of the frontal region depicted in Figure XXX.
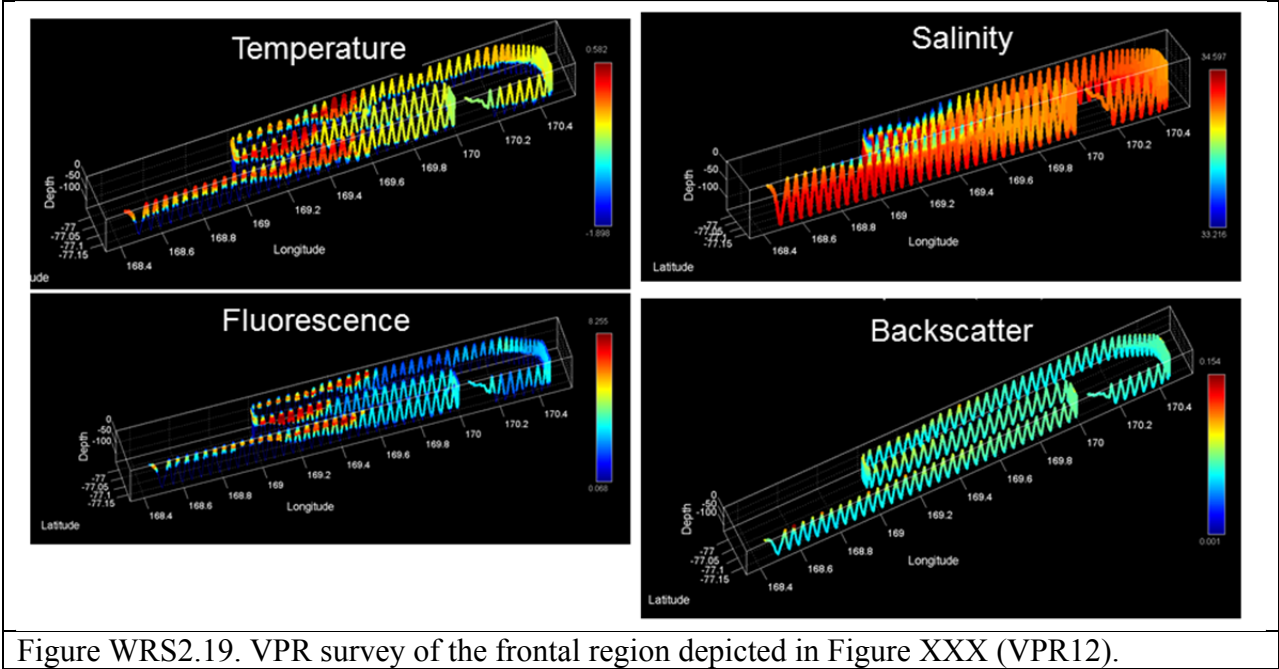
Figure WRS2.19. VPR survey of the frontal region depicted in Figure XXX (VPR12).

0-150m

Cross-front Section - North

Temperature

Fluorescence (µg/L)

Salinity

Oxygen (ml/L)

Sigmat

Transmition (%)

Distance (km)

0-700m

Cross-front Section - North

Temperature

Fluorescence (µg/L)

Salinity

Oxygen (ml/L)

Sigmat

Transmition (%)

Distance (km)
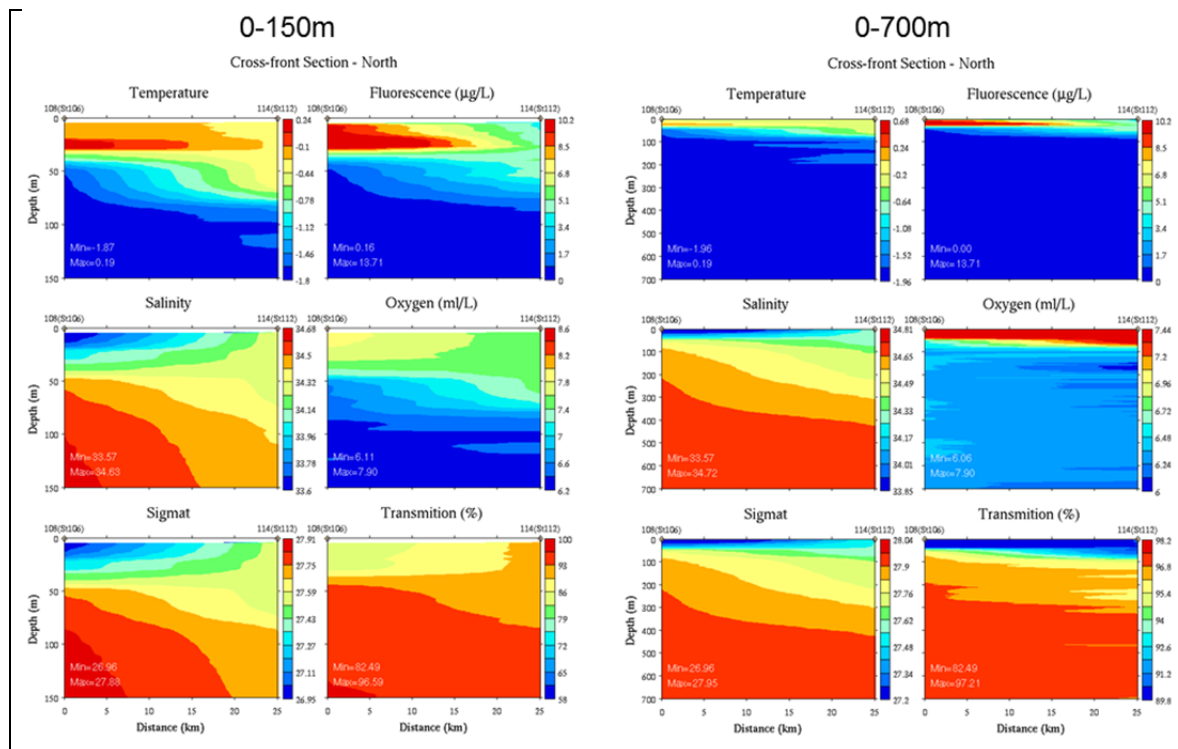
Figure WRS2.20. Across-front CTD section: north.

Cross-front Section - North

Phosphate (uM)

Ammonium (uM)

Nitrite (uM)

Silicate (uM)

N+N (uM)

Chlorophyll a (ug/L)

Distance (km)

Cross-front Section - North

Phosphate (uM)

Ammonium (uM)

Nitrite (uM)

Silicate (uM)

N+N (uM)

Chlorophyll a (ug/L)

Distance (km)
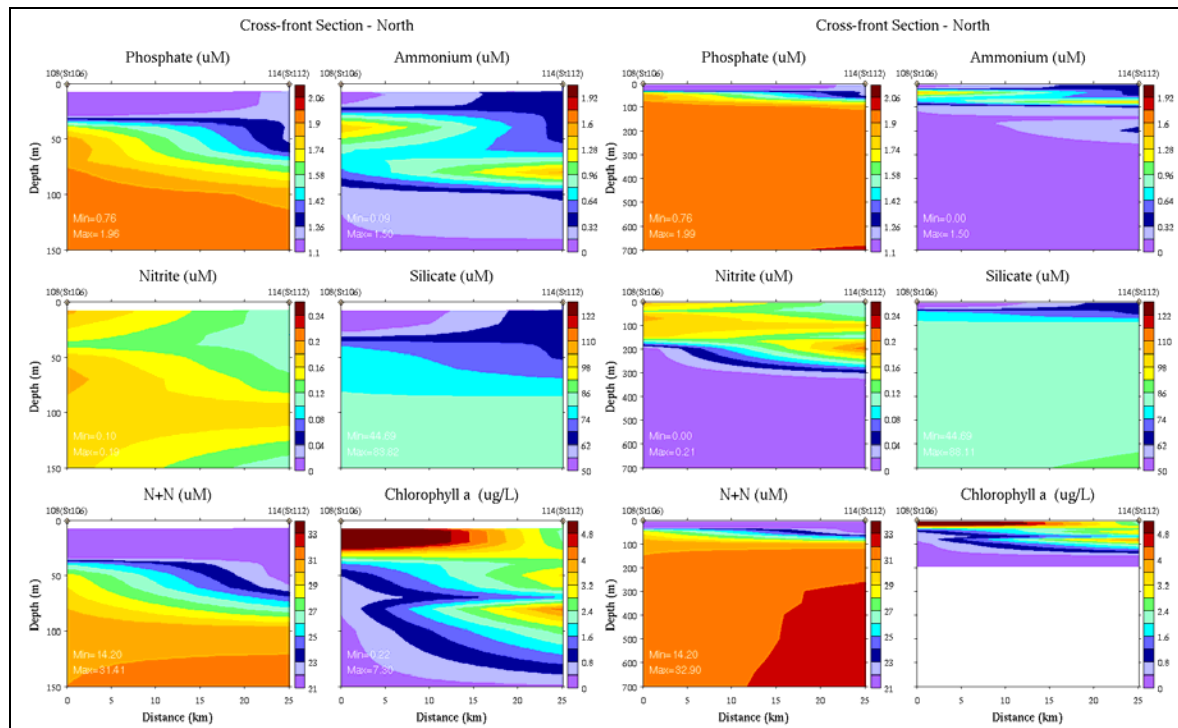
Figure WRS2.21. Across-front nutrient section: north.
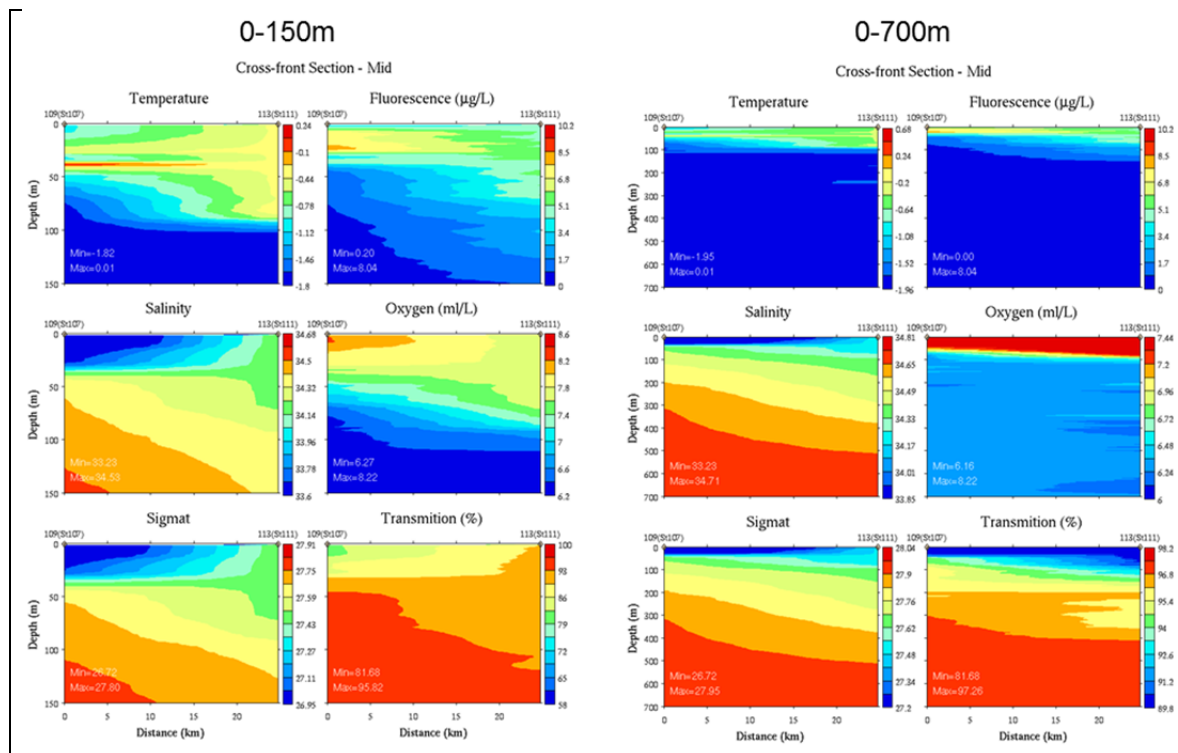
Figure WRS2.22. Across-front CTD section: middle.
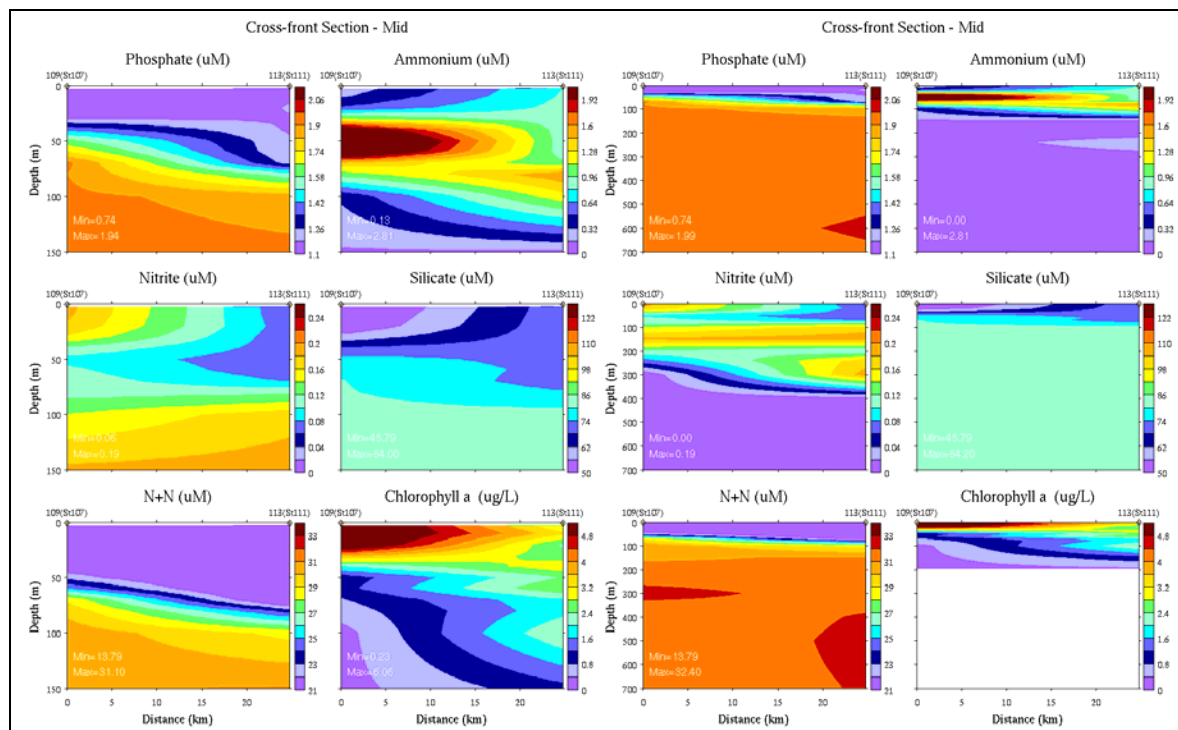
Figure WRS2.23. Across-front nutrient section: middle.

0-150m

0-700m
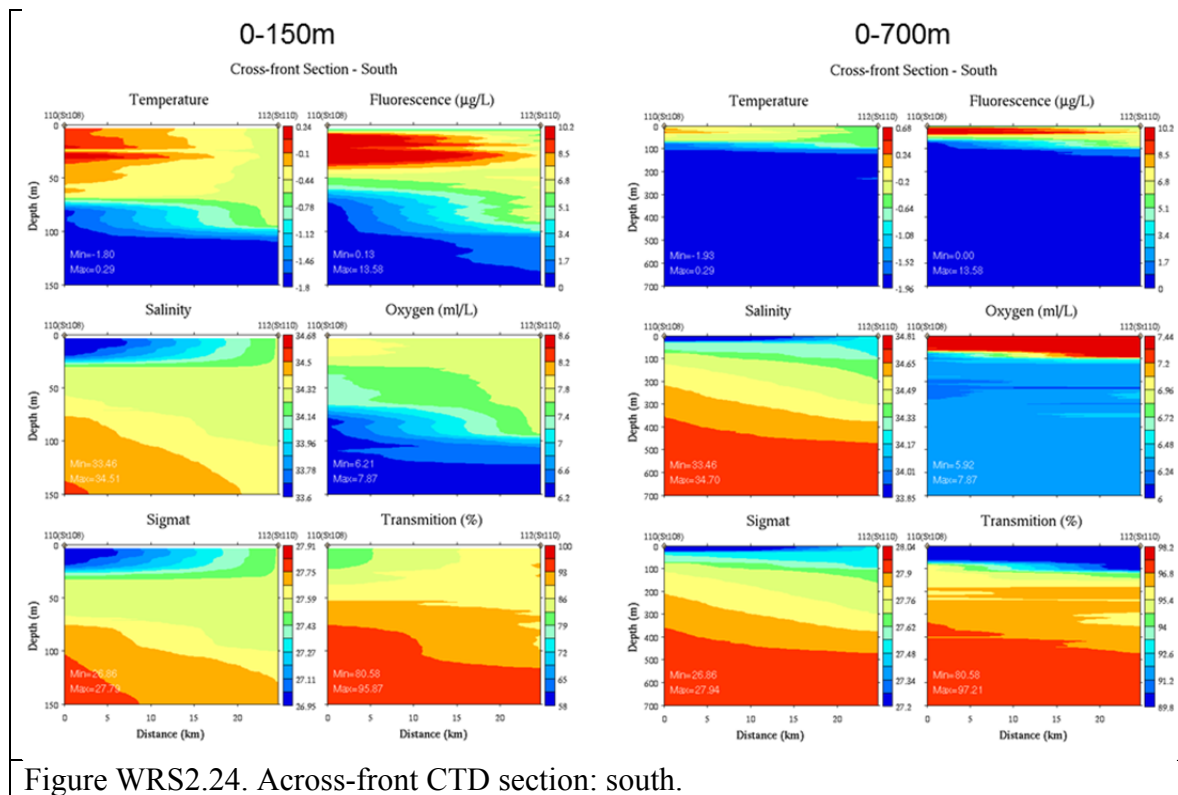
Figure WRS2.24. Across-front CTD section: south.
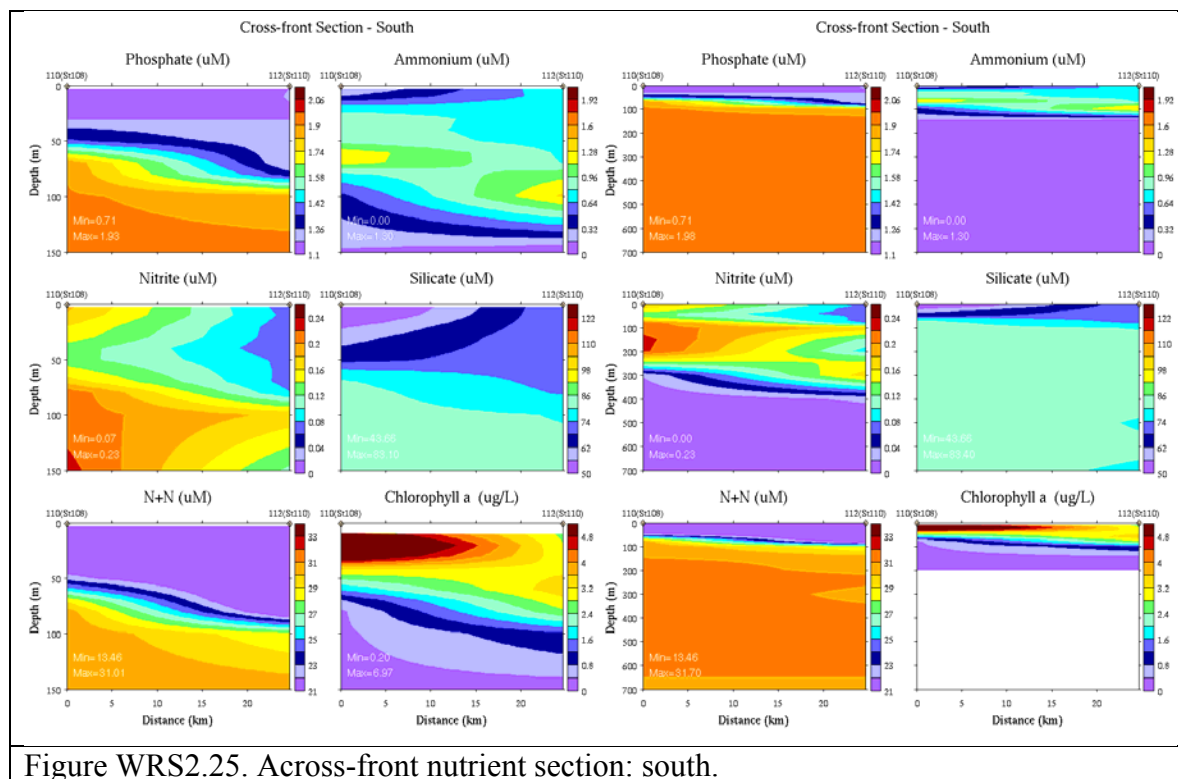
Figure WRS2.25. Across-front nutrient section: south.
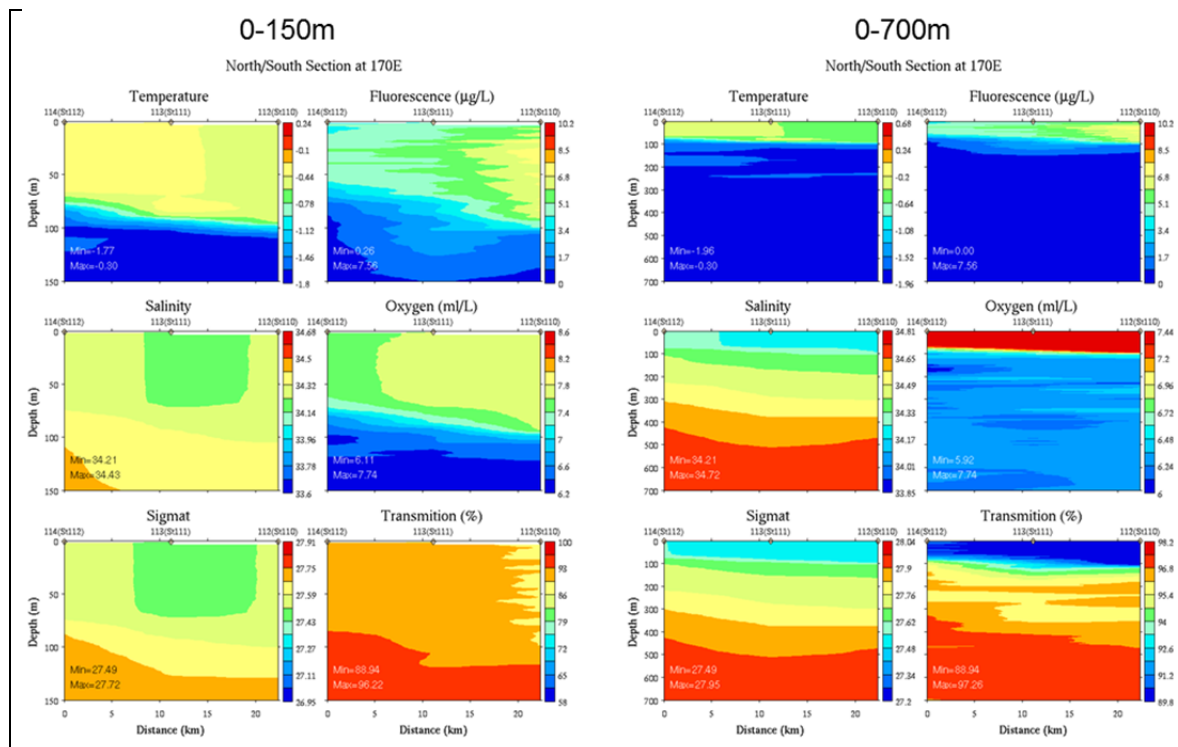
Figure WRS2.26. Along-front CTD section.
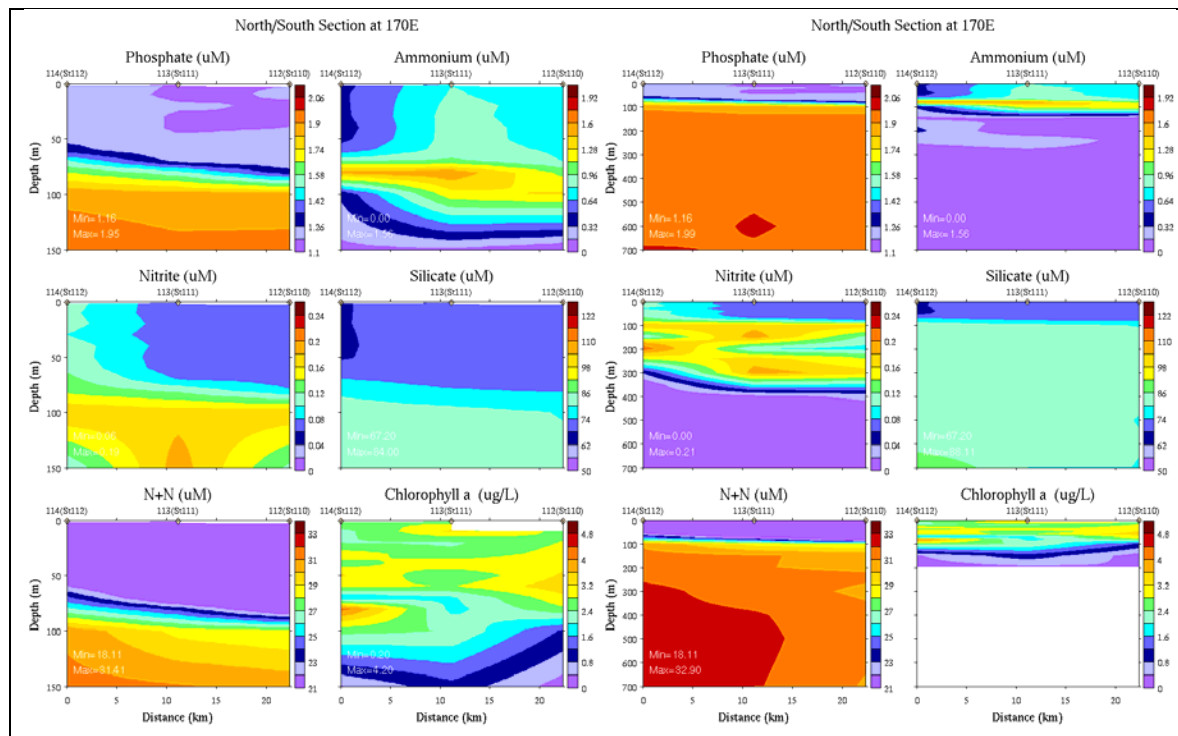
Figure WRS2.27. Along-front nutrient section.
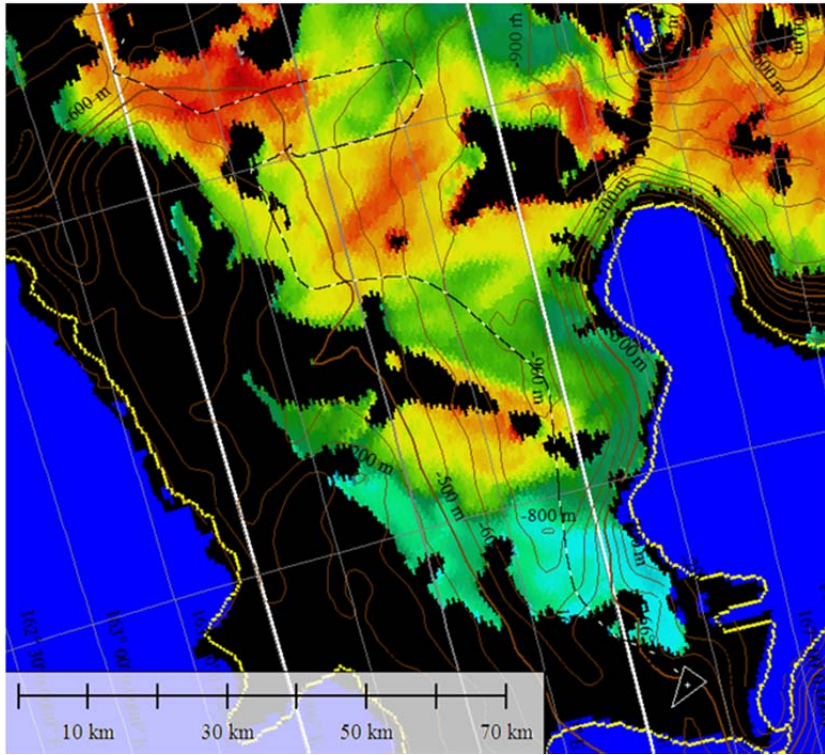
Figure WRS2.28. Western Ross Sea – McMurdo Sound VPR
survey trackline overlayed on Feb 4 MODIS chlorophyll image.
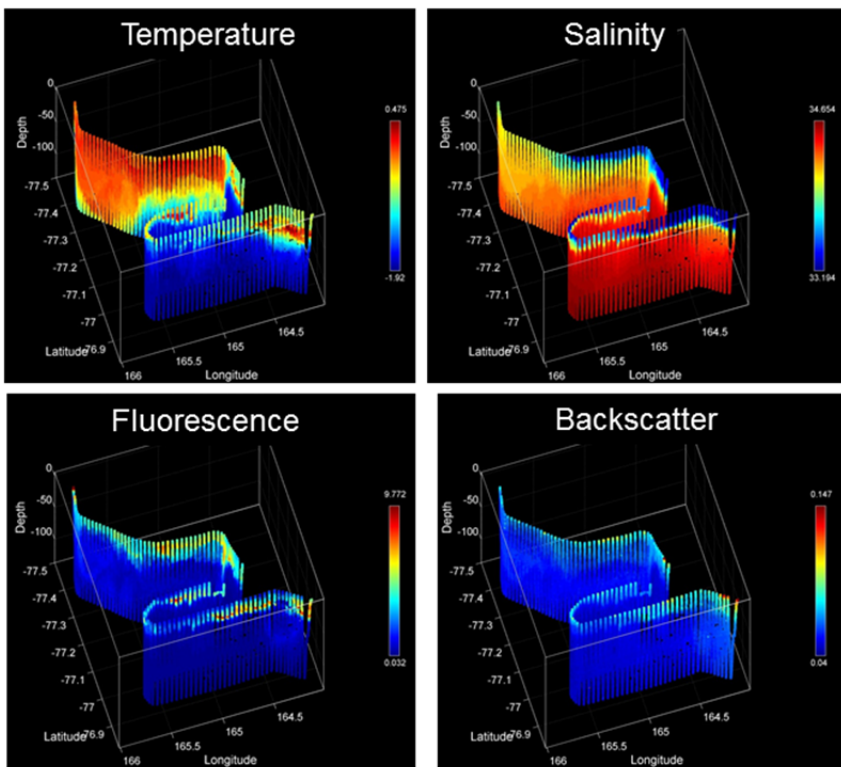
Figure WRS2.29. Western Ross Sea – McMurdo Sound VPR survey (VPR 13/14).
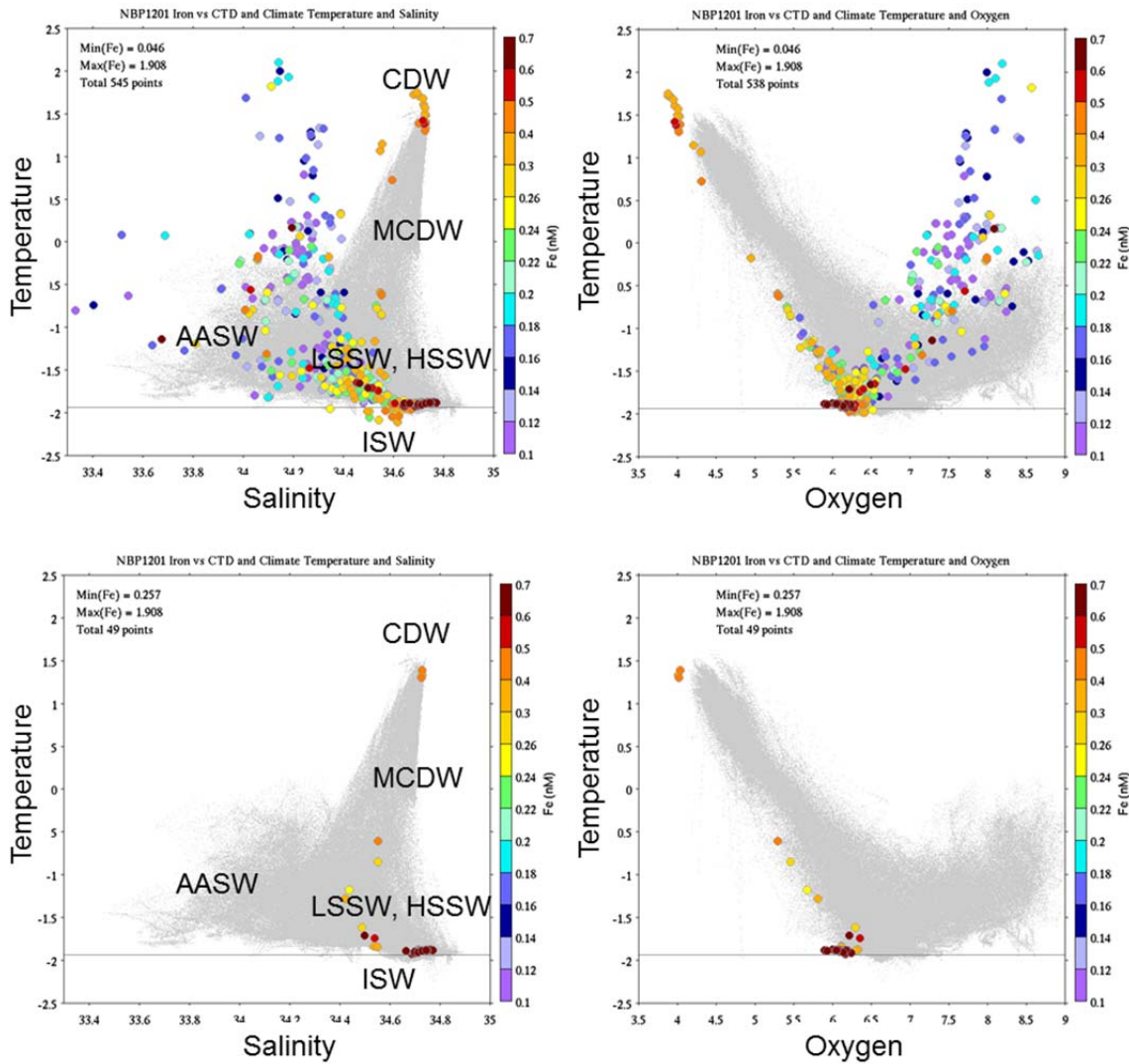
Figure Conc.1. Top: Dissolved Fe plotted as a function of temperature and salinity (left) and temperature and oxygen (right); Bottom: same as above, but only the deepest sample for each cast is plotted.

Figure Conc.2. N:P and N:Si ratios for PRISM nutrient data.

Figure Conc.3. Nutrients, ratios, chlorophyll, and dissolved iron concentrations.
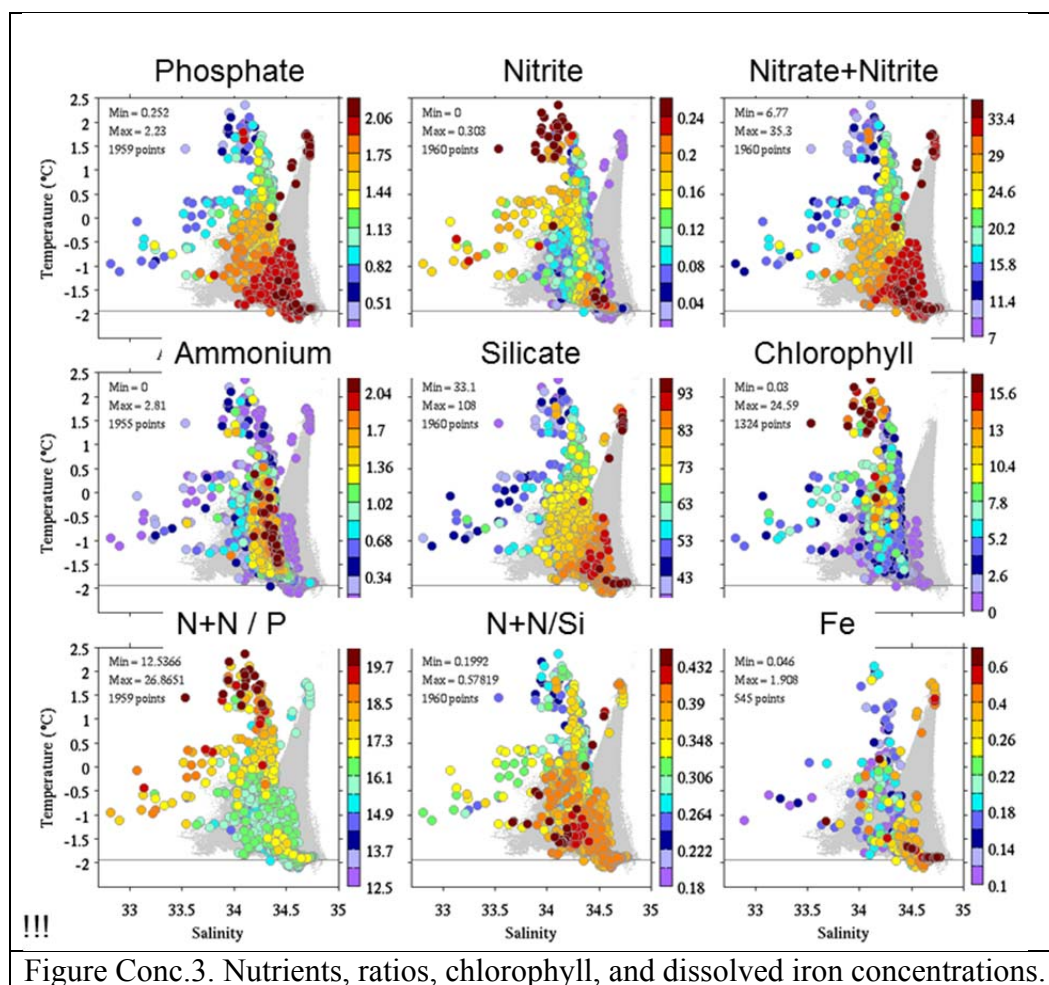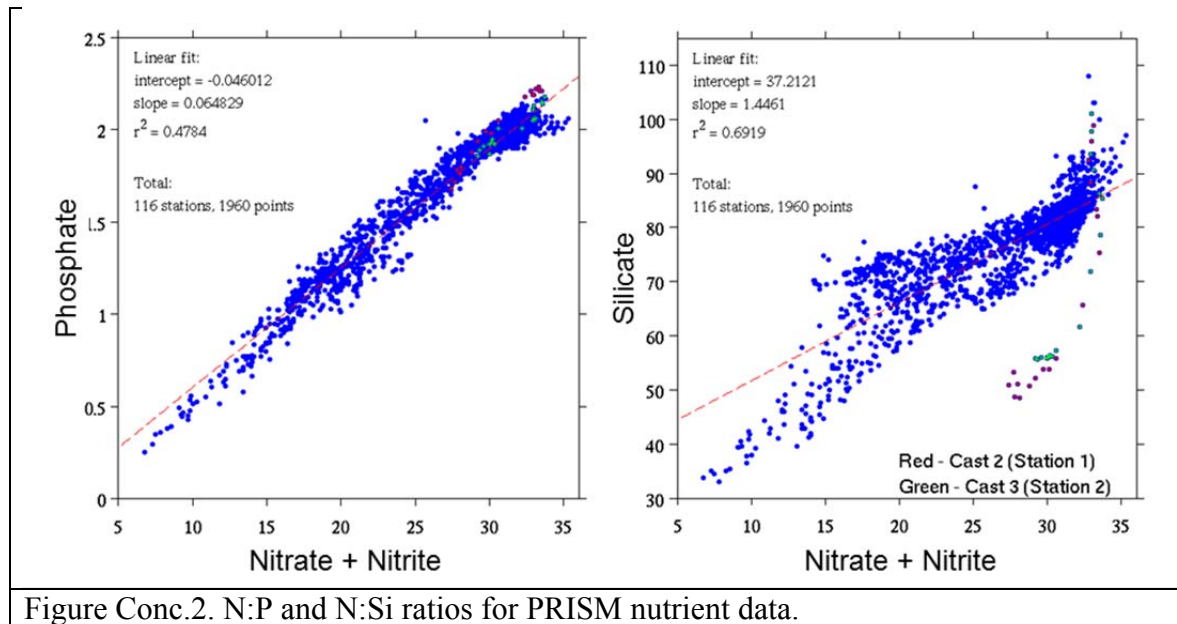
Long-Term: Incubation Experiment 1 – Eddy 2
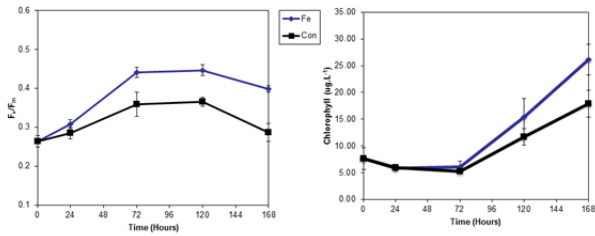
Long-Term: Incubation Experiment 2 – Ross Bank
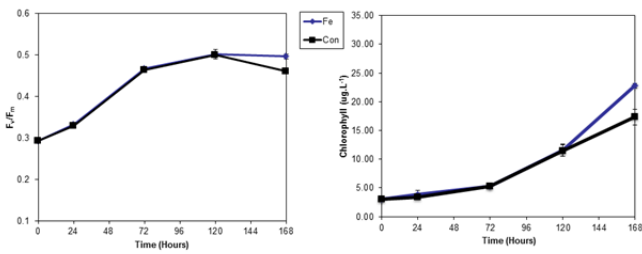
Long-Term: Incubation Experiment 3 – Ross Ice Shelf
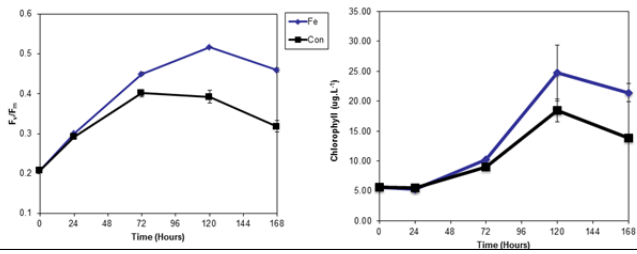
Figure Conc.4. Long-term incubation results from Bibby/Ryan-Keogh.
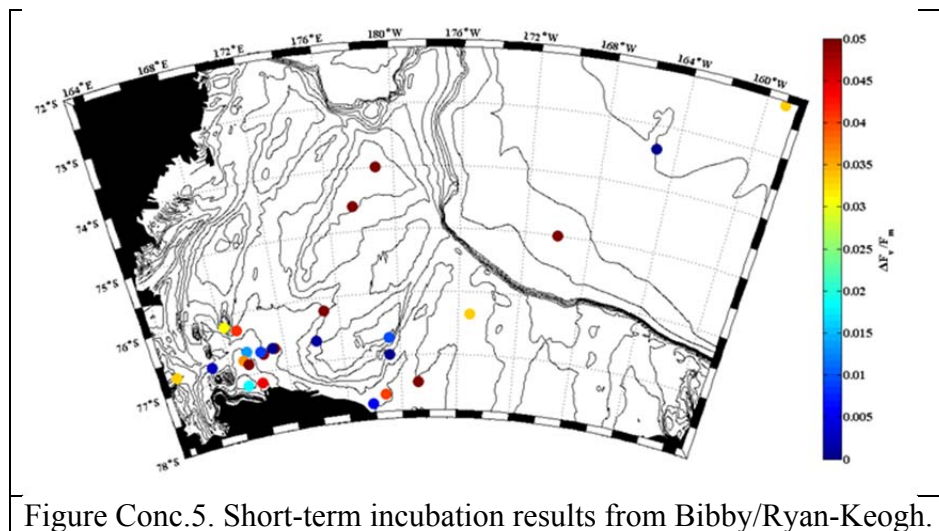
Figure Conc.5. Short-term incubation results from Bibby/Ryan-Keogh.

Figure Conc.6. Short-term incubation results from Bibby/Ryan-Keogh.
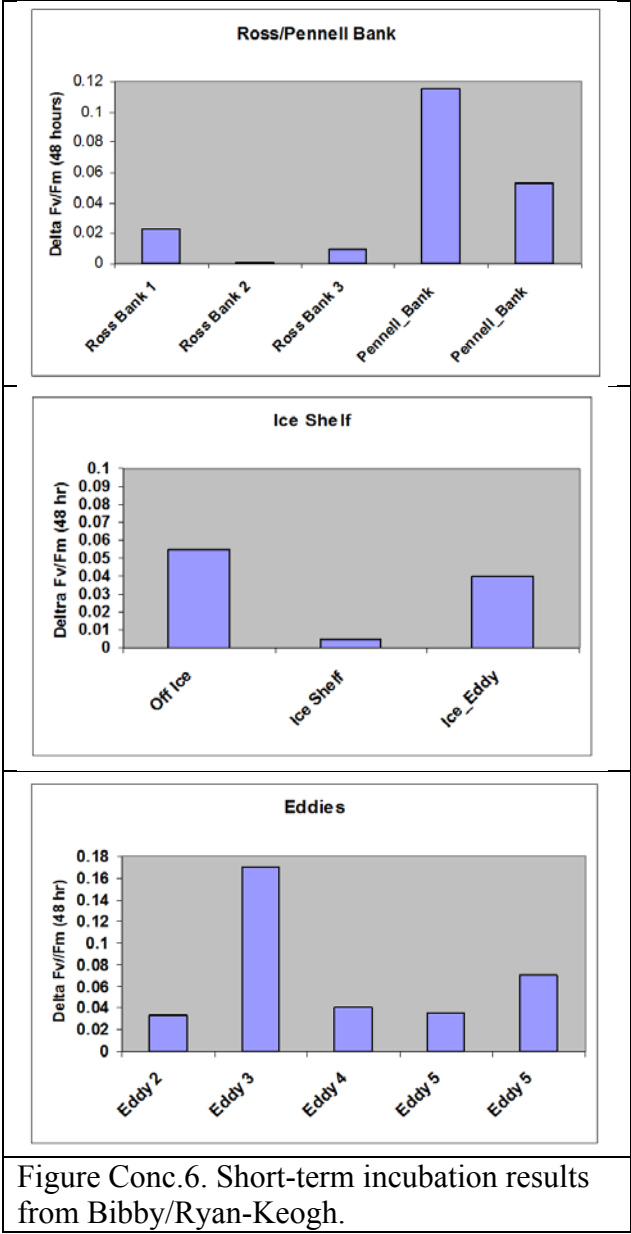
Appendix A. Cruise participants

Al Hickey MPC
Dennis McGillicuddy
RPSC Dan Powers MT
RPSC Chris Linden (Multibeam)
Elise Olson
Olga Kosnyrev
Josh Eaton
Robb Hagg
RPSC Lindsey Ekern MST
RPSC Kim Null MST
Walker Smith
RPSC Andy Nunn ET
RPSC Barry Bjork ET
Bettina Sohst
Candace Wall
RPSC Diane Hutt MST
RPSC Amy Schuab MT
RPSC Julian Race IT
RPSC Joe Tarnow IT
Stephanie Hathcock
Doan Nhu Hai
Sean Charles
Tommy Purcell MT
Jeff Arlingstall MT
Liza DeLizo
Anna Mosby
Chris (Geordie) Marsay
Tom Bibby
Pamela Barrett
Jennifer Bennett
John Klinck
Blair Greenan
Randy King
Marco Pedulli
Suriyan Saramul
Pierre St Laurent
Tommy Ryan-Keogh
Peter Sedwick

Appendix B. Daily narrative

December 24 - Departure, testing of the MVP and VPR outside the Straits of Magellan.

December 31 – CTD test cast.

January 1-3 – VPR tow.

January 6 – Station 1, offshore of ice pack. Bibby incubation.

January 7 – Station 2, inside ice pack. Bibby incubation. Breaking through thick ice.

January 8 – Station 3, inshore of ice pack; MVP/towfish survey to Eddy 1

January 9 – Station 4, inside eddy; short MVP tow to outside eddy; Station 5 outside eddy; MVP survey to Eddy #2, station #6 inside eddy. VPR survey from inside Eddy 2 to its SE corner; operations suspended upon receipt of a mayday call from a Korean fishing vessel.

January 10 – Transit to McMurdo

January 11 – Evacuation of survivors, recommencement of science ops at ice edge, station 7.

January 12 – MVP/towfish ops High biomass station 8, low biomass station 9.

January 14-15: VPR survey of eddy 3; SeaHorse deployment; station 10 at eddy center; SeaHorse re-deployment.

January 15-16: Cross-pattern of hydro stations in Eddy 3 (stations 11-18).

January 16-17: VPR survey of frontal region between high and low biomass areas; three stations acrost from east to west (19-20-21). VPR survey of low-biomass region, stations 22-23-24-25-26 in east-west line.

January 18-19: MVP survey back to Eddy 3, crossing from east to west. VPR survey reoccupation of the same line for intercalibration of MVP/VPR; continued final survey of Eddy 3, followed by CTD grid, stations 27-35. Recovery of SeaHorse during CTD survey.

January 19-20: MVP challenged by icing conditions; VPR survey to Ross Bank; survey of Ross Bank.

January 20-22: CTD survey of Ross Bank (Stations 36-55). Deployment of SeaHorse.

January 23-24 MVP Survey from Ross Bank to Ross Ice Shelf

January 25: Ross Ice Shelf CTD section; VPR survey of Ross Ice Shelf eddy; begin CTD survey of eddy feature

January 26: Completion of Ross Ice Shelf eddy CTD survey; transit to Ross Bank; beginning of reoccupation of SE-NW section of the bank

January 27: Completion of the SE-NW section, recovery of SeaHorse, deployment of VPR.

January 27-28: VPR survey from Ross Bank to Joides Trough

January 29-30: Joides Trough CTD/MVP survey

January 30-31: MVP/towfish survey from Joides to 76 40 line; Low Biomass – High Biomass – Ice Edge stations

Feb 1-2: VPR survey of Ice Edge Eddy, deployment of SeaHorse. As expected from the VPR survey, the station at eddy center (96) yields high abundance of kidney beans, confirmed with the microscope as *Phaeocystis* debris. Additional stations in Ice Edge eddy, Franklin Island Station.

Feb 2-3: N-S section along 169, along with time-series occupation at Jacobs Gulch; VPR survey of frontal region; stations 110-112.

Feb 4: VPR survey from frontal region back to Eddy Center; station at eddy center including hoop net tow.

Feb 5: Three stations west of ice edge; VPR survey of Western Ross Sea and north McMurdo Sound

Feb 6: In ice for cargo ops.

Feb 7: Fueling with the R/V Itallica.

Feb 8: Cargo ops.

Feb 9: In ice; packing.

Feb 10: Arrival at McMurdo.

Feb 11: Disembark NBP.

Appendix C. VPR log

Dates	Tow ID	Comments
Jan 1	VPR1	In transit; recovered early
Jan 1-3	VPR2	In transit; diatom aggregates?
Jan 10	VPR3	Eddy 2 radial section
Jan 14-15	VPR4	Eddy 3 survey
Jan 16	VPR5	Frontal region between high and low biomass areas; no O_2 data
Jan 16-17	VPR6	Survey of low biomass area
Jan 18	VPR7	Re-survey of Eddy 3 core; includes intercalibration section with MVP
Jan 19-20	VPR8	Survey to and around Ross Bank
Jan 25	VPR9	Ross Ice Shelf eddy survey
Jan 27-28	VPR10	Ross Bank to Joides Trough; *Phaeocystis* to the SE, small bead-like diatom chains to the NW
Feb 1	VPR11	Survey of Ice Edge Eddy; lots of *Phaeocystis* with kidney beans in the middle.
Feb 3	VPR12	Frontal region: diatoms on top of *Phaeocystis* to the west, 100m layer of all *Phaeocystis* to the east.
Feb 4	VPR13	Survey of Ice Edge Eddy
Feb 5-6	VPR14/15	Western Ross Sea to McMurdo Sound

Appendix D. CTD Casts and Station Identifiers

CTD Cast #	Station #
1	Test
2-41	1-40
42	Profile at SeaHorse on Ross Bank
43-118	41-116

Appendix E. VPR observations of remnant *Phaeocystis* colonies

One of the most abundant classes of objects observed in VPR images from NBP12-01 consisted of irregular spheres. Due to their irregular shape and the fact that they were not readily identifiable as any known taxon or type of debris, they have been referred to as "beans". In the VPR images they appear as white opaque objects generally having a slightly deformed spherical shape. Several examples are presented in Figure E1. They have a dull texture typical of marine snow and were typically observed in highest concentrations between 70 and 120 m depth. Often, "beans" were found below areas of elevated *Phaeocystis* abundance.

In an effort to determine identity of these "beans", we took samples from Niskin bottles at several stations within the depth range where the objects were typically observed. Water was sieved gently through a 10 μm mesh and rinsed with filtered seawater into a petri dish or bottle for immediate observation under a dissecting microscope with the ability to capture photographs. At stations 96 and 113, in the center of the Ice Edge Eddy, depths were targeted based on VPR observations at that site. During the first of these eddy center stations, many objects of a shape consistent with "beans" were observed. Photographs of these objects taken through a dissecting microscope are presented in Figure E2 . These objects appeared to be broken and deflated spherical *Phaeocystis* colonies. One such object was transferred to a slide and photographed at higher magnification (Figure E3). Based on these observations, it seems likely that the "beans" observed with the VPR are in fact remnants of *Phaeocystis* colonies.
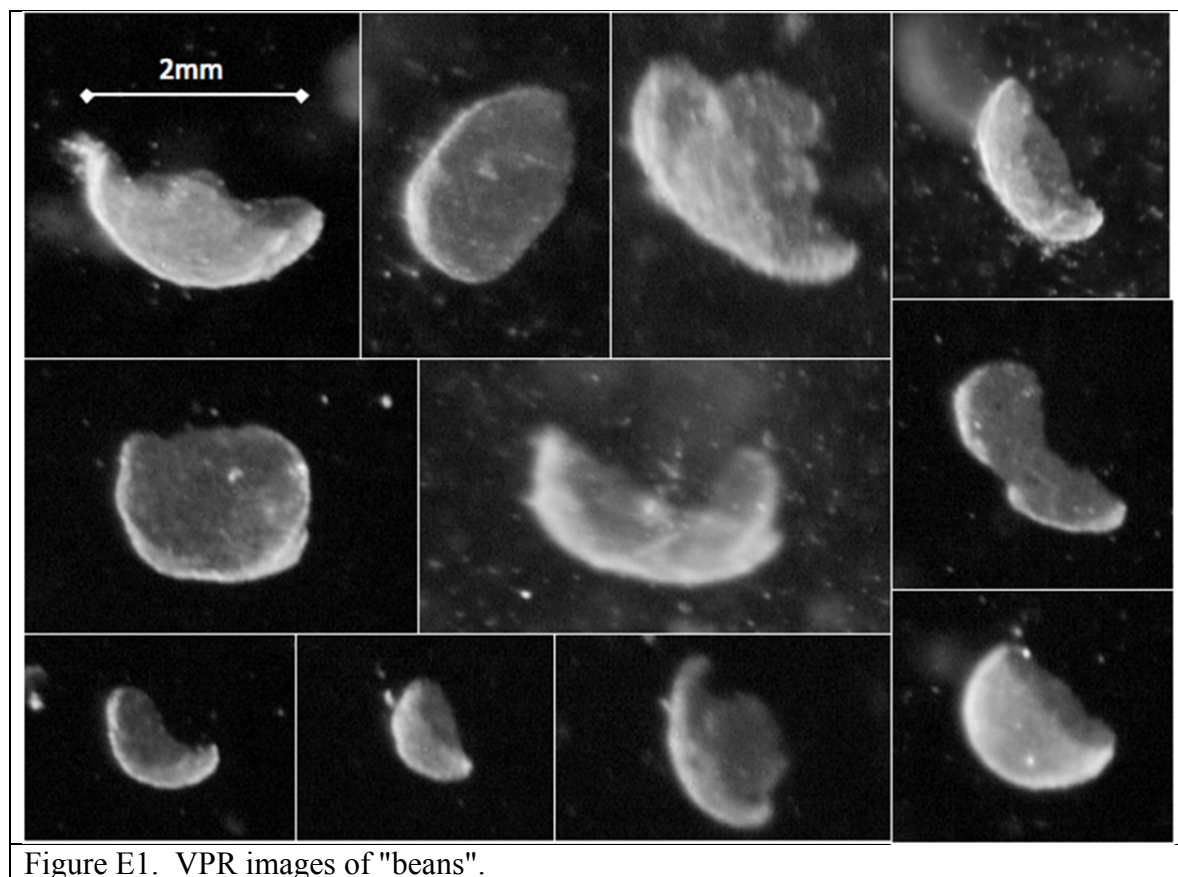
Figure E1. VPR images of "beans".
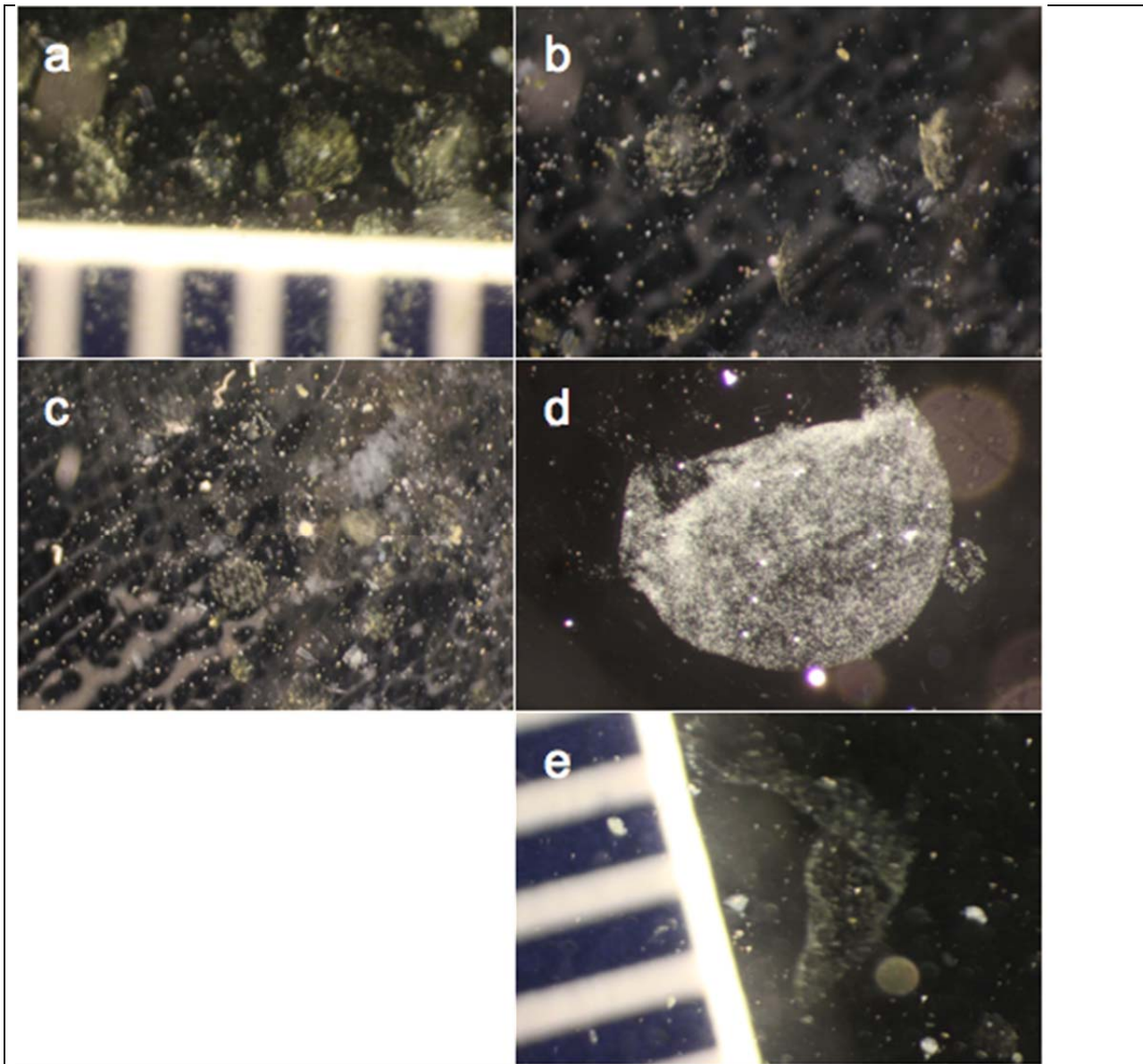
Figure E2. Images from Dissecting microscope. a-c) Station 96, 16x magnification 100 and 120m sample in petri dish. Ruler marks are at mm intervals. d) Station 96, 40x magnification, mounted on slide. e) Station 100, 16x magnification, 80m sample.
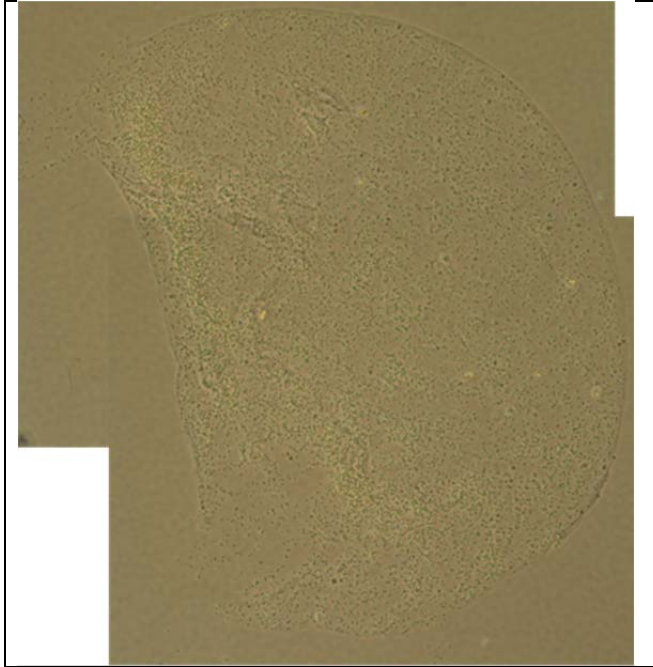
Figure E3. High magnification image of putative "bean" from Station 96 (Hai).

Appendix F. Oxygen titrations

Prepared by John Klinck and Marco Pedulli

Introduction

The CTD used on RVIB N.B. Palmer cruise NBP12-01 included two SBE 43 oxygen sensors. Water samples were taken from niskin bottles on the CTD rosette to verify the oxygen values through chemical titration.

Methods

Four oxygen samples were taken from about half of (54) CTD casts. Samples were chosen from niskin bottles at depths where oxygen concentrations spanned the range of observed values. In all cases , the oxygen samples were taken from the niskin bottles before any other samples were taken. The samples were fixed with 1 ml of NaOH/NaI and MgCl, in that order.

The pickled samples were then titrated with Na_2SO_4 using the onboard automated Ampirometric Oxygen Titrator (ref doc from Chris Langdon). A single set of three blank titrations was done at the beginning of the cruise. At least three standards were run before each set of titrations. The end points for each sample were entered into a spreadsheet . Oxygen concentrations were calculated using the formula provided in the Langdon manual. Values from primary and secondary oxygen sensors (SBE 43) from the CTD were automatically

Figure 1. Titrated values plotted against CTD sensors (red is primary, blue is secondary). The red and blue lines are the linear fit to each sensor. The black dashed line is the expected fit.

downloaded after each cast. Comparison between sensors and bottle titrations were carried out soon after. All units of oxygen concentration are reported here in ml/L.

111

Results

A total of 220 samples from 54 stations were sampled for oxygen calibration. On cast 51, the oxygen sensor from the VPR was exchanged for the primary CTD sensor as a test. These four values are removed from this analysis, as the VPR sensor proved to be unreliable. Comparison of the CTD oxygen concentration against the titrated oxygen concentration show considerable scatter (Fig. 1). A linear fit of the CTD oxygen to the titrated oxygen (for each sensor separately) yields a fit quite different from the unit slope, zero intercept line expected.

Figure 2. Comparison of primary and secondary observations for all bottles. The solid blue line is the linear fit between the two sensors. The black dashed line is the expected fit.

A direct comparison of the primary and secondary CTD sensors (Fig. 2) shows good consistency but the sensors do not exactly follow the one-slope, zero intercept line.

The mean differences between the primary sensor and titrated values (-0.34 ml/L) and between the secondary and titrated values (-0.26 ml/L) are about half of the standard deviations (0.66 and 0.62, respectively) indicating considerable scatter in these results.

Figure 3. The difference between the CTD and titrated oxygen for each sensor. The black line shows the mean difference and the blue lines are plus and minus one standard deviation.

This difference is evident in a plot of the difference between the sensor and titrated values plotted against the titrated oxygen (Fig. 3).

A number of the differences are larger than 2 ml/L indicating either a sampling or titrating error. Any point more than two standard deviations from the means is considered to be an outlier and is removed from further analysis. A total of 19 points was removed from the primary comparison and 15 from the secondary.
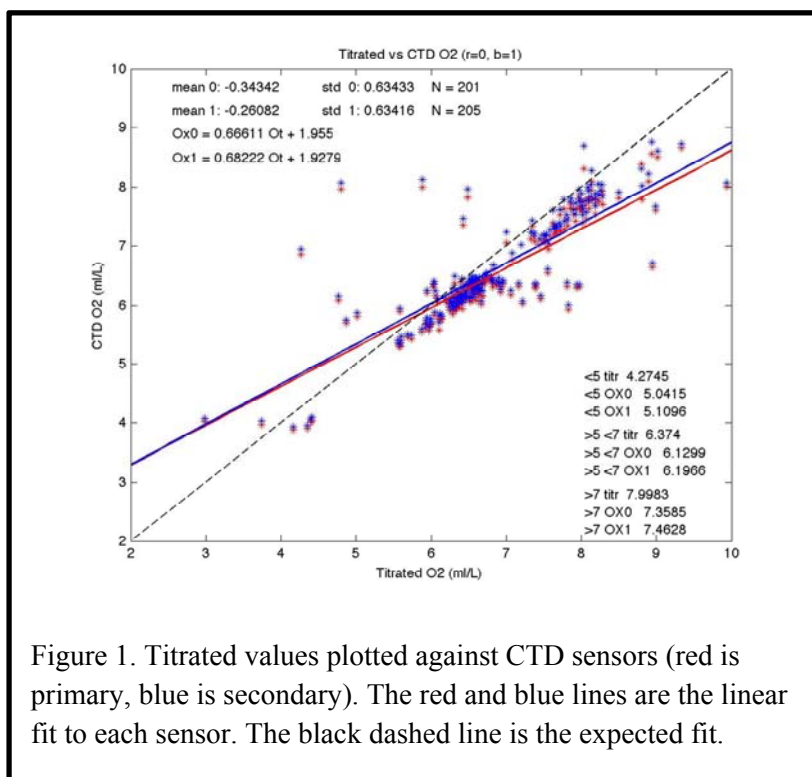

Figure 4. Titrated values plotted against CTD sensors (red is primary, blue is secondary). The red and blue lines are the linear fit to each sensor. The black dashed line is the expected fit. The outliers are removed from this analysis.

Analysis of the reduced data set results in a reduction of the standard deviation (Fig. 4). The mean offset between the titrated and CTD oxygen remains the same (-0.32 and -0.24, respectively).

Some of the differences between titrated and CTD oxygen values (Fig. 5) continue to be of order 1 ml/L, which indicates errors in sampling or titrating. So, a second data reduction is applied following the same procedure. Comparisons with

Figure 5. The difference between the CTD and titrated oxygen for each sensor. The black line shows the mean difference and the blue lines are plus and minus one standard deviation.

differences larger than 2 standard deviations (calculated from the reduced data) are again dropped from the analysis. A further 24 and 27 points, respectively are removed from the comparison.

Analysis of the reduced set of comparisons gives similar offsets between the two CTD sensors and the titrated oxygen values of -0.295 and -0.233 for the primary and secondary sensors, respectively (Fig. 6). The standard deviation of the differences is about half of the mean difference (0.165 and 0.168, respectively).

The linear regression line (Fig. 6) shows some increase in the difference between titrated and CTD values with increased oxygen concentration. However the regression lines for each sensor have similar offset and slope.

Figure 6. Titrated values plotted against CTD sensors (red is primary, blue is secondary). The red and blue lines are the linear fit to each sensor. The black dashed line is the expected fit. The outliers are removed from this analysis.

A comparison of the difference between the sensor and titrated values (Fig. 7) shows that there is scatter, and that most of the points with large differences have the sensor value about the same or higher than the titrated value.

Of particular concern for the oxygen sensors is whether the calibration changes over the time span of the cruise. A display of the difference against cast number (Fig. 8) is effectively a comparison
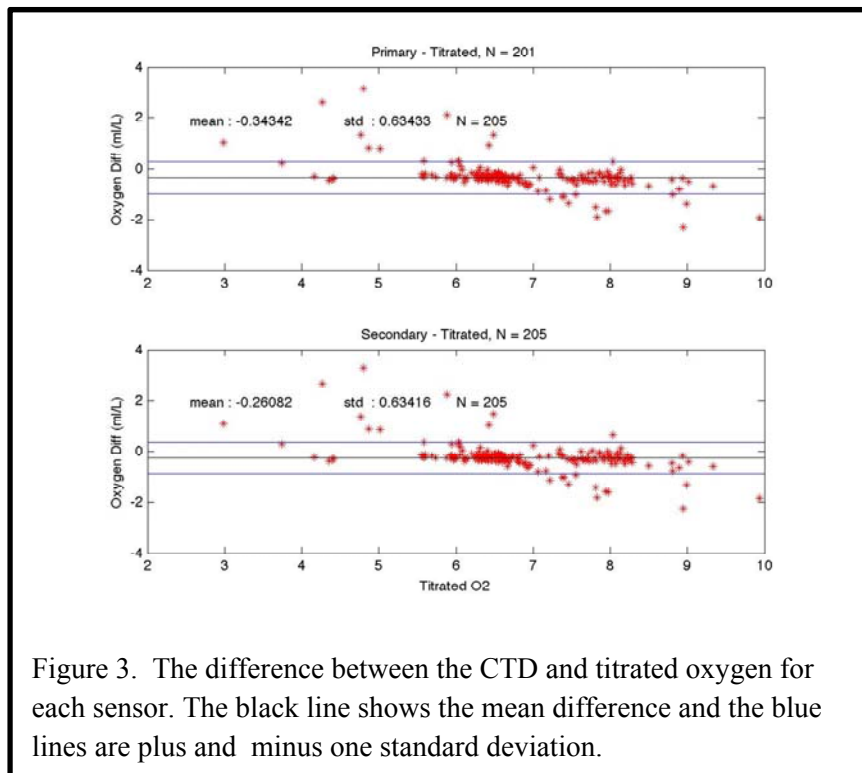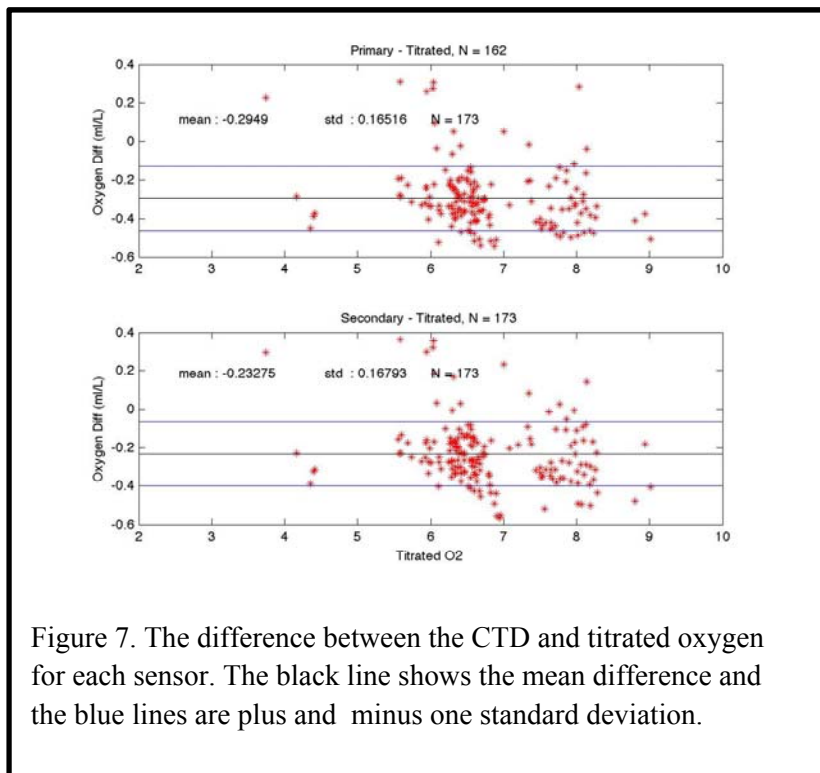

Figure 7. The difference between the CTD and titrated oxygen for each sensor. The black line shows the mean difference and the blue lines are plus and minus one standard deviation.

over time. A regression through the differences for each sensor has a slope of 0.00016 and 0.00005, respectively, which means that the average difference between titrated and CTD sensor values over 100 casts would change by 0.016 and 0.005 which should not affect the interpretation of these measurements. However, the scatter in these data do raise caution in making strong statements about the sensor drift.

Conclusions

Oxygen samples were taken from 54 CTD casts resulting in 220 oxygen samples. About 15 percent of these samples could not be used because of failed titration or unreasonably large differences with the CTD sensor.

After two removals of points that are more than two standard deviations from the mean, 162 and 173 points remain for analysis. These points reveal that both sensors are lower than the titrated value by 0.29 and 0.23 ml/L, respectively. An analysis over time indicates that there has been negligible drift of the calibration of these sensors over the time span of this cruise. Scatter in the titrated values raises caution in the interpretation of these results.
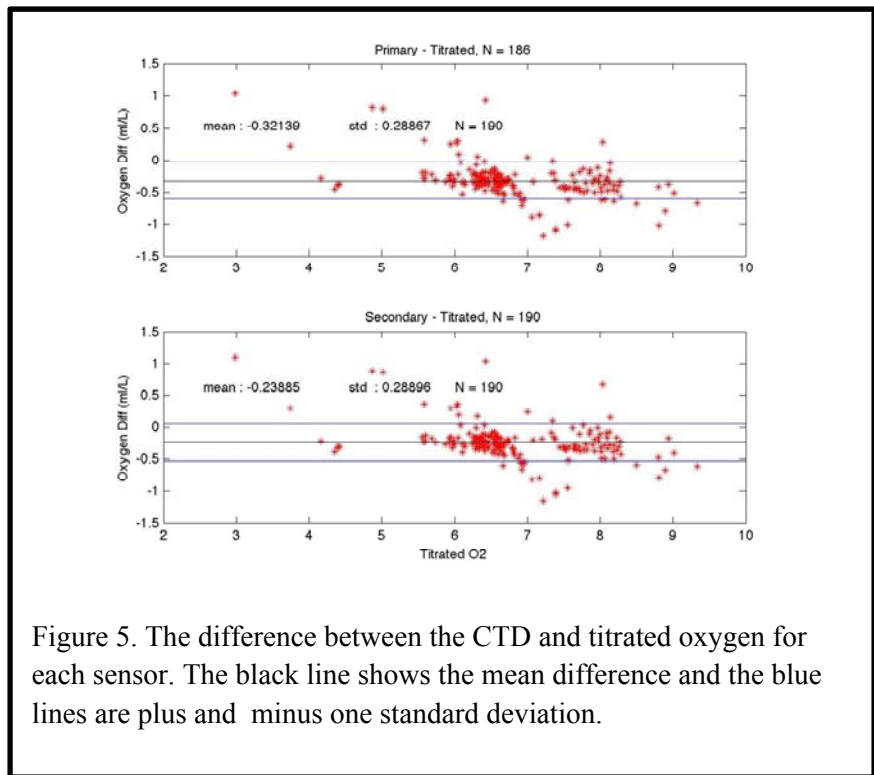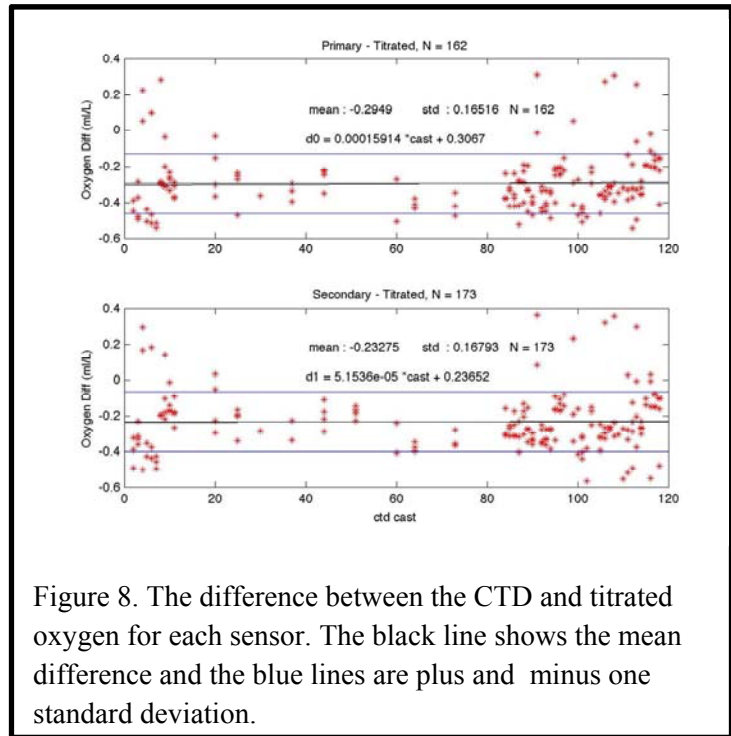

Figure 8. The difference between the CTD and titrated oxygen for each sensor. The black line shows the mean difference and the blue lines are plus and minus one standard deviation.

Appendix G. Salinity measurements - prepared by Suriyan Saramul and John Klinck

Introduction

The primary CTD on this cruise is a SeaBird SBE 9+ with two SBE4 salinity sensors. The CTD was housed in a 24 bottle rosette. Six salinity samples were taken from the deepest cast each day for calibration of the CTD salinity sensors. This report is an analysis of the bottle salinity and comparison to the CTD salinity values.

Methodology

The salinity samples were collect once a day whenever there were CTD casts; the six deepest Niskin bottles were sampled. There were 24 stations (in total) that have been sampled. The number and location of each station are shown in Fig. 1 and Table 1. After the water samples were drawn from the Niskin bottles, they were stored at room temperature (21°C) for at least 12 hours before analyzing.

The portable salinometer model 8410A was used to measure conductivity of the water sample. The conductivity of the water sample is automatically converted to the salinity by adjusting the ratio to the value from the IAPSO standard seawater. Standard seawater was run at the beginning of each sampling session. (Look at Salinometer Data Logger (SDL) Manual for more detail).

Figure 1: Sampling stations for bottle salinity.

Table 1: Salinity sampling stations. +ve/-ve are north/south and east/west for latitude and longitude, respectively

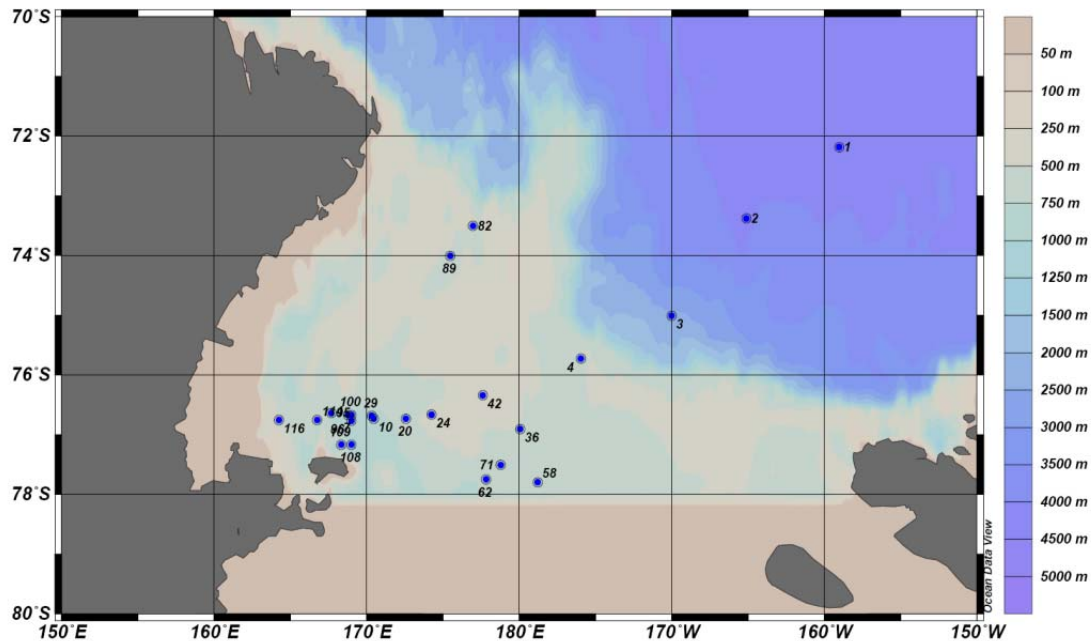| Stn.	Date Time	Latitude	Longitude	Stn.	Date Time	Latitude	Longitude
1	01/06/2012 22:32	-72.1819	-159.0165	58	01/24/2012 10:00	-77.7956	-178.7964
2	01/07/2012 19:01	-73.3786	-165.0936	62	01/24/2012 23:12	-77.7475	177.8147
3	01/08/2012 16:53	-75.0032	-170.0071	71	01/26/2012 01:12	-77.5065	178.7997
4	01/09/2012 13:21	-75.7261	-175.9472	82	01/28/2012 19:41	-73.5013	176.9778
7	01/13/2012 06:20	-76.6666	168.7751	89	01/29/2012 19:34	-74.0039	175.4882
9	01/14/2012 01:25	-76.6660	174.2459	95	01/31/2012 20:14	-76.6385	167.6861
10	01/15/2012 05:45	-76.7305	170.4751	96	02/01/2012 10:08	-76.7674	169.0093
20	01/16/2012 01:42	-76.7321	172.5715	100	02/01/2012 19:03	-76.6671	168.9967
24	01/17/2012 15:58	-76.6663	174.2502	108	02/02/2012 20:23	-77.1671	168.9988
29	01/18/2012 10:13	-76.6803	170.3326	109	02/03/2012 00:08	-77.1668	168.3330
36	01/19/2012 12:06	-76.9047	-179.9230	114	02/04/2012 14:21	-76.7534	166.7629
42	01/21/2012 07:30	-76.3391	177.6241	116	02/05/2012 00:22	-76.7498	164.2509

Results

There are in total 144 water samples (24 stations) collected from this cruise (NBP1201) for the salinity measurement. These samples were measured in eleven sample runs. The bottle salinity is plotted against CTD salinity (both primary (blue) and secondary (red) sensors; Fig. 2). The data points scatter along the one to one line (dark solid line). Most of the salinity values fall in the narrow range 34.4 to 34.7. One data point with lower salinity is from station 3 at 200 m depth. This water is quite fresh because this station was in the melting ice band from early in the cruise.
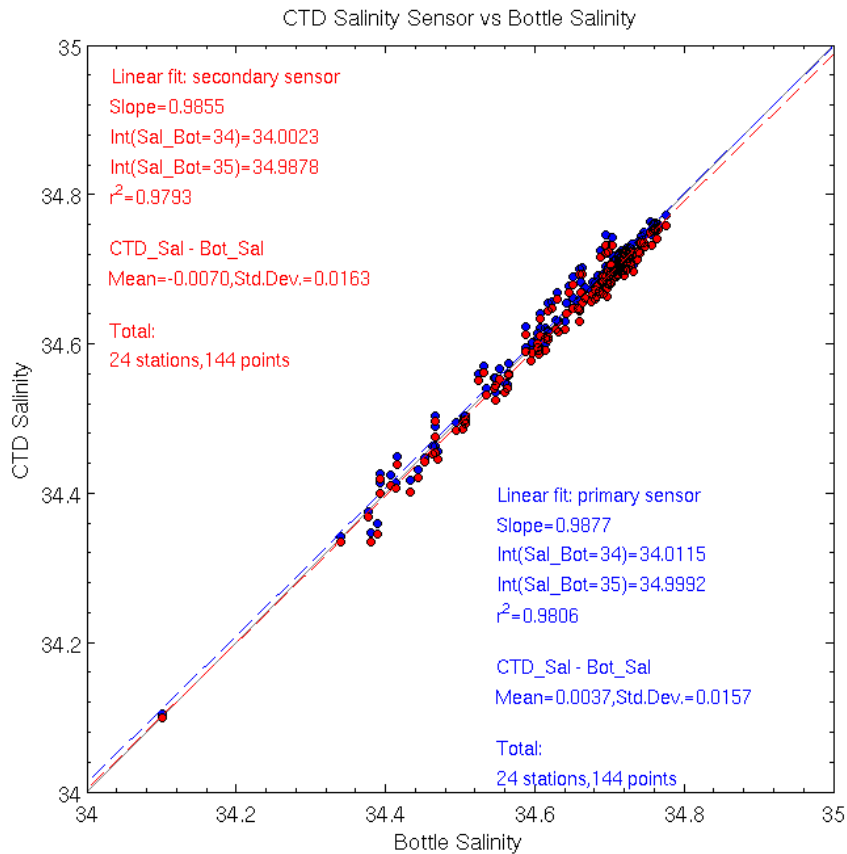
Figure 2: The plot of bottle salinity against primary CTD sensor (blue) and secondary CTD sensor (red). The slope, intercept, r^2, mean and standard deviation of error are also presented.

A linear fit for each CTD sensor checks the comparison between these two measurements. The slopes, intercepts, where bottle salinity equals 34 and 35, and r^2 are displayed for both primary sensor (blue) and secondary sensor (red). The r^2 (Fig. 2) shows reasonable correlation between bottle salinity and CTD salinity sensors with the value greater than 0.97. The error is the difference between CTD salinity and bottle salinity. The mean error and standard deviation of error are 0.0037 and 0.0157 for the primary salinity sensor and –0.0070 and 0.0163 for the secondary salinity sensor, respectively. These values represent only the average value, but do not show the variability among each data point or even sample run. Therefore, the differences are shown in Fig. 3.

A clear feature of this analysis (Fig. 3) is that each sample run has a consistent and small scatter but each group has a rather large offset relative to the other groups (after run 3). In run 6, there appears to be a trend, but during this run of 18 samples (3 stations), a standard was run before each set of samples. Careful inspection shows that each group is offset from the others after the standard. Each sample run is analyzed and the results are shown in Table 2. The number in the parenthesis represents the secondary salinity results.
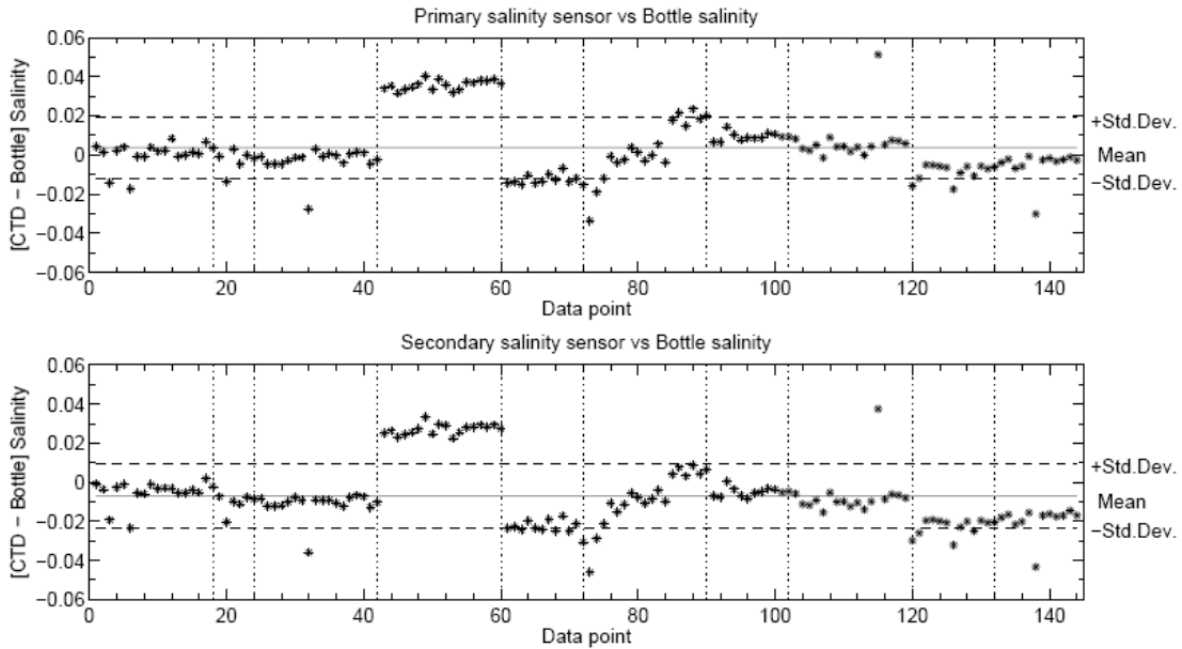
Figure 3: The difference between primary salinity and bottle salinity (top panel) and between secondary salinity and bottle salinity (bottom panel). Dash lines represent ±1 standard deviation of the difference and vertical dot lines separate the sample runs.

Table 2 clearly shows a good correlation between CTD salinity and bottle salinity for the 4th run, but with a different mean from the other runs.

The removal of data points that fall outside one standard deviation from the mean might help to improve the correlation between the CTD salinity and bottle salinity (see Fig. 4). A total of 39 and 35 data points are removed from the primary and secondary salinity sensors, respectively. This reduced data set (Fig. 4) improves the correlation between CTD salinity and bottle salinity, except for the mean error of secondary salinity sensor (~ -0.0097).

Given the difficulty with the salinometer samples, the two salinity sensors on the CTD were compared (Fig. 5) over all bottle samples (1963 values, not just those for which salinity samples were drawn). This analysis indicates that there is a mean difference of 0.012173 between the two sensors with the secondary sensor having lower salinity than the primary.

Table 2: The slope and intercept of the linear fit between bottle salinity and CTD salinity for both primary and secondary (secondary is in the parenthesis). Mean of error (CTD − bottle) and standard deviation of error are shown in the last two columns. Note: the intercepts are shown for bottle salinity = 0.

Run#	#of Stn(pts)	Slope	Intercept	r^2	Mean Err.	Std.Dev.Err.
1	3(18)	0.9960	0.1382	0.9985	0.0004	0.0064
		(0.9984)	(0.0492)	(0.9986)	(-0.0052)	(0.0062)
2	1(6)	0.9883	0.4008	0.9986	-0.0034	0.0058
		(0.9843)	(0.5299)	(0.9991)	(-0.0108)	(0.0049)
3	3(18)	0.9839	0.5553	0.9955	-0.0030	0.0066
		(0.9918)	(0.2740)	(0.9956)	(-0.0113)	(0.0064)
4	3(18)	1.0091	-0.2784	0.9994	0.0358	0.0025
		(1.0067)	(-0.2052)	(0.9993)	(0.0271)	(0.0027)
5	2(12)	0.9952	0.1520	0.9994	-0.0127	0.0026
		(1.0064)	(-0.2454)	(0.9990)	(-0.0230)	(0.0035)
6&7	3(18)	0.9948	0.1810	0.9833	0.0026	0.0151
		(1.0019)	(-0.0753)	(0.9859)	(-0.0081)	(0.0140)
8	2(12)	0.9826	0.6119	0.9993	0.0093	0.0022
		(0.9886)	(0.3893)	(0.9989)	(-0.0050)	(0.0024)
9	3(18)	1.0426	-1.4703	0.9005	0.0059	0.0126
		(1.0424)	(-1.4807)	(0.8995)	(-0.0082)	(0.0126)
10	2(12)	0.9909	0.3085	0.9773	-0.0081	0.0037
		(0.9927)	(0.2321)	(0.9759)	(-0.0222)	(0.0038)
11	2(12)	1.0615	-2.1357	0.9980	-0.0053	0.0080
		(1.0584)	(-2.0445)	(0.9980)	(-0.0195)	(0.0077)

Conclusions

The water samples from 24 stations with 6 samples each have been analyzed with the portable salinometer model 8410A. Before running each set of samples the IAPSO standard seawater had been sampled to set the standard ratio. Therefore the calculated salinity (bottle salinity) of the samples is dependent on the standard ratio for each run. The comparison between the bottle salinity and CTD salinity both primary and secondary sensors show good correlation with r^2 in the order of 0.98, but the mean difference between bottle salinity and CTD salinity is still large. The error of each sample (Fig. 3) tends to deviate from mean error for each group of samples.

The salinometer was re-zeroed after the third set of measurements because the measurements showed considerable variability. At that time, some of the tubing was also replaced. It is clear from Fig. 3 that each run has an offset from the other runs. This offset occurs after the standard is run. During run 6, a standard was run three times, before each group of six bottles. Within this single session, there is a clear offset among the clusters of samples.

The cause of these offsets has not been determined. This information has been relayed to the MST on board for further analysis. Because of these offsets, these data can not be used to calibrate the conductivity sensors. Analysis of pre- and post-cruise calibration on these sensors will determine their quality.
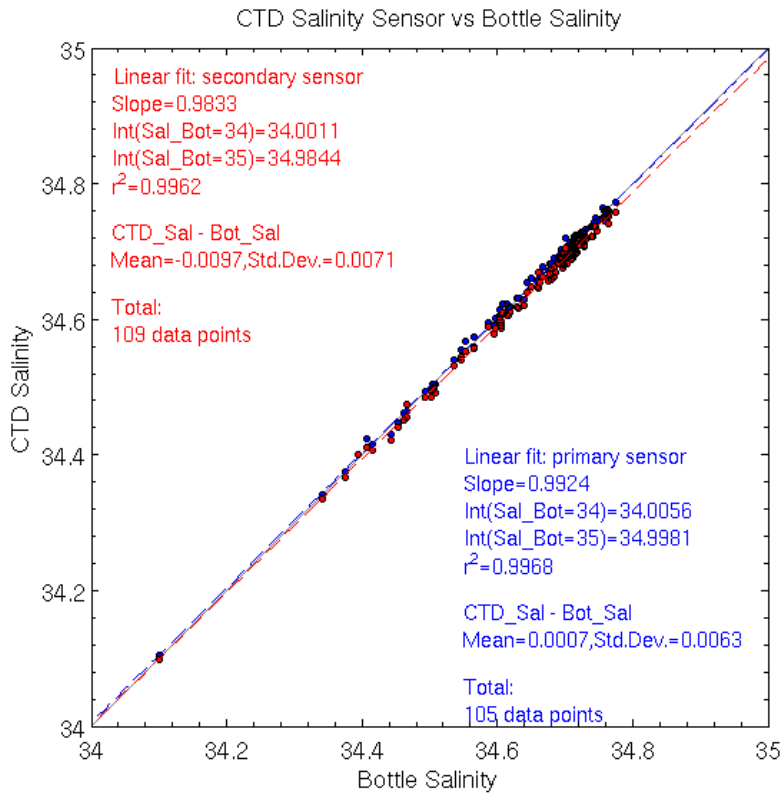
Figure 4: The plot of primary (blue) and secondary (red) salinity against bottle salinity after the outliers have been removed. The one to one plot is a dark solid line.
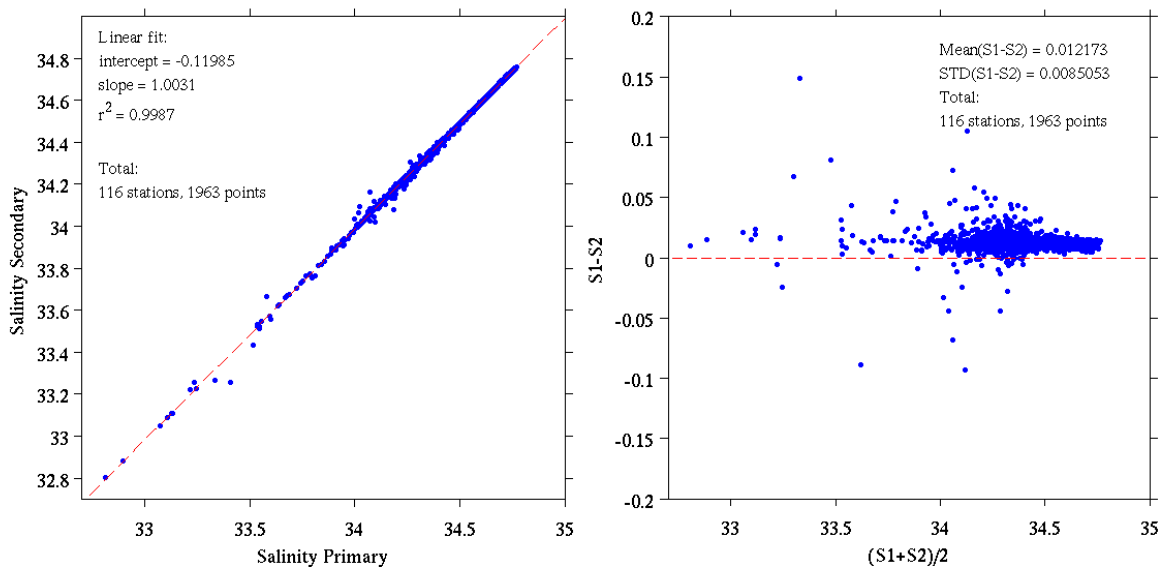

Figure 5. Comparison of the primary (S1) and secondary (S2) salinity sensors for all bottle samples for the cruise. The right panel shows the primary to secondary difference plotted